WCAP-16045-NP
Revision 0

March, 2003

Qualification of the Two-Dimensional Transport Code PARAGON

Qualification of the Two-Dimensional Transport Code PARAGON

Prepared by:
M. Ouisloumen
H. Huria
L. T. Mayhue
R. M. Smith
S. W. Park
M. J. Kichty

Approved: Y. A. Chao, March 6, 2003
Y. A. Chao, Acting Manager
Advanced Software Development

Approved: Richard A. Lorety 3/4/2003
R. A. Loretz, Manager
U.S. Fuel and Fuel Components

Page Left Intentionally Blank

Acknowledgement

The authors wish to acknowledge the contributions made by J. D. St. John, A. N. Piplica, R. D. Erwin, R. T. Smith, J. A Barsic, T. A. Downs, and T. J. Congedo. The authors also want to acknowledge the reviews of this document by R. A. Loretz, Waldemar Lipiec, Y. A. Chao, R. B. Sisk, and W. H. Slagle. The authors also wish to thank C. Bolton and J. Pavlecic for help in preparation of this document.

Page Left Intentionally Blank

Table of Contents

List of Tables

Page Left Intentionally Blank

List of Figures

Section 1.0: Introduction

The purpose of this report is to provide documentation of the qualification of PARAGON, a new Westinghouse neutron transport code. It is also requested that the NRC provide generic approval of PARAGON for use with Westinghouse's nuclear design code system or as a standalone code. The code will be used primarily to calculate nuclear input data for three-dimensional core simulators. Based on the qualification of PARAGON as documented herein, PARAGON can be used as a standalone or as a direct replacement for all the previously licensed Westinghouse Pressurized Water Reactor ("PWR") lattice codes, such as PHOENIX-P. Thus, other topicals that reference the Westinghouse nuclear design code system will remain applicable with PARAGON.

A major nuclear design code system in use at Westinghouse since 1988 consists of two primary codes, PHOENIX-P and ANC. PHOENIX-P is the neutron transport code currently used to provide nuclear input data for ANC. The qualification and license approval of the use of PHOENIX-P for PWR core design calculations is provided in Reference 1-2.

PARAGON is a new code written entirely in FORTRAN 90/95. PARAGON is a replacement for PHOENIX-P and its primary use will be to provide the same types of input data that PHOENIX-P generates for use in three dimensional core simulator codes. This includes macroscopic cross sections, microscopic cross sections for feedback adjustments to the macroscopic cross sections, pin factors for pin power reconstruction calculations, and discontinuity factors for a nodal method solution.

PARAGON is based on collision probability – interface current cell coupling methods. PARAGON provides flexibility in modeling that was not available in PHOENIX-P including exact cell geometry representation instead of cylinderization, multiple rings and regions within the fuel pin and the moderator cell geometry, and variable cell pitch. The solution method permits flexibility in choosing the quality of the calculation through both increasing the number of regions modeled within the cell and the number of angular current directions tracked at the cell interfaces. Section 2 will provide further details on PARAGON theory and features.

The qualification of a nuclear design code is a large undertaking since it must address the qualification of the methodology used in the code, the implementation of that methodology, and its application within a nuclear design system. For this reason, Westinghouse has historically used a systematic qualification process, which starts with the qualification of the basic methodology used in the code and proceeds through logical steps to the qualification of the code as used with the entire system. This process was used when qualifying PHOENIX-P/ANC system in Reference 1-2. This same process is followed for the qualification of PARAGON in this report.

Consistent with the qualification process described above, the qualification of PARAGON will consist of three parts: 1) comparisons to critical experiments and isotopic measurements, 2) comparisons of assembly calculations with Monte Carlo method calculations (MCNP), and 3) comparisons against measured plant data. The first two parts will qualify the methodology used in PARAGON and its implementation. The third part will qualify the use of PARAGON data for core design applications. Where appropriate, comparisons will also be made to PHOENIX-P results.

The current PARAGON cross section library is a 70-group library with the same group structure as the library currently used with PHOENIX-P. The PARAGON qualification library has been improved [ ]^{a,c}

This report is organized in the Sections as described below.

Section 2 presents an overview of the PARAGON theory and its implementation. The nuclear data library used for this qualification is also described in this section.

Section 3 presents the results of PARAGON calculations for many standard critical experiments. These include the Strawbridge-Barry 101 criticals, the Kritz high temperature experiments, and the Babcock and Wilcox critical experiments with Urania-Gadolinia fuel. Section 3 also presents reactivity and power distribution comparisons between PARAGON and Monte Carlo (MCNP) calculations for single assembly problems. Various assembly designs similar to those currently in use in PWR cores are included in these MCNP/PARAGON comparisons. Finally, isotopic comparisons are made between PARAGON and the Yankee and Saxton isotopic measurements.

Section 4 presents the results of using PARAGON input data with a three-dimensional core simulator model (in this case ANC) and compares the calculations to actual plant measurements. The parameters compared are boron letdown curves, beginning of cycle (BOC) HZP critical boron, BOC isothermal temperature coefficients (ITC), and BOC rodworths. Comparisons of the results of using PARAGON input data with a three-dimensional core simulator model (ANC) against measured core power distributions are also shown for several cycles. Section 4 also presents comparisons of PARAGON/ANC model results against those of PHOENIX-P/ANC for core calculations for which there are no plant measurements (e.g. shutdown margin, ejected rod, etc).

Section 2.0: PARAGON Methodology

2.1 Introduction

PARAGON is a two-dimensional multi-group neutron (and gamma) transport code. It is an improvement over the Westinghouse licensed code PHOENIX-P (Reference 2-1). The main difference between PARAGON (Reference 2-2) and PHOENIX-P resides in the flux solution calculation. PHOENIX-P uses a nodal cell solution coupled to an S4 transport solution as described in Reference 2-1. PARAGON uses the Collision Probability theory within the interface current method to solve the integral transport equation. Throughout the whole calculation, PARAGON uses the exact heterogeneous geometry of the assembly and the same energy groups as in the cross-section library to compute the multi-group fluxes for each micro-region location of the assembly.

In order to generate the multi-group data that will be used by a core simulator code PARAGON goes through four steps of calculations: resonance self-shielding, flux solution, homogenization and burnup calculation. This section will describe the theoretical models that each of the PARAGON components is using.

2.2 PARAGON Cross-sections Library

The current PARAGON cross section library uses ENDF/B VI as the basic evaluated nuclear data files. Currently the library has 70 neutron energy groups [ ]^{a,c}. But PARAGON is designed to work with any number of energy groups that is specified in the library, and Westinghouse intends to continuously improve the library as better data become available and recommended by the data evaluation community. This library has been generated using the NJOY processing code (Reference 2-3). To account for the resonance self-shielding effect, the group cross-sections are tabulated as a function of both temperature and background scattering cross-section (dilution). The resonance self-shielding module of the code uses these resonance self-shielding tables to compute the isotopic self-shielded cross-section in the real heterogeneous situation. The library contains energy group cross-sections and transport-corrected P0 scattering matrices as a function of temperature. The P0 scattering matrices contain diagonal corrections for anisotopic scattering. [ ]^{a,c}

2.3 Theory of PARAGON modules

This section will describe in detail the physics models and different mathematical approximations that each of the PARAGON components is using.

2.3.1 Cross-section resonance self-shielding module

PARAGON uses the same resonance self-shielding theory as in PHOENIX-P (Reference 2-1) but generalized to handle the multi-regions in cells which is needed mainly to support the fuel rod design codes. PHOENIX-P method is based on an average-rod resonance self-shielding algorithm (Reference 2-4). The non-regularity of the lattice is taken into account using space dependent Dancoff factor corrections. In the resonance energy range, the neutron slowing-down is the most dominant process. This remark supports the assumption of the factorization of the flux into a product of a macroscopic term ψ varying slowly with the lethargy and a term φ describing the local variations due to the resonances of the isotopes:

$$\phi = \psi\varphi \tag{2-1}$$

As in the PHOENIX-P code, PARAGON uses the collision probabilities to solve the slowing-down equation in pin cells with the real heterogeneous geometry. The rational approximation is used to evaluate the fuel to fuel collision probabilities and the flux φ is approximated using the intermediate resonance approximation (Reference 2-4)

2.3.2 *Flux calculation module*

The neutron (or gamma) flux, obtained from the solution of the transport equation, is a function of three variables: energy, space and angle. For the energy variable, PARAGON (Reference 2-2) uses the multi-group method where the flux is integrated over the energy groups. For the spatial variable, the assembly is subdivided into a number of sub-domains or cells and the integral transport equation is solved in the cells using the collision probability method. The cells of the assembly are then coupled together using the interface current technique (Reference 2-2). At the interface, the solid angle is discretized into a set of cones (Reference 2-2, 2-5) where the surface fluxes are assumed to be constant over each angular cone. PARAGON has been written in a general way so that the cell coupling order is limited only by the computer memory. The collision probability method is based on the flat-flux assumption, which will require subdividing the cells into smaller zones. Thus, for each cell in the assembly, the system of equations to be solved is given by the discretized one energy group transport equation:

$$\begin{aligned}
\phi_i &= \sum_{\alpha,\rho\nu} P_{is_\alpha}^{\rho\nu} J_{-,\alpha}^{\rho\nu} + \sum_j V_j P_{ij} F_j, \\
J_{+,\alpha}^{\rho\nu} &= \sum_{\beta,\eta\mu} P_{s_\alpha s_\beta}^{\rho\nu\,\eta\mu} J_{-,\beta}^{\eta\mu} + \sum_i P_{s_\alpha i}^{\rho} F_i, \\
J_{-,\alpha}^{\rho\nu} &= \sum_{\beta,\eta\mu} B_{\alpha\beta}^{\rho\nu\,\eta\mu} J_{+,\beta}^{\eta\mu}
\end{aligned} \tag{2-2}$$

The following notations are used: ϕ_i for the average flux in zone i (flat-flux assumption), $J_{\pm,\alpha}^{\rho\nu}$ for the current entering $(-)$ or leaving $(+)$ the cell through the surface oriented by the exterior or interior normal $\vec{n}_{\pm\alpha}$, $B_{\alpha\beta}^{\rho\nu\eta\mu}$ for the albedo coefficients and F_j for the neutron (fission and scattering) emission density or gamma production density (prompt fission, neutron capture, scattering, decay of fission products, etc). In those equations, the set of cones are indicated by (ρ,ν) and (η,μ) defining the azimuthal φ (not to be confused with the flux φ in the previous section) and polar ϑ coupling orders:

$$[\varphi,\vartheta] \in [0,2\pi]\times[0,\pi] = \bigcup_\rho [\varphi_\rho,\varphi_{\rho+1}] \times \bigcup_\nu [\vartheta_\nu,\vartheta_{\nu+1}] \tag{2-3}$$

The first flight collision probabilities (P_{ij}), transmission probabilities (P_{ss}) and leakage (P_{si}) (or surface to volume (P_{is})) collision probabilities are given by:

$$\begin{aligned}
P_{ij} &= \frac{1}{V_j}\int_{D_i} d\vec{r} \int_{D_j} d\vec{r}' \frac{e^{-\tau(u)}}{4\pi u^2}, \\
P_{is_\alpha}^{\rho\nu} &= \frac{1}{\pi S_\alpha \sqrt{A_\alpha^{\rho\nu}}} \int_{D_i} d\vec{r} \int_{\partial D_\alpha} d^2 r_s \psi_{-,\alpha}^{\rho\nu}(\vec{\Omega})(\vec{\Omega}\cdot\vec{n}_{-,\alpha}) \frac{e^{-\tau(t)}}{t^2}, \\
P_{s_\alpha s_\beta}^{\rho\nu\,\eta\mu} &= \frac{\sqrt{A_\alpha^{\rho\nu}}}{\pi S_\beta \sqrt{A_\beta^{\eta\mu}}} \int_{\partial D_\alpha} d^2 r_s' \int_{\partial D_\beta} d^2 r_s \psi_{+,\alpha}^{\rho\nu}(\vec{\Omega}) \psi_{-\beta}^{\eta\mu}(\vec{\Omega})(\vec{\Omega}\cdot\vec{n}_{+\alpha})(\vec{\Omega}\cdot\vec{n}_{-,\beta}) \frac{e^{-\tau(t')}}{t'^2}
\end{aligned} \tag{2-4}$$

where the following definitions are used:

- $t' = \left\| \vec{r}_s - \vec{r}_s' \right\|$, $t = \left\| \vec{r}_s - \vec{r} \right\|$ and $u = \left\| \vec{r} - \vec{r}' \right\|$ are the path of neutrons from surface to surface, volume to surface and volume to volume respectively, and $\tau(x)$ is the optical path.
- S_α is the surface area of the cell's surface element α and V_i is the volume of zone i.
- The domains of integration cover the zone's volume D_i and the cell's surface element ∂D_α

The transmission (P_{ss}) and leakage (P_{sl}) collision probabilities in the equations above have been derived by expanding the angular fluxes, at cell surfaces ∂D_α, in a finite set of discrete angular fluxes with the representative functions $\psi_{\pm,\alpha}^{\rho v}(\bar{\Omega})$. Two distinct components are used for entering and outgoing fluxes:

$$\psi_{\pm,\alpha}^{\rho v}(\bar{\Omega}) = \frac{1}{\sqrt{A_\alpha^{\rho v}}} H(\bar{\Omega} \in \Omega_{\rho v}), \tag{2-5}$$

where

$$A_\alpha^{\rho v} = \frac{1}{\pi} \int_{(4\pi)} (\bar{\Omega} \cdot \bar{n}_{\pm,\alpha}) H(\bar{\Omega} \in \Omega_{\rho v}) d\bar{\Omega}, \tag{2-6}$$

and $H(\bar{\Omega} \in \Omega_{\rho v})$ is the Heaviside distribution defined by:

$$H(\bar{\Omega} \in \Omega_{\rho v}) = \begin{cases} 1 \Rightarrow \bar{\Omega} \in \Omega_{\rho v} \Leftrightarrow [\varphi, \vartheta] \in [\varphi_\rho, \varphi_{\rho+1}] \times [\vartheta_v, \vartheta_{v+1}] \\ 0 \Rightarrow \bar{\Omega} \notin \Omega_{\rho v} \end{cases} \tag{2-7}$$

The solution of the above algebraic system of equation (2-2) over the entire assembly is obtained by the response heterogeneous matrix method, which uses current-flux iterations (Reference 2-2, 2-6). The flux solver module has been extensively tested and proved to perform very accurately (Reference 2-2,2-7,2-8).

2.3.3 *Homogenization module*

The next step in PARAGON calculation after the flux solution is the leakage correction. The purpose of this module is to compute the multi-group diffusion coefficients and the multi-group critical flux (spectrum) for the entire homogenized assembly (or parts of the assembly, like baffle/reflector regions). This is usually achieved by solving the fundamental mode of the transport equation (Reference 2-4). The flux solution to the transport equation is assumed to be separable in a space part and an energy and angle part: $\phi(\vec{r}, E, \bar{\Omega}) = \varphi(\vec{r})\psi(E, \bar{\Omega})$. This assumption leads to the following B_1 system of equations (flux-current) to be solved (Reference 2-4):

$$\begin{aligned} \Sigma_g \psi_g \pm iBJ_g &= \sum_{g'} \Sigma_{0,g' \to g} \psi_{g'} + \chi_g, \\ \pm iB\psi_g + 3\alpha_g \Sigma_g J_g &= 3 \sum_{g'} \Sigma_{1,g' \to g} J_{g'} \end{aligned} \tag{2-8}$$

where: (ψ_g, J_g) are the fundamental mode flux and current for group g, Σ_g is the homogenized total cross-section, $\Sigma_{0,g'\to g}$ and $\Sigma_{1,g'\to g}$ are the isotropic and the anisotropic scattering matrices, χ_g is the fission spectrum (normalized to one), $i^2 = -1$, B^2 is the fundamental material buckling and

$$\alpha_g = \begin{cases} \frac{1}{3}x^2\left(\frac{\arctan(x)}{x-\arctan(x)}\right) & \text{if } x^2 = (\frac{B}{\Sigma_g})^2 > 0 \\ \frac{1}{3}x^2\left(\frac{\ln(\frac{1+x}{1-x})}{\ln(\frac{1+x}{1-x})-2x}\right) & \text{if } x^2 = -(\frac{B}{\Sigma_g})^2 > 0 \end{cases} \qquad (2\text{-}9)$$

Note that the above equations are usually solved for the critical material bucking B^2 which makes the neutron multiplication factor equal to one.

For each energy group, the micro-region fluxes are corrected by the ratio of the fundamental mode fluxes and the assembly averaged fluxes to get the final micro-region critical fluxes. Another model (Reference 2-9) to compute the critical flux has been implemented in PARAGON. In this model, the neutron source has been modified by adding an artificial absorption cross-section $D_g B^2$ in each micro-region of the assembly. In this case, the diffusion coefficients are first computed by using the previous model. In case of fuel assemblies, the two models are comparable. The second model is mainly used in the case of critical experiments for which a measured buckling is usually available.

2.3.4 Depletion module

The assembly composition changes following neutron irradiation are obtained by calculating the isotopic depletion and buildup in the heterogeneous geometry, using an effective one-group collapsed flux and cross-sections. The differential equations solved by PARAGON depletion module are given by:

$$\frac{d}{dt}N_i(t) = \sum_j \gamma_{j\to i}\sigma_{f,j}\phi(t)N_j(t) - N_i(t)\left[\sigma_{a,i}\phi(t) + \lambda_i\right] + N_j(t)\lambda_j + N_k(t)\sigma_{ki}\phi(t) \qquad (2\text{-}10)$$

Where:

- N_i is the concentration (number density) for the isotope i
- $\gamma_{j\to i}$ is the yield of isotope i per fission of isotope j
- $\sigma_{f,j}$ is the energy-integrated microscopic fission cross-section of isotope j
- $\sigma_{a,i}$ is the energy-integrated microscopic absorption cross-section of isotope i
- λ_i is the decay constant of isotope i
- λ_j is the decay constant of the parent isotope j
- σ_{ki} is the energy-integrated microscopic capture cross-section of isotope k leading to the formation of isotope i
- $\phi(t)$ is the energy-integrated flux for the zone where the isotope is present.

PARAGON uses the predictor-corrector technique to better account for the flux level variation (Reference 2-4). The module is, however general enough to the extent that any new chain can be added easily with very minor changes in the code.

The code detects automatically the regions to be depleted, but the user has the option to hold any region in the assembly as non-depletable. For the boron depletion, the user has a choice of depleting it according to a letdown curve that is provided through the input or exponentially (i.e depletion chain). Note that gamma heating is taken into account in the evaluation of the flux level during the burnup depletion.

2.4 Other Modeling Capabilities

This section will describe the other capabilities implemented in PARAGON such as the fuel temperatures, branch calculations etc.

2.4.1 Temperature Model

Through the input, PARAGON is provided with [ ]^{a,c} temperature tables [function of

]^{a,c}

PARAGON has a module that interpolates in these tables to compute the temperatures for each isotope present in the model before calling the self-shielding module for cross-sections calculations.

2.4.2 Doppler Branch Calculation

A Doppler branch calculation capability is built into PARAGON. This capability permits fuel temperature variations to be modeled while keeping all other parameters constant. Results of these calculations are used to generate changes in [ ]^{a,c} which are passed to the core models to capture Doppler effects. [ ]^{a,c}

2.4.3 Thermal Expansion

A model to expand the radii of the cylindrical region has been implemented in PARAGON. [ ]^{a,c}

The code uses this capability mainly in the case of the Doppler branch calculation. It also has a flag to turn it on in any calculation step.

2.4.4 Interface Module

PARAGON has the flexibility of printing many types of micro and macro physics parameters. Hence the user can request to edit the fluxes, partial currents, surface fluxes, different reaction rates, isotopic distribution etc. The editing could be done for micro-regions, or as an average over

a cell or as an average over a group of cells, and for any number of energy groups (i.e. the code can collapse to any number of groups for editing).

PARAGON uses files to store the data needed for core calculations. Those files are processed by other codes used for core modeling and analysis.

2.4.5 Reflector Modeling

PARAGON generates the reflector constants [

]^{a,c}

Section 3.0: Critical Experiments and Isotopics

The primary use of PARAGON will be to generate nuclear data for three dimensional core simulator models. Thus, the best qualification of PARAGON is through comparison of core simulator plant models developed using PARAGON-calculated nuclear input data against measured plant data These comparisons will be made in section 4 of this report.

As described in Section 1.0, Westinghouse has historically used a systematic qualification process which starts with the qualification of the basic methodology used in the code and proceeds through logical steps to the qualification of the code as used with a complete nuclear code system (Reference 3-1). Following this process for the PARAGON code, PARAGON has been used in stand-alone mode to model standard critical experiments. The results of these calculations are presented in this section. In addition, comparisons of the results of PARAGON single assembly calculations with the same assembly run in the Monte Carlo code MCNP (Reference 3-12) are shown for both reactivity and power distribution. The MCNP calculations used a continuous energy ENDF/B-VI based library.

At the end of this section, a comparison of PARAGON calculated isotopics against those measured at Saxton and Yankee is presented

3.1 Critical Experiments

PARAGON results from modeling the following experiments are provided in this section: 1) the Strawbridge–Barry 101 Criticals (Section 3.1.1), 2) the KRITZ high-temperature criticals (Section 3.1.2), and 3) the Babcock & Wilcox Spatial Criticals (Section 3.1.3).

3.1.1 Strawbridge-Barry 101 Criticals

The Strawbridge and Barry criticals contains 101 uniform, light water lattices. These criticals contain 40 uranium oxide and 61 uranium metal cold clean experiments (Reference 3-2). These critical experiments have historically been included in Westinghouse code qualifications since they cover a wide range of lattice parameters and therefore provide a severe test for the lattice code to predict reactivities accurately over a broad range of conditions.

Since the Strawbridge-Barry criticals are uniform lattices for which experimental bucklings have been reported, these criticals have been treated as single pin cells in PARAGON. The range of lattice parameters covered by these criticals are:

Enrichment (a/o U^{235}) :	1.04 to 4.069
Boron concentration (ppm):	0 to 3392
Water to uranium ratio·	1.0 to 11.96
Pellet diameter (cm):	0.44 to 2.35
Lattice pitch (cm):	0.95 to 4.95
Clad material:	none, aluminum, stainless steel
Lattice type:	square, hexagonal
Fuel density (g/cm^3):	7.5 to 18.9

Since the current version of PARAGON does not model hexagonal fuel, the hexagonal pin cells were replaced by equivalent square pin cells which preserve moderator area.

A summary of the results is shown in Table 3-1. This table shows reactivity predictions for various groupings of the criticals. Of particular interest is the result for all UO_2 experiments. The mean K_{eff} for these forty experiments is [ ]^{a,c} with a standard deviation of [ ]^{a,c} The mean K_{eff} for all experiments was [ ]^{a,c} with a standard deviation of [ ]^{a,c} Figures 3-1 through 3-5 show the PARAGON results as a function of water to uranium ratio, enrichment, pellet diameter,

experimental buckling, and soluble boron concentration (seven criticals had soluble boron). The results in these figures show excellent performance for PARAGON over the entire range of each parameter with no significant bias or trends for any lattice parameter.

3.1.2 KRITZ High-Temperature Criticals

The KRITZ high-temperature critical experiments series (Reference 3-3) provide critical benchmark data for uranium-fueled, water moderated lattices at high temperatures. These experiments were run at temperatures up to 245 °C (473 °F) covering temperatures close to the range used in light water reactor cores. The details of the experiments are provided in Reference 3-3. Twelve KRITZ experiments were modeled in PARAGON. The modeled experiments included two lattice configurations (39x39 and 46x46) over a temperature range from 41.2 to 245.8 °C with boron concentrations from essentially zero to 175 ppm. The axial bucklings provided in the reference were used to calculate K_{eff}. Table 3-2 summarizes the results of the PARAGON calculations for these criticals. For each experiment, the table shows the lattice configuration, the soluble boron concentration, the water temperature, the axial buckling used to determine K_{eff}, and the PARAGON calculated K_{eff}. The mean K_{eff} for all twelve experiments was [ ]^{a,c} with a standard deviation of [ ]^{a,c} The very small standard deviation shows that PARAGON predicts very consistently across the large temperature range of these experiments with no significant trend

3.1.3 Babcock & Wilcox Spatial Criticals

A large physics verification program sponsored by USAEC and Babcock & Wilcox (B&W) was conducted at B&W's Lynchburg Research Center during the 1970's. These experiments, which are documented in References 3-4 and 3-5, provided reactivity and power distribution measurements for typical PWR lattices at cold conditions for various configurations of fuel rods, guide thimbles, and several different burnable absorbers.

Since PARAGON can handle large problems, these experiments were modeled directly in PARAGON. For each experiment, the PARAGON k-infinity was compared to the k-infinity calculated by the Monte Carlo code MCNP for the same configuration. A cross section library developed by Westinghouse based on ENDF/B-VI was used with MCNP for the Monte Carlo calculations in this report. In addition, the axial buckling provided in the references was used with the PARAGON reactivity result to calculate K_{eff}. Details for each configuration are provided in the references.

Table 3-3 presents the PARAGON and MCNP results for B&W Core XI for loadings 1 through 9. Core XI contained low enriched uranium clad in aluminum in a 15x15 lattice. For each of the nine loadings, Table 3-3 shows the number of fuel rods, water rods and Pyrex burnable absorbers, the MCNP calculated k-infinity and standard deviation, the PARAGON calculated k-infinity, and the PARAGON K_{eff} calculated using the axial buckling. The mean PARAGON k-infinity for the nine configurations was [ ]^{a,c} with a standard deviation of [ ]^{a,c} which is within [ ]^{a,c} pcm of the mean MCNP k-infinity of [ ]^{a,c} which has a standard deviation of [ ]^{a,c} The mean PARAGON K_{eff} was [ ]^{a,c} with a standard deviation of [ ]^{a,c} Power distributions for three of these experiments are shown in Figures 3-6 (loading 2), 3-7 (loading 6), and 3-8 (loading 9). The results shown in these figures demonstrate that the predicted PARAGON power distribution agrees very well with measurement with the average difference being about [ ]^{a,c}

Tables 3-4, 3-5, 3-6 and 3-7 present PARAGON results for B&W cores with gadolinia rods, with and without control rods. Table 3-4 shows results for cores with the number of gadolinia rods varying from 0 to 36 in 15x15 lattices of 2.46 w/o enriched fuel. Table 3-5 shows results from the same cores in the presence of B_4C control rods. Table 3-6 shows results from cores with varying number of gadolinia rods (0 to 36) with and without control rods in 15x15 lattices of 4.02 w/o enriched fuel. Table 3-7 simulates a CE 16x16 lattice with 2x2 water rods with 4.02 w/o enriched fuel and from 0 to 32 gadolinia rods. As in the B&W pyrex experiments shown in Table 3-3, MCNP was run for all configurations for k-infinity comparisons to PARAGON. The maximum difference between the mean

MCNP and PARAGON k-infinities for these tables is [ ]^{a,c} The mean PARAGON K_{eff} varies from critical by [ ]^{a,c} The standard deviations are all below [ ]^{a,c}

Comparisons of measured and PARAGON predicted power distributions for three of these experiments are provided in Figures 3-9 (Core 5, 28 gadolinia rods), 3-10 (Core 12, no gadolinia rods), and 3-11 (Core 14, 28 gadolinia rods). As with the pyrex cores, the power distributions of these cores were very well predicted by PARAGON with the mean measured to predicted rod power difference being less than [ ]^{a,c} for all three core configurations.

The reactivity results for all twenty-nine B&W critical experiments were very good with a mean keff of [ ]^{a,c} and a standard deviation of [ ]^{a,c} The average difference between the measured and PARAGON power distribution for the six experiments shown in Figures 3-6 through 3-11 was [ ]^{a,c} per cent with an average standard deviation of [ ]^{a,c} per cent.

3.2 Monte Carlo Assembly Benchmarks

Thirteen different assembly configurations were calculated in both PARAGON and the Monte Carlo code MCNP. These assembly configurations were chosen to cover a variety of lattice types, burnable absorbers, a large enrichment range and both UO_2 and MOX. Specifically, the following describes the parameter range covered by these configurations:

Lattice types:	Westinghouse	14x14, 15x15, 16x16, 17x17
	Combustion Engineering	14x14, 16x16
Burnable absorbers:		Integral Fuel Burnable Absorber (IFBA), gadolinia (Gd_2O_3), erbia (Er_2O_3)
Enrichment:		2.10 to 5.00 w/o
Fuel:		UO_2 and MOX

Table 3-8 presents the reactivity results of these assembly calculations. For each assembly configuration, the table presents the lattice type, the enrichment, the number and type of burnable absorber present, the MCNP calculated k-infinity, the PARAGON calculated k-infinity and the difference in pcm between the PARAGON and MCNP k-infinities. As can be seen from the table, the mean difference between the PARAGON and MCNP k-infinities was very good at [ ]^{a,c} with a standard deviation of [ ]^{a,c} The largest difference is for the MOX assembly at [ ]^{a,c} The agreement for the gadolinia assembly is very good at [ ]^{a,c}

Figures 3-12 through 3-24 present comparisons between MCNP and PARAGON rod power distributions for the thirteen assemblies listed in Table 3-8. For each power distribution figure, three statistical quantities are listed: 1) the maximum difference between the MCNP and PARAGON rod powers , 2) the average deviation from the mean of the rod power differences, and 3) the standard deviation of the rod power differences. These figures demonstrate that PARAGON rod power predictions are well predicted. The average rod power differences ranged from [ ]^{a,c} Sufficient histories were run so that the MCNP standard deviation for each rod power was less than [ ]^{a,c} in all cases.

3.3 Saxton and Yankee Isotopics Data

The spectrograph-measured isotopics data for Saxton Cores 2 and 3 with mixed oxide fuel, Yankee cores 1, 2, and 4 with stainless steel clad fuel, and Yankee Core 5 with zircaloy clad fuel have been compared to PARAGON isotopic concentrations. The measured data for these isotopics are documented in References 3-6, 3-7, 3-8, and 3-9 (Saxton) and 3-10 and 3-11 (Yankee). Since the

measured fuel rods for both the Saxton and Yankee cases were far enough away from lattice heterogeneities that they were exposed to the asymptotic flux spectrum, PARAGON pin cell calculations were used for these comparisons. The pin cell cases were set up to approximate the core operating history for each isotopic data set.

The Saxton Cores 2 and 3 isotopic comparisons for the major isotopes are shown in Figures 3-25 through 3-37. Comparisons for the Yankee Cores 1,2, and 4 stainless steel clad UO_2 fuel isotopics are shown in Figures 3-38 through 3-50 Comparisons for Yankee Core 5 zircaloy clad UO_2 fuel isotopics are shown in Figures 3-51 through 3-63.

As noted in Reference 3-1, the Saxton isotopic case was particularly challenging since it is for a mixture of PuO_2 in a natural uranium matrix. In addition, the wet fraction was changed at an intermediate burnup due to the removal of fuel rods for isotopics measurements. As seen in the figures, PARAGON matches the measured values both in shape and magnitude.

The Yankee core data represent a typical UO_2 light water lattice with two clad materials. The figures comparing measured to PARAGON isotopics for these data also show very good agreement throughout the isotopic burnup range.

The isotopic comparisons for both the Saxton and Yankee isotopics show no significant trend for any isotope with burnup. These excellent results demonstrate the capability of PARAGON for predicting the depletion characteristics of both UO_2 and PuO_2 LWR fuel over a wide range of burnup conditions.

Table 3-1: Strawbridge –Barry Critical Experiment Data versus PARAGON predictions

Experiment Group	Number of Data Points	Mean Keff	Standard Deviation	
Hexagonal lattice	[			a, b, c
Square lattice				
Aluminum clad				
Stainless Steel clad				
No Clad				
Dissolved boron				
No Boron				
UO2 experiments				
Uranium metal experiments				
All				]

Table 3-2: PARAGON Keff for KRITZ Experiments

[a, b, c]

Table 3-3: Results for B&W Core XI with PYREX rods

[ ] a, b, c

Table 3-4: Results for B&W Cores with 2.46 w/o U^{235} and Gadolinia Rods

[ ] a, b, c

Table 3-5: Results from B&W Cores with 2.46 w/o U235, Gadolinia Rods and Control Rods

[ ] a, b, c

Table 3-6: Results from B&W Cores wih 4.02 w/o U235, Gadolinia Rods and Control Rods

[ ] a, b, c

Table 3-7: Results from B&W Cores with 4.02 w/o U235, CE 16x16 Lattice with 2x2 Water Rods

[ ] a, b, c

Table 3-8: Results of Assembly Benchmarks

a, b, c

Figure 3-1: Strawbridge-Barry Critical Experiments:PARAGON Prediction versus Lattice Water to Uranium Ratio

a, b, c

Figure 3-2: Strawbridge-Barry Critical Experiments: PARAGON Prediction versus Fuel Enrichment

a, b, c

Figure 3-3: Strawbridge-Barry Critical Experiments: PARAGON Prediction versus Pellet Diameter

a, b, c

Figure 3-4: Strawbridge-Barry Critical Experiments: PARAGON Prediction versus Experimental Buckling

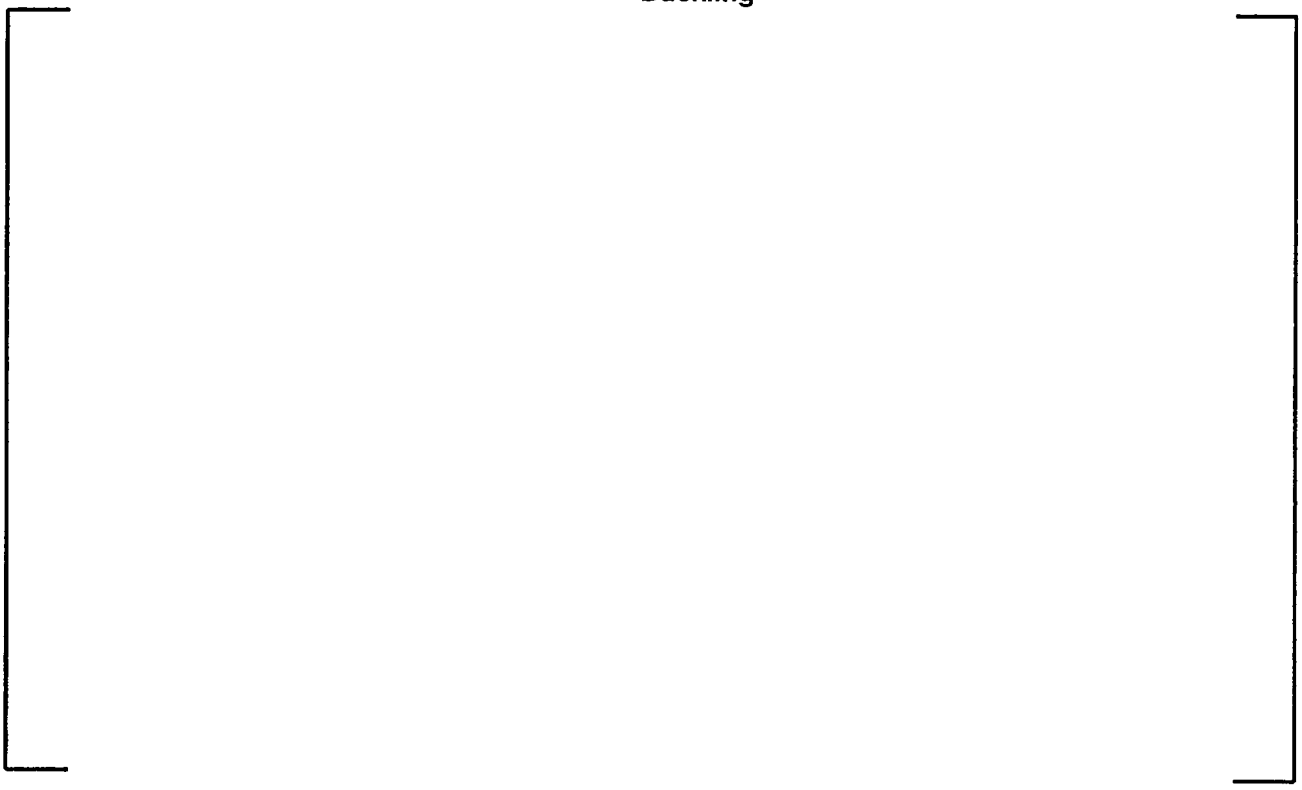

a, b, c

Figure 3-5: Strawbridge-Barry Critical Experiments: PARAGON Prediction versus Soluble Boron Concentration

a, b, c

Figure 3-6: Babcock & Wilcox Critical Experiments: Core XI, Loading 2 Center Assembly Rod Power Distribution

a, b, c

Figure 3-7: Babcock & Wilcox Critical Experiments: Core XI, Loading 6 Center Assembly Rod Power Distribution

a, b, c

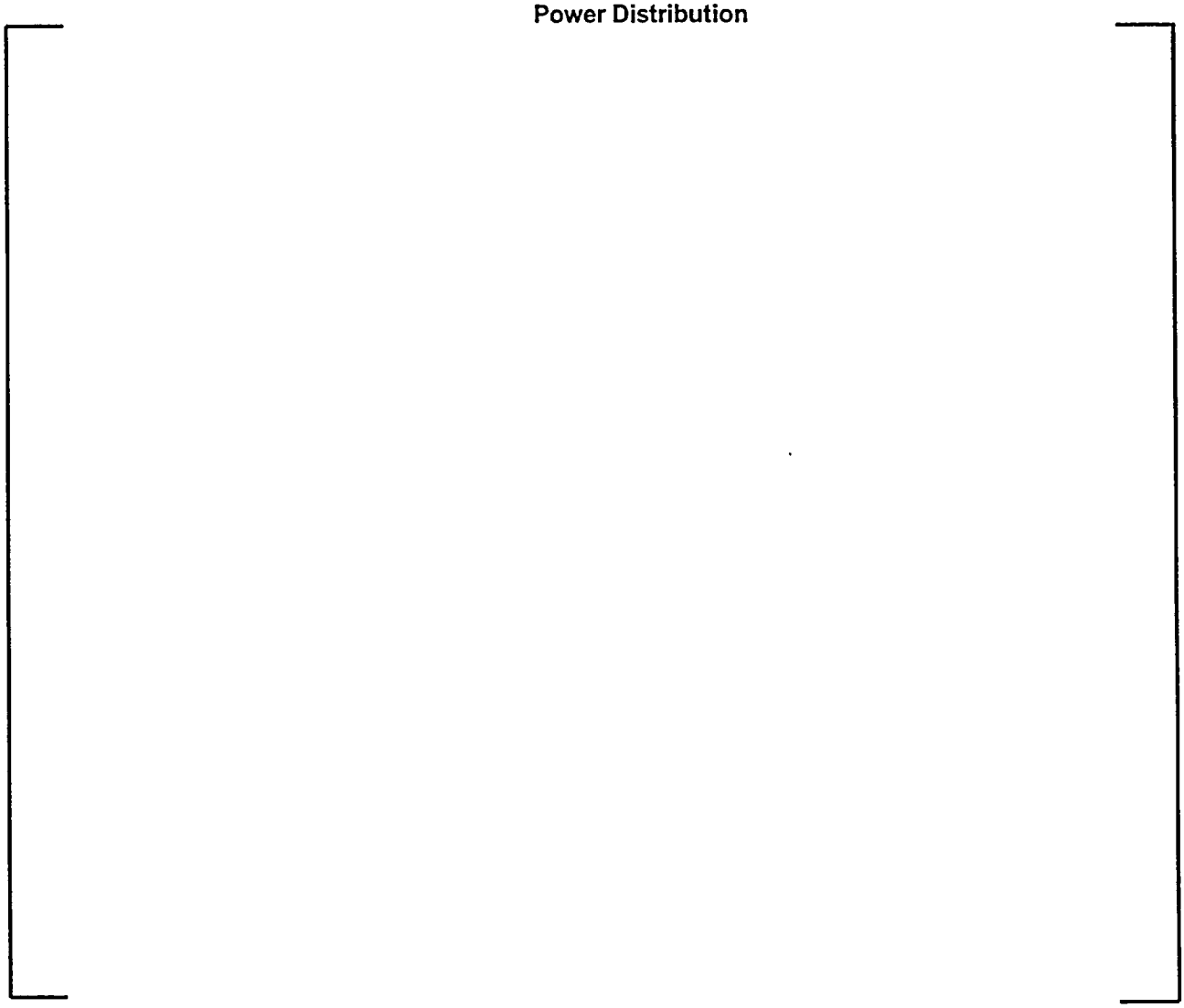

Figure 3-8: Babcock & Wilcox Critical Experiments: Core XI, Loading 9
Center Assembly Rod Power Distribution

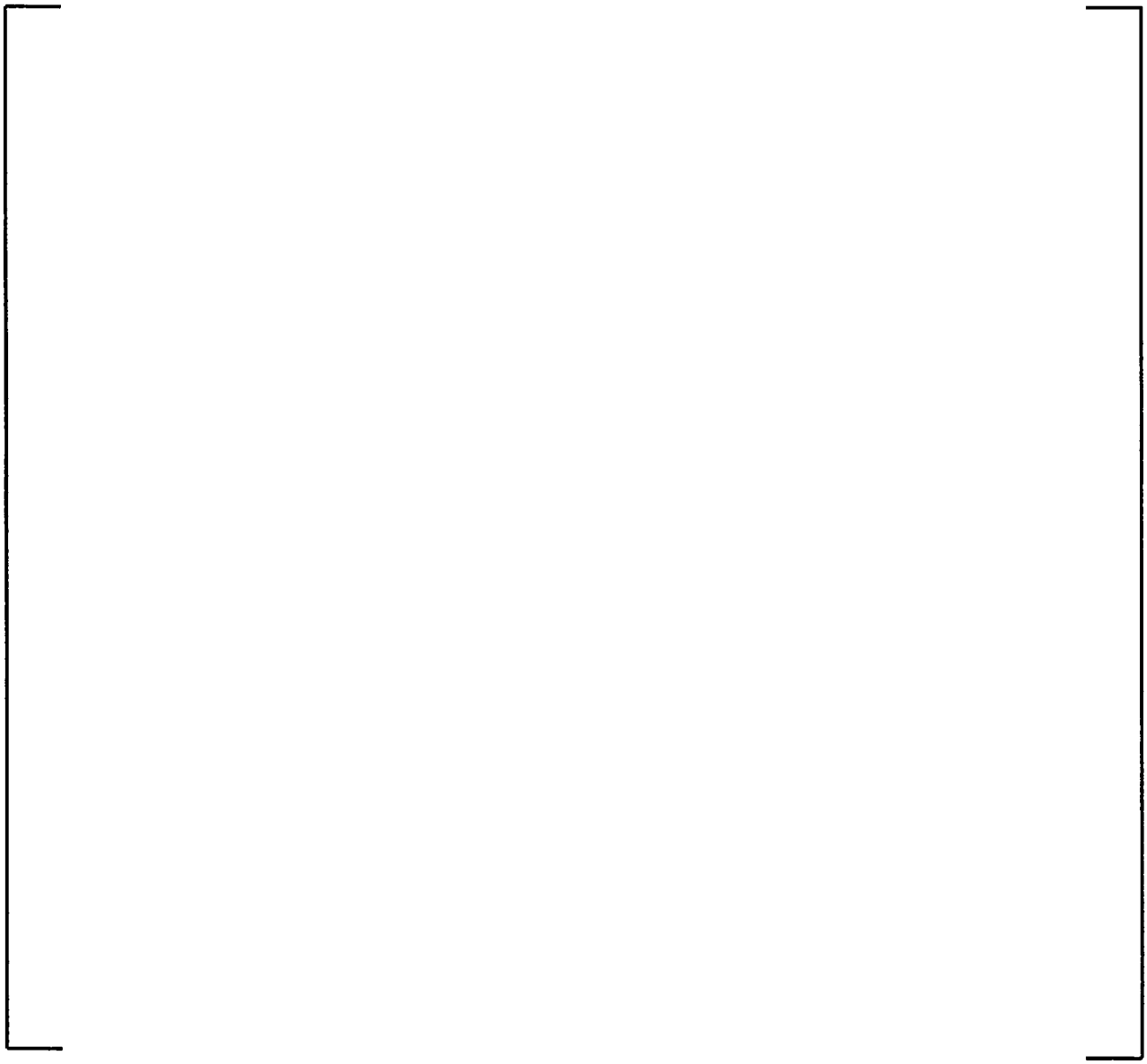

a, b, c

Figure 3-9: Babcock & Wilcox Critical Experiments: Core 5, 28 Gadolinia Rods Center Assembly Rod Power Distribution

a, b, c

Figure 3-10: Babcock & Wilcox Critical Experiments: Core 12, No Gadolinia Rods
Center Assembly Rod Power Distribution

a, b, c

Figure 3-11: Babcock & Wilcox Critical Experiments: Core 14, 28 Gadolinia Rods Center Assembly Rod Power Distribution

a, b, c

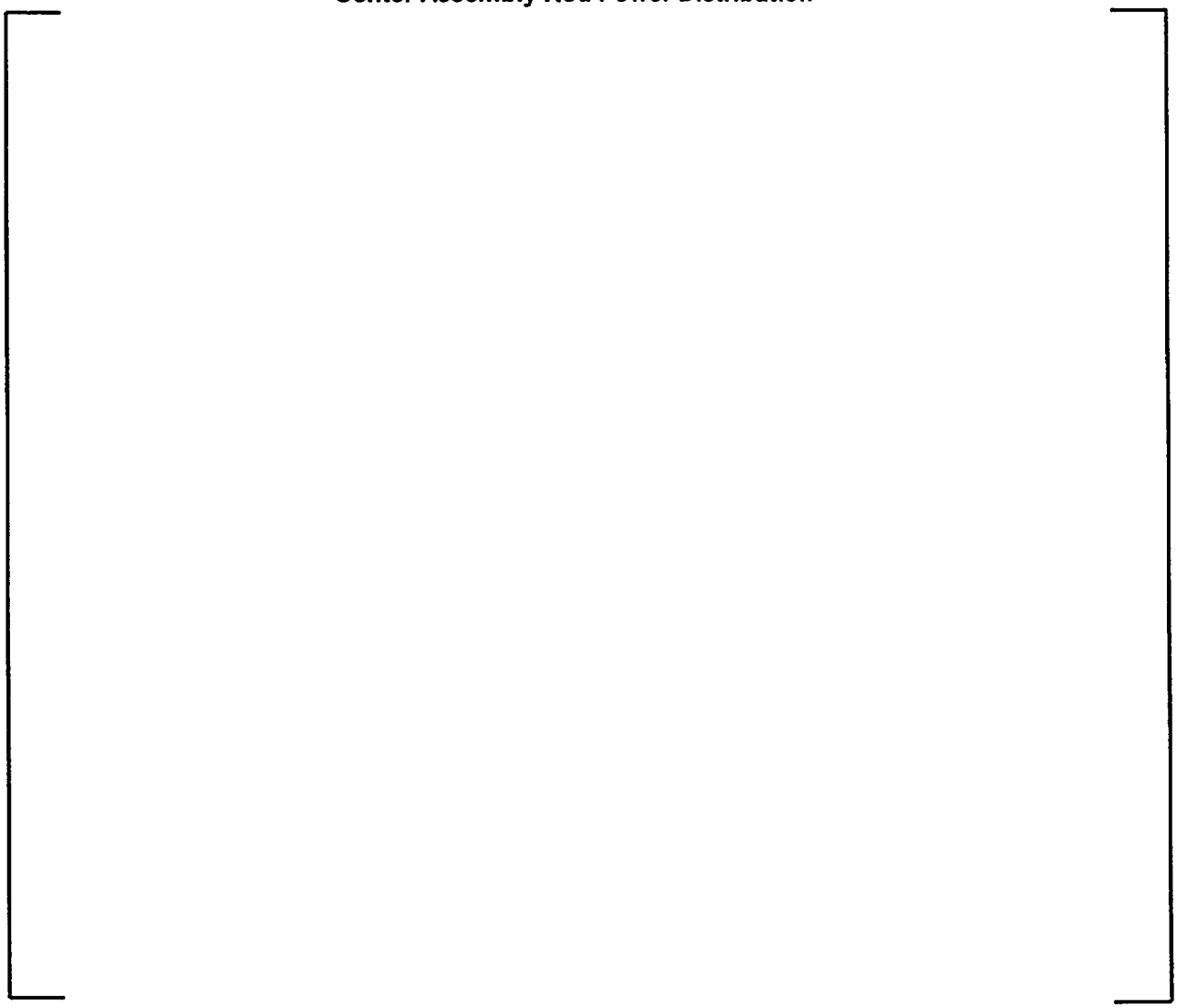

Figure 3-12: MCNP vs PARAGON: 14x14 Westinghouse Assembly (4.00 w/o No BA) Assembly Rod Power Distribution

a, b, c

Figure 3-13: MCNP vs PARAGON: 15x15 Westinghouse Assembly (3.90 w/o No BA) Assembly Rod Power Distribution

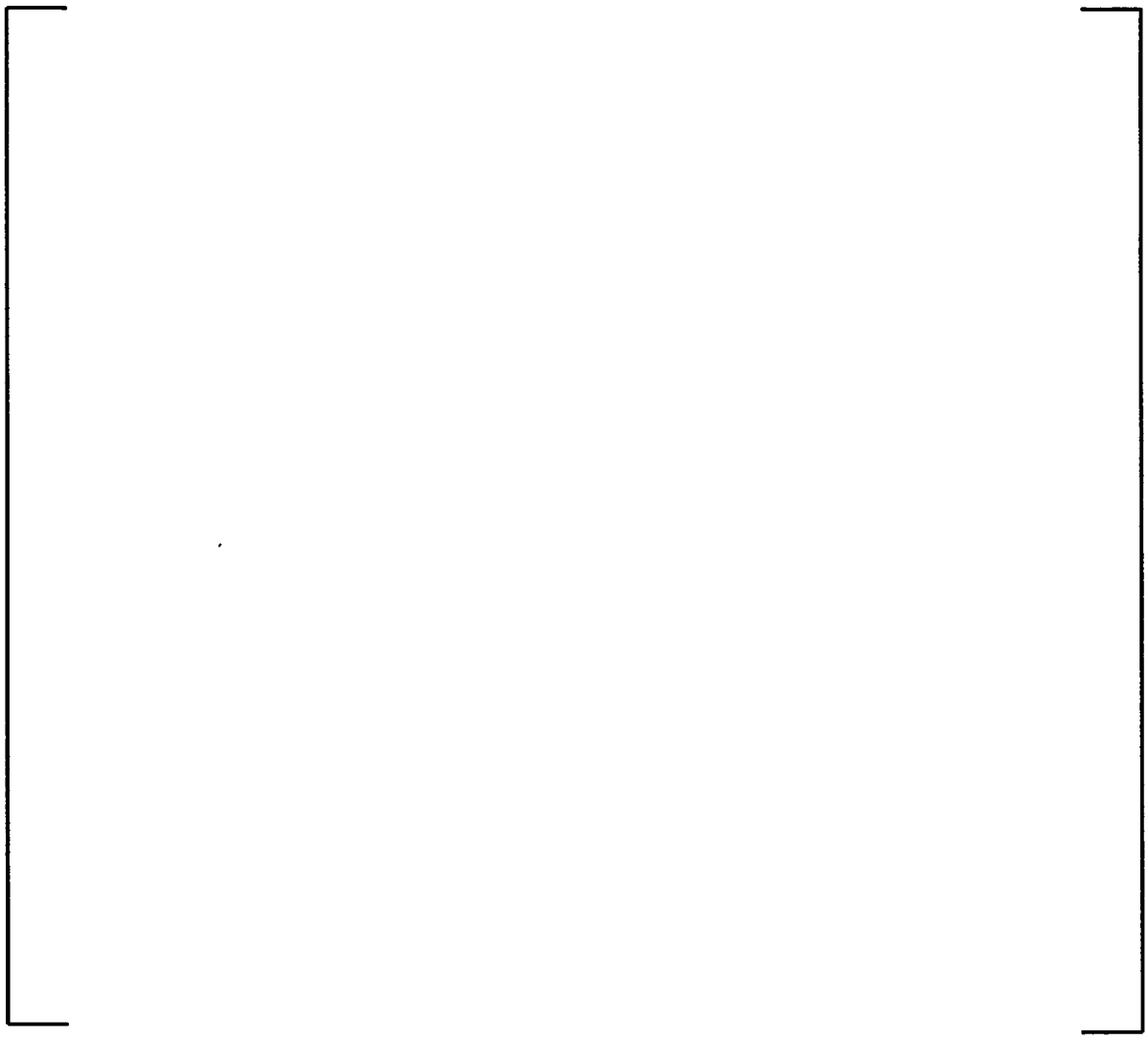

a, b, c

Figure 3-14: MCNP vs PARAGON: 15x15 Westinghouse Assembly (5.0 w/o 60 IFBA) Assembly Rod Power Distribution

a, b, c

Figure 3-15: MCNP vs PARAGON: 16x16 Westinghouse Assembly (4.00 w/o No BA) Assembly Rod Power Distribution

[ ]a, b, c

Figure 3-16: MCNP vs PARAGON: 17x17 Standard Westinghouse Assembly (2.10 w/o No BA)
Assembly Rod Power Distribution

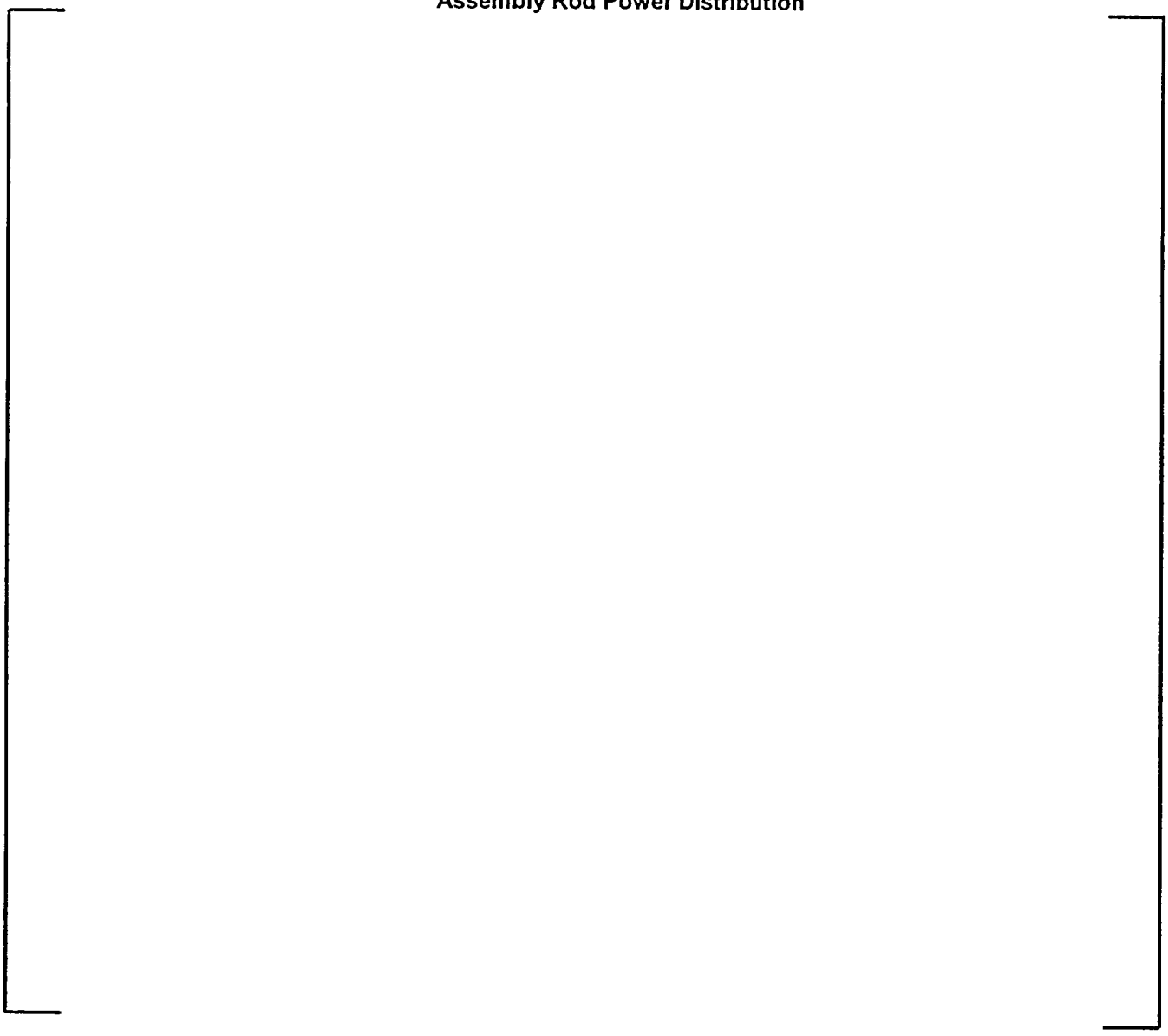

a, b, c

Figure 3-17: MCNP vs PARAGON: 17x17 Standard Westinghouse Assembly (4.10 w/o No BA)
Assembly Rod Power Distribution

a, b, c

Figure 3-18: MCNP vs PARAGON: 17x17 OFA Westinghouse Assembly (4.70 w/o 156 IFBA)
Assembly Rod Power Distribution

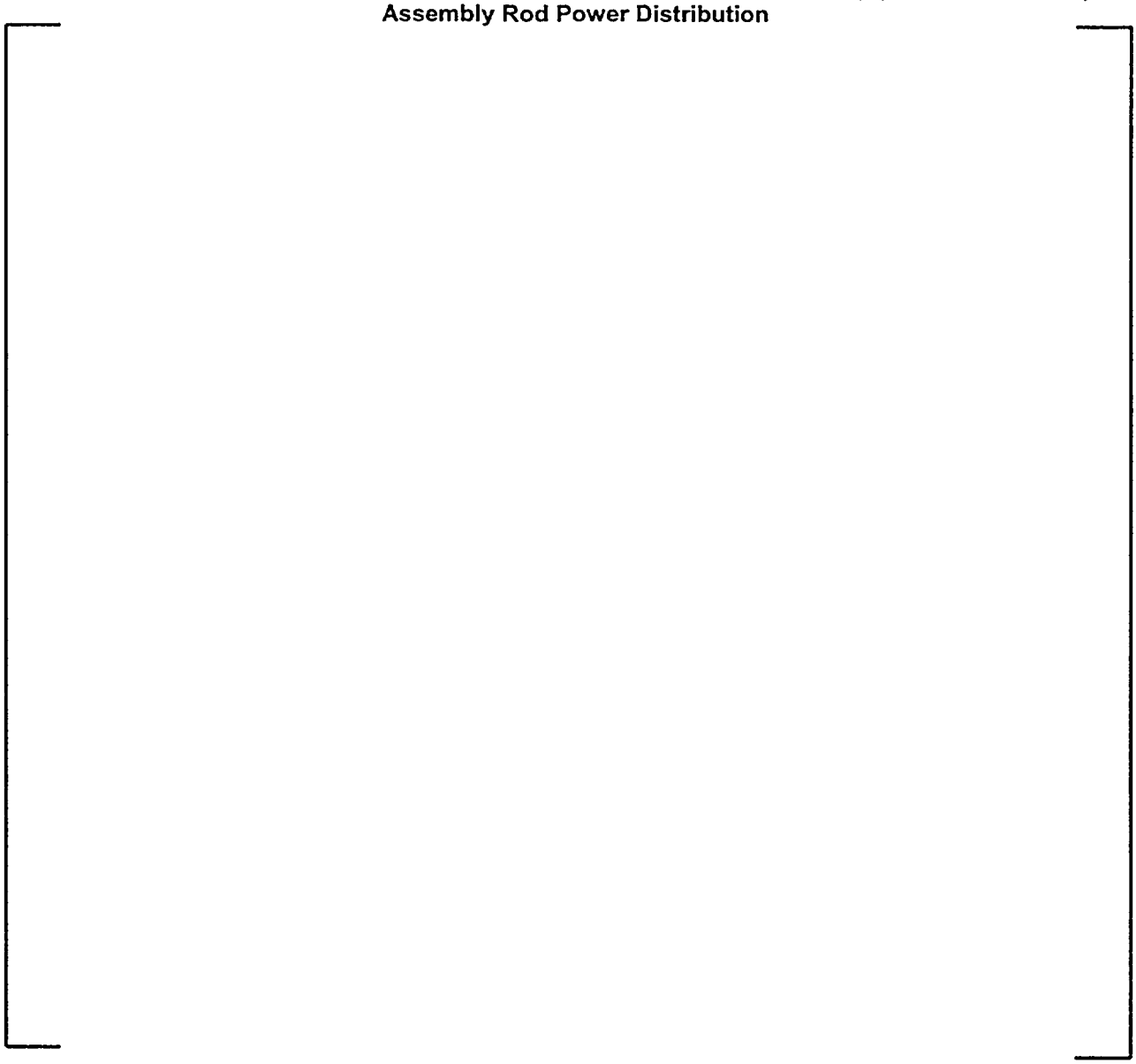

a, b, c

Figure 3-19: MCNP vs PARAGON: 17x17 Standard Westinghouse Assembly (5.0 w/o 128 IFBA)
Assembly Rod Power Distribution

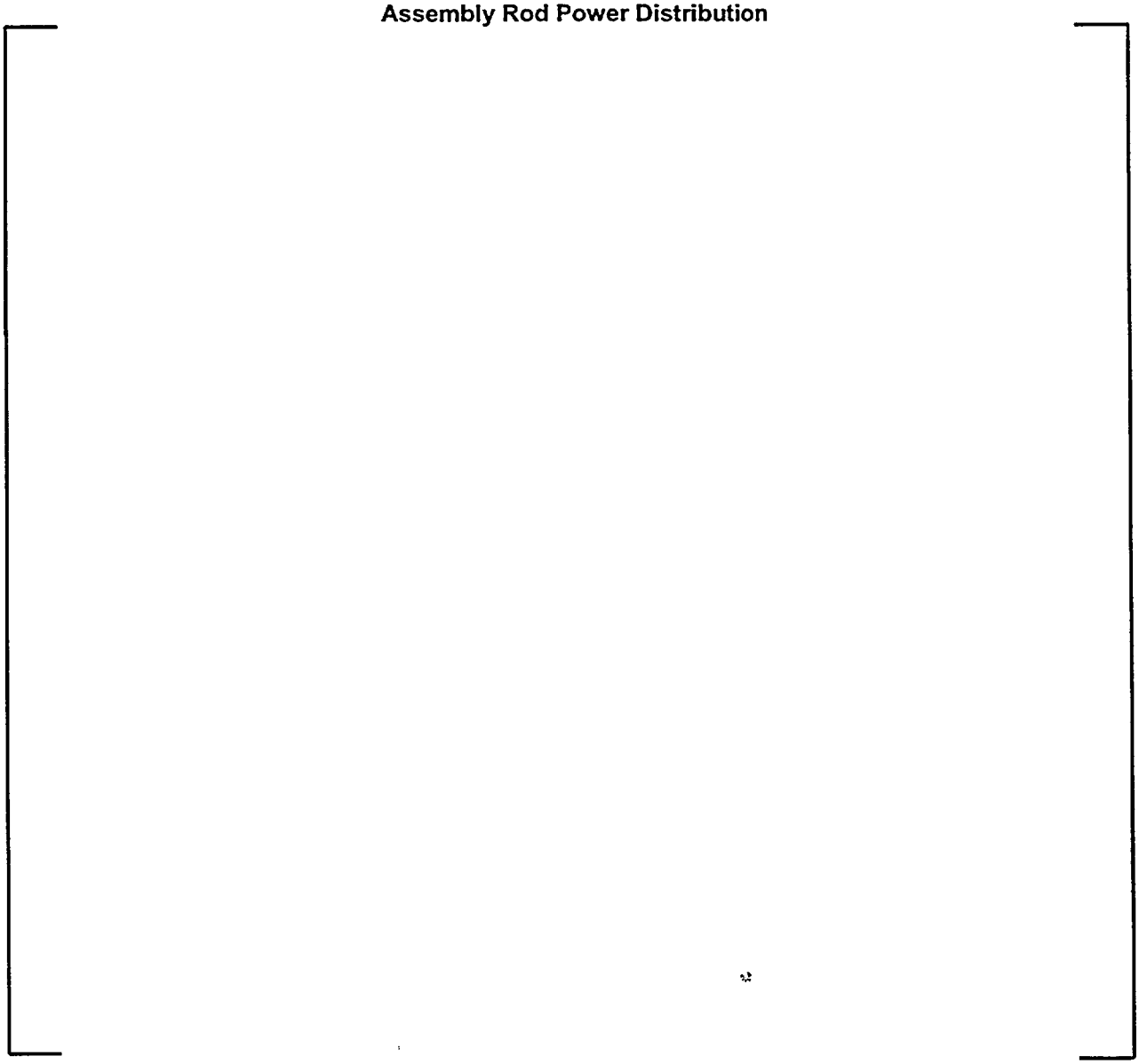

a, b, c

Figure 3-20: MCNP vs PARAGON: 17x17 Standard Westinghouse Assembly (4.00 w/o 24 Gd_2O_3 Rods) Assembly Rod Power Distribution

a, b, c

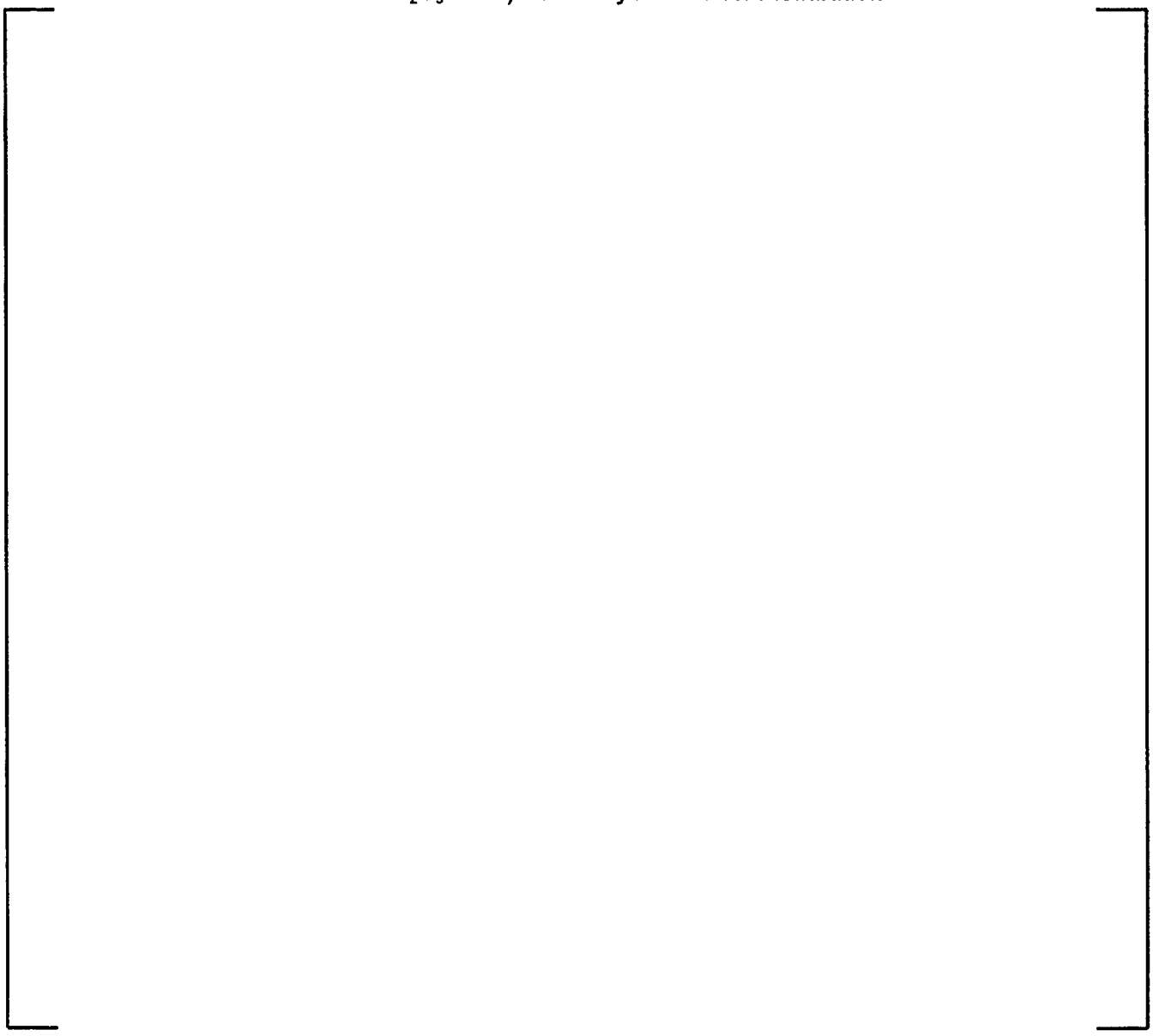

Figure 3-21: MCNP vs PARAGON: 17x17 Standard Westinghouse Assembly (6.1 w/o MOX, No BA) Assembly Rod Power Distribution

a, b, c

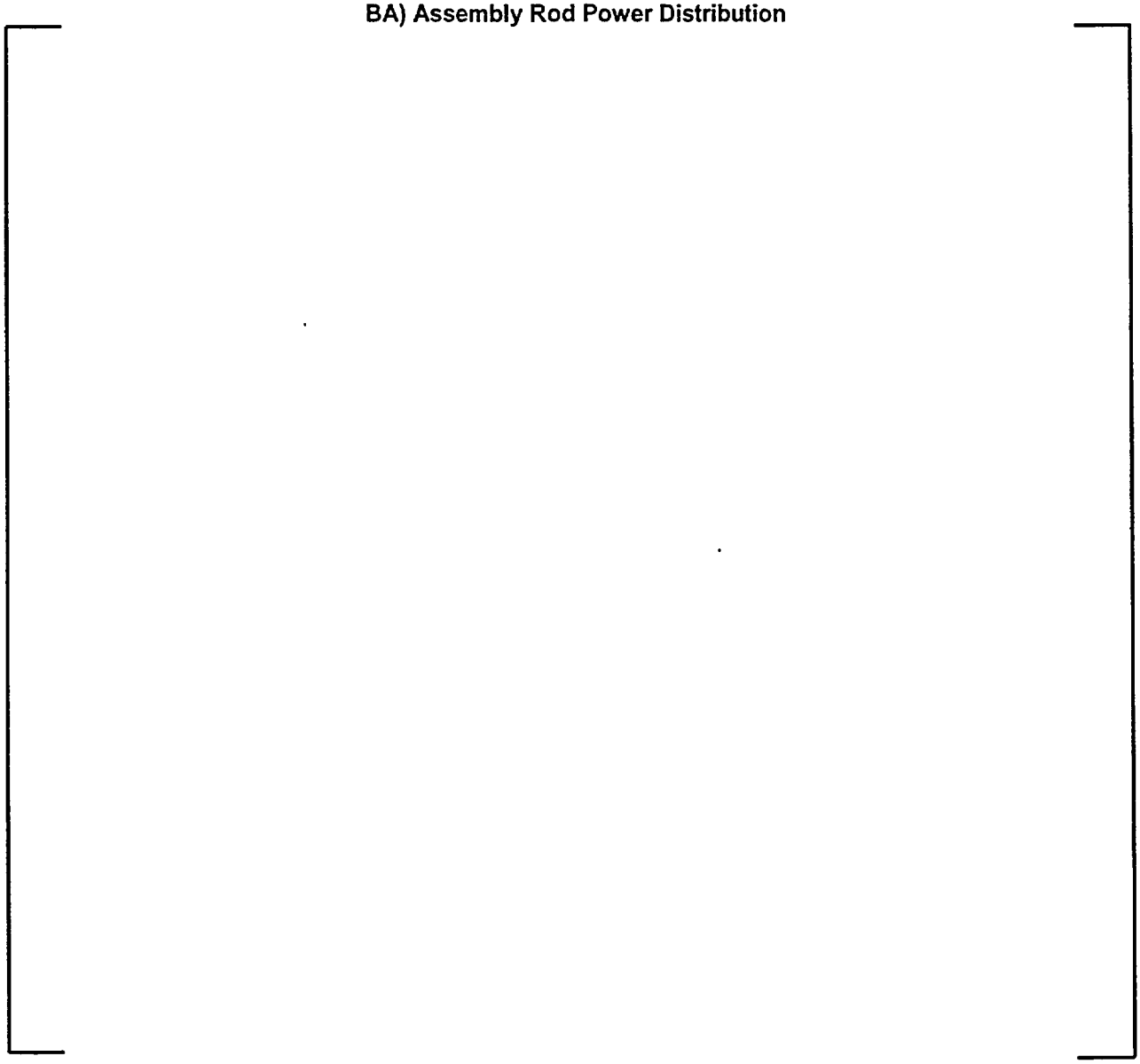

Figure 3-22: MCNP vs PARAGON: 17x17 OFA Westinghouse Assembly (4.00 w/o 72 Er_2O_3 Rods) Assembly Rod Power Distribution

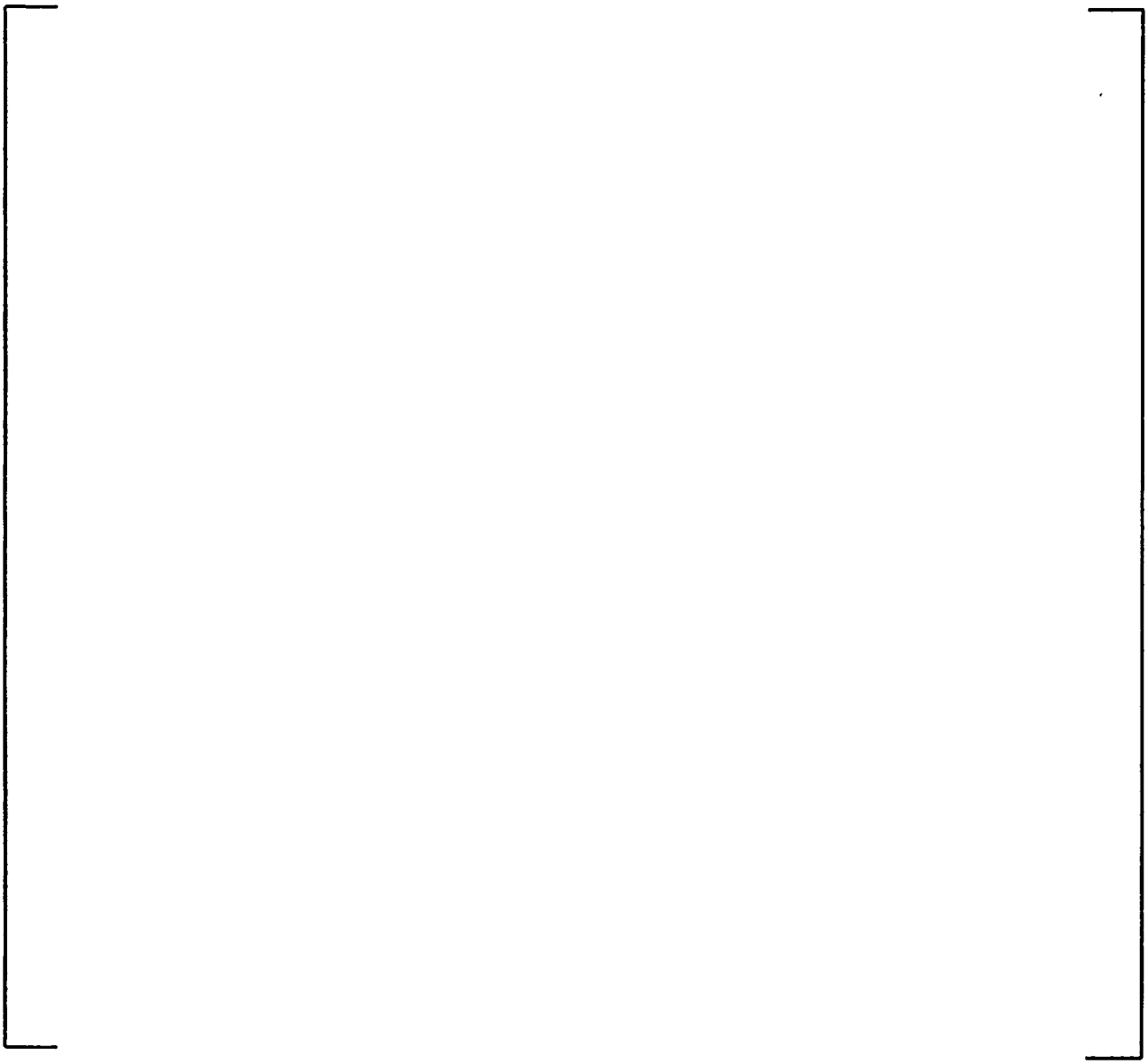

a, b, c

Figure 3-23: MCNP vs PARAGON: 14x14 CE Assembly (4.30,3.40 w/o 44 Er_2O_3 Rods) Assembly Rod Power Distribution

a, b, c

Figure 3-24: MCNP vs PARAGON: 16x16 CE Assembly (4.05,3.65 w/o 52 Er_2O_3 Rods) Assembly Rod Power Distribution

a, b, c

Figure 3-25: Saxton Fuel Performance Evaluation Program: PARAGON U^{235}/U Prediction Versus Burnup

a, b, c

Figure 3-26: Saxton Fuel Performance Evaluation Program: PARAGON U^{236}/U Prediction Versus Burnup

a, b, c

Figure 3-27: Saxton Fuel Performance Evaluation Program: PARAGON U^{238}/U Prediction Versus Burnup

Figure 3-28: Saxton Fuel Performance Evaluation Program: PARAGON Pu^{239}/Pu Prediction Versus Burnup

Figure 3-29: Saxton Fuel Performance Evaluation Program: PARAGON Pu^{240}/Pu Prediction Versus Burnup

Figure 3-30: Saxton Fuel Performance Evaluation Program: PARAGON Pu^{241}/Pu Prediction Versus Burnup

Figure 3-31: Saxton Fuel Performance Evaluation Program: PARAGON Pu^{242}/Pu Prediction Versus Burnup

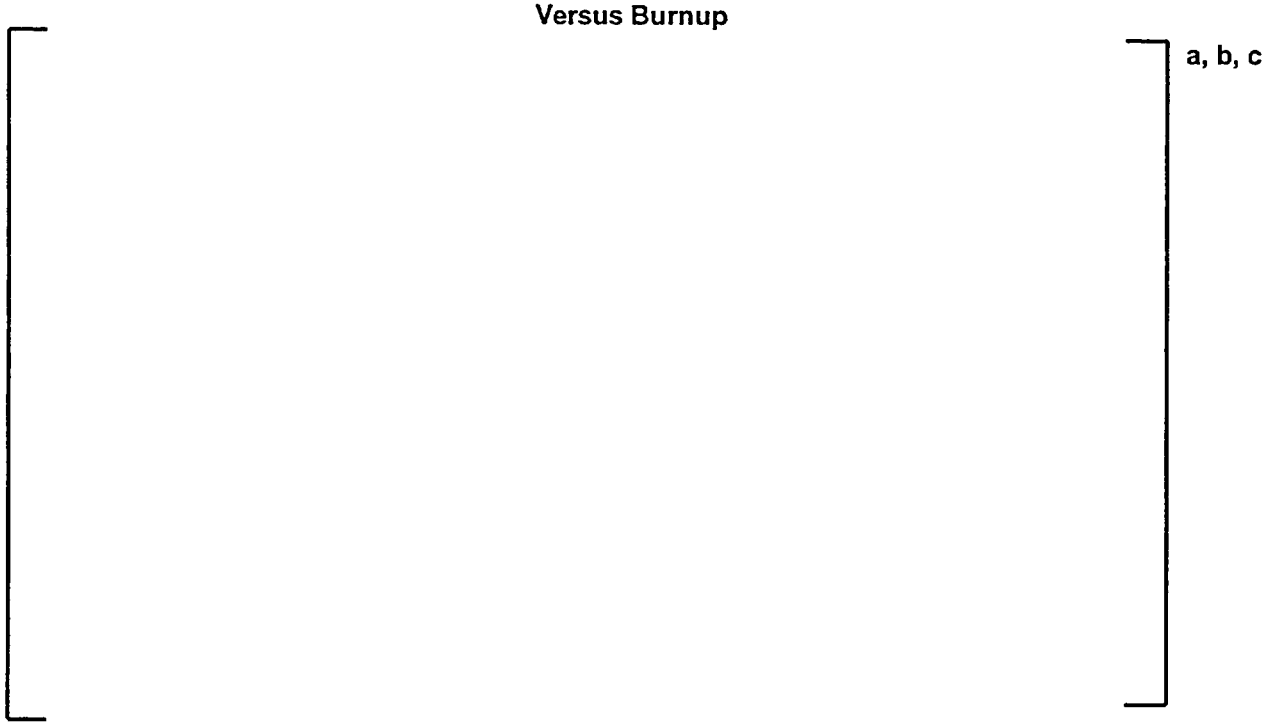

Figure 3-32: Saxton Fuel Performance Evaluation Program: PARAGON Pu^{239}/U^{238} Prediction Versus Burnup

Figure 3-33: Saxton Fuel Performance Evaluation Program: PARAGON Pu^{239}/Pu^{240} Prediction Versus Burnup

a, b, c

Figure 3-34: Saxton Fuel Performance Evaluation Program: PARAGON Pu^{240}/Pu^{241} Prediction Versus Burnup

a, b, c

Figure 3-35: Saxton Fuel Performance Evaluation Program: PARAGON Pu^{241}/Pu^{242} Prediction Versus Burnup

[a, b, c]

Figure 3-36: Saxton Fuel Performance Evaluation Program: PARAGON U^{236}/U^{235} Prediction Versus Burnup

[a, b, c]

Figure 3-37: Saxton Fuel Performance Evaluation Program: PARAGON U^{235}/U^{238} Prediction Versus Burnup

[a, b, c]

Figure 3-38: Yankee Core Evaluation Program (Stainless Steel Clad): PARAGON U^{235}/U Prediction Versus Burnup

[a, b, c]

Figure 3-39: Yankee Core Evaluation Program (Stainless Steel Clad): PARAGON U^{236}/U Prediction Versus Burnup

Figure 3-40: Yankee Core Evaluation Program (Stainless Steel Clad): PARAGON U^{238}/U Prediction Versus Burnup

Figure 3-41: Yankee Core Evaluation Program (Stainless Steel Clad): PARAGON Pu^{239}/Pu Prediction Versus Burnup

Figure 3-42: Yankee Core Evaluation Program (Stainless Steel Clad): PARAGON Pu^{240}/Pu Prediction Versus Burnup

Figure 3-43: Yankee Core Evaluation Program (Stainless Steel Clad): PARAGON Pu^{241}/Pu Prediction Versus Burnup

Figure 3-44: Yankee Core Evaluation Program (Stainless Steel Clad): PARAGON Pu^{242}/Pu Prediction Versus Burnup

Figure 3-45: Yankee Core Evaluation Program (Stainless Steel Clad): PARAGON Pu^{239}/U^{238} Prediction Versus Burnup

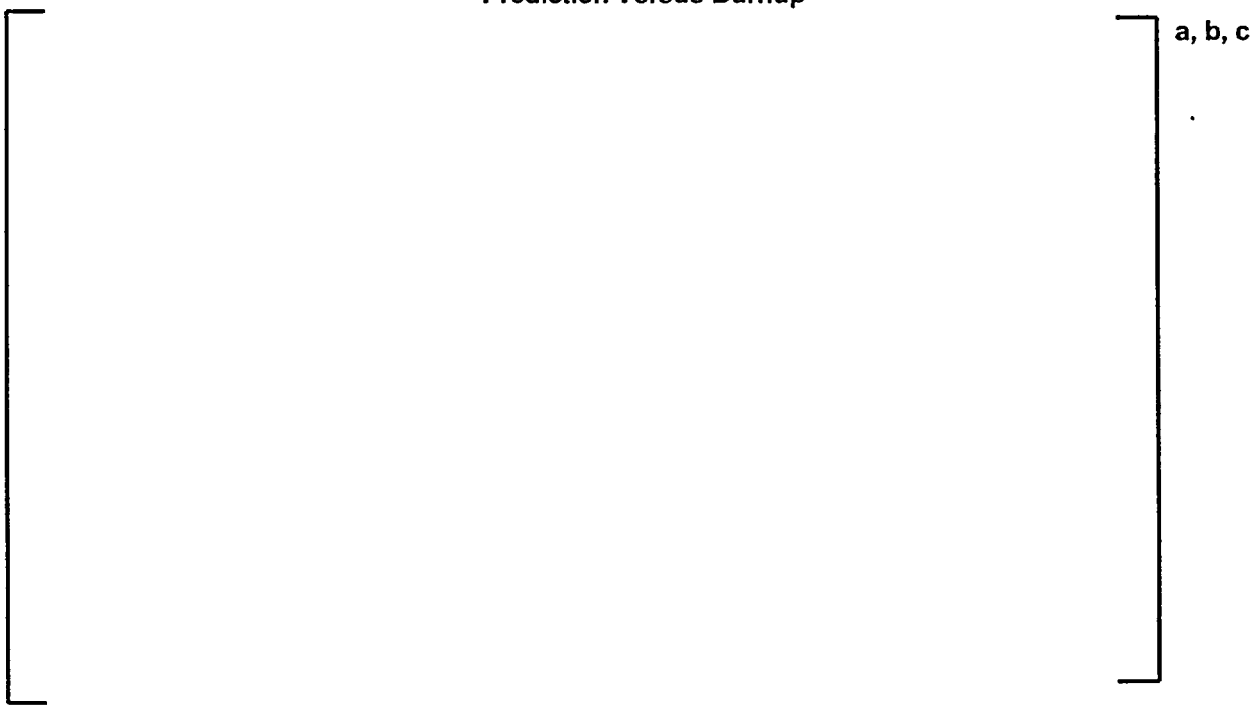

a, b, c

Figure 3-46: Yankee Core Evaluation Program (Stainless Steel Clad): PARAGON Pu^{239}/Pu^{240} Prediction Versus Burnup

a, b, c

Figure 3-47: Yankee Core Evaluation Program (Stainless Steel Clad): PARAGON Pu^{240}/Pu^{241} Prediction Versus Burnup

Figure 3-48: Yankee Core Evaluation Program (Stainless Steel Clad): PARAGON Pu^{241}/Pu^{242} Prediction Versus Burnup

Figure 3-49: Yankee Core Evaluation Program (Stainless Steel Clad): PARAGON U^{236}/U^{235} Prediction Versus Burnup

a, b, c

Figure 3-50: Yankee Core Evaluation Program (Stainless Steel Clad): PARAGON U^{235}/U^{238} Prediction Versus Burnup

a, b, c

Figure 3-51: Yankee Core Evaluation Program (Zircaloy Clad): PARAGON U^{235}/U Prediction Versus Burnup

Figure 3-52: Yankee Core Evaluation Program (Zircaloy Clad): PARAGON U^{236}/U Prediction Versus Burnup

Figure 3-53: Yankee Core Evaluation Program (Zircaloy Clad): PARAGON U^{238}/U Prediction Versus Burnup

Figure 3-54: Yankee Core Evaluation Program (Zircaloy Clad): PARAGON Pu^{239}/Pu Prediction Versus Burnup

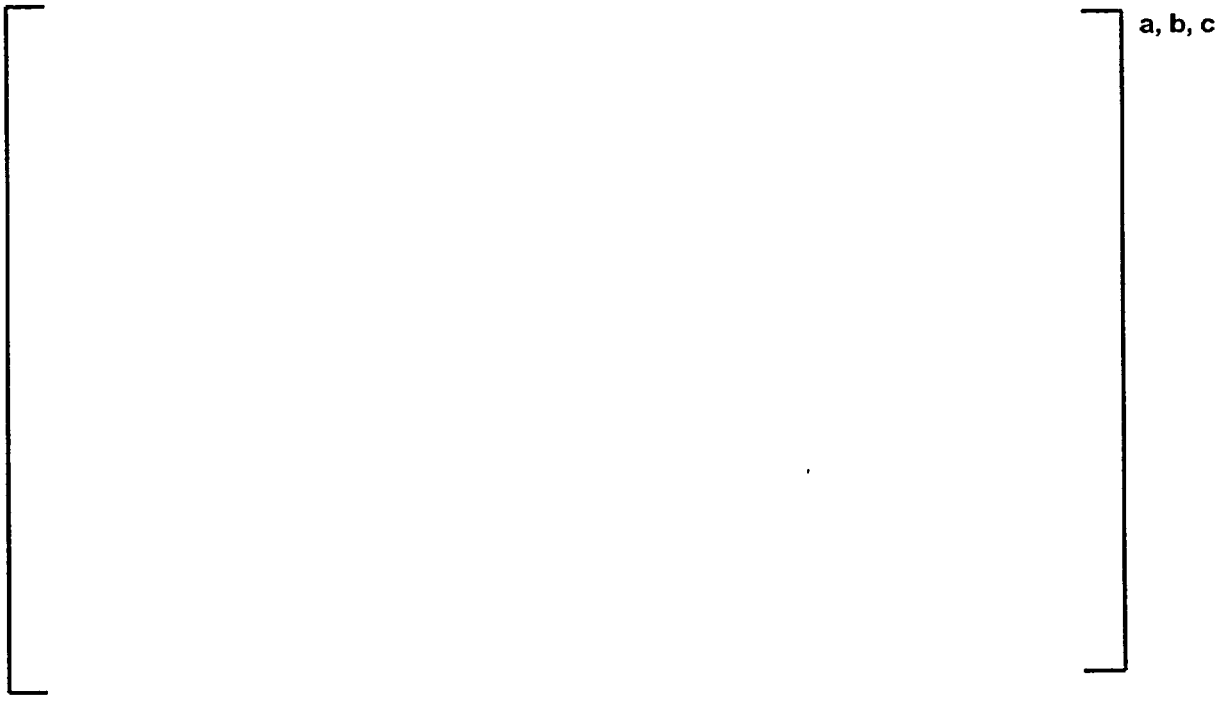

Figure 3-55: Yankee Core Evaluation Program (Zircaloy Clad): PARAGON Pu^{240}/Pu Prediction Versus Burnup

Figure 3-56: Yankee Core Evaluation Program (Zircaloy Clad): PARAGON Pu^{241}/Pu Prediction Versus Burnup

Figure 3-57: Yankee Core Evaluation Program (Zircaloy Clad): PARAGON Pu^{242}/Pu Prediction Versus Burnup

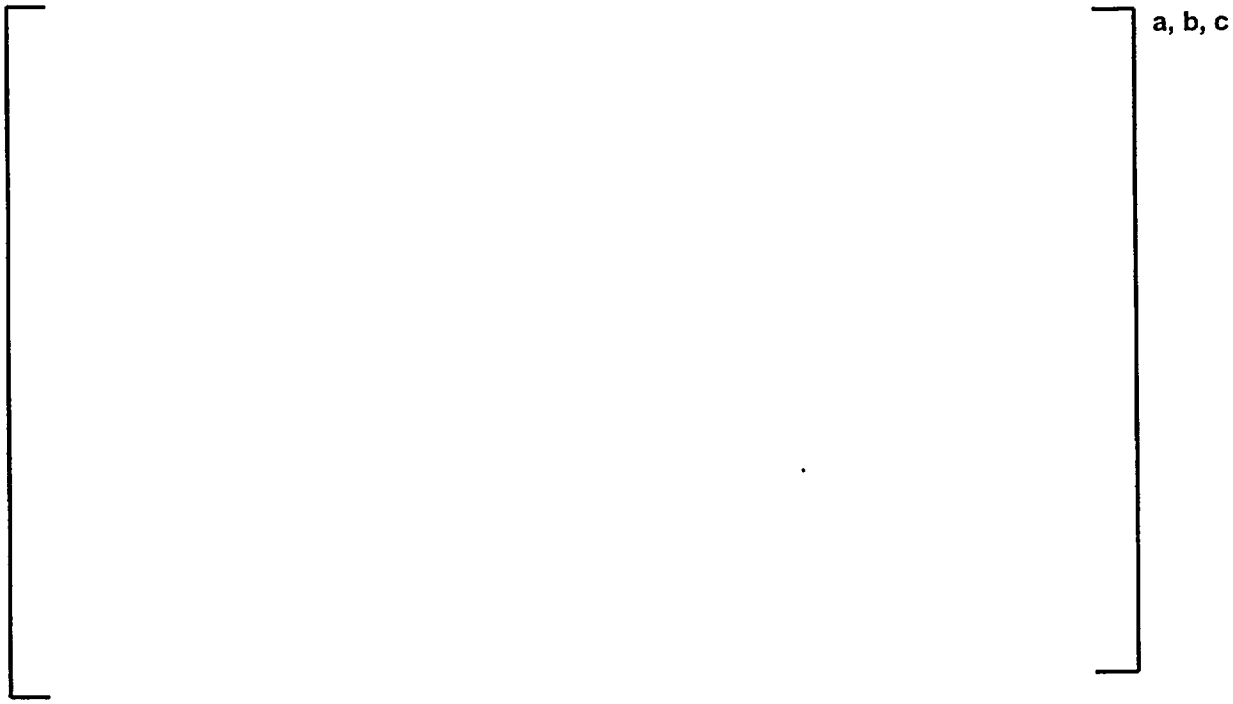

a, b, c

Figure 3-58: Yankee Core Evaluation Program (Zircaloy Clad): PARAGON Pu^{239}/U^{238} Prediction Versus Burnup

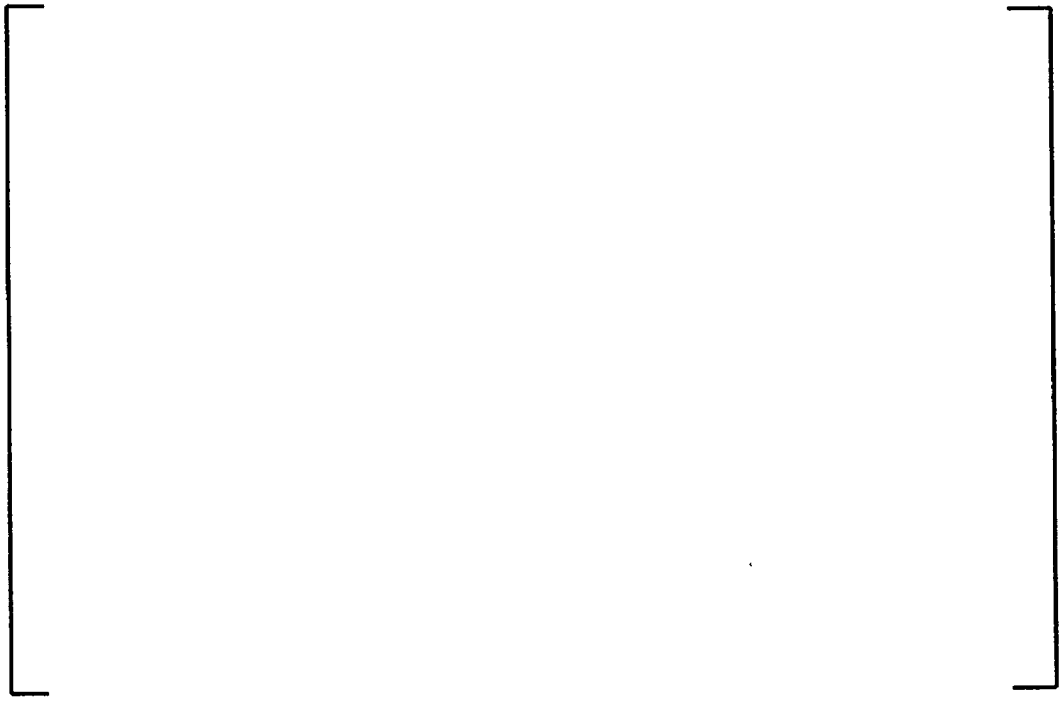

a, b, c

Figure 3-59: Yankee Core Evaluation Program (Zircaloy Clad): PARAGON Pu^{239}/Pu^{240} Prediction Versus Burnup

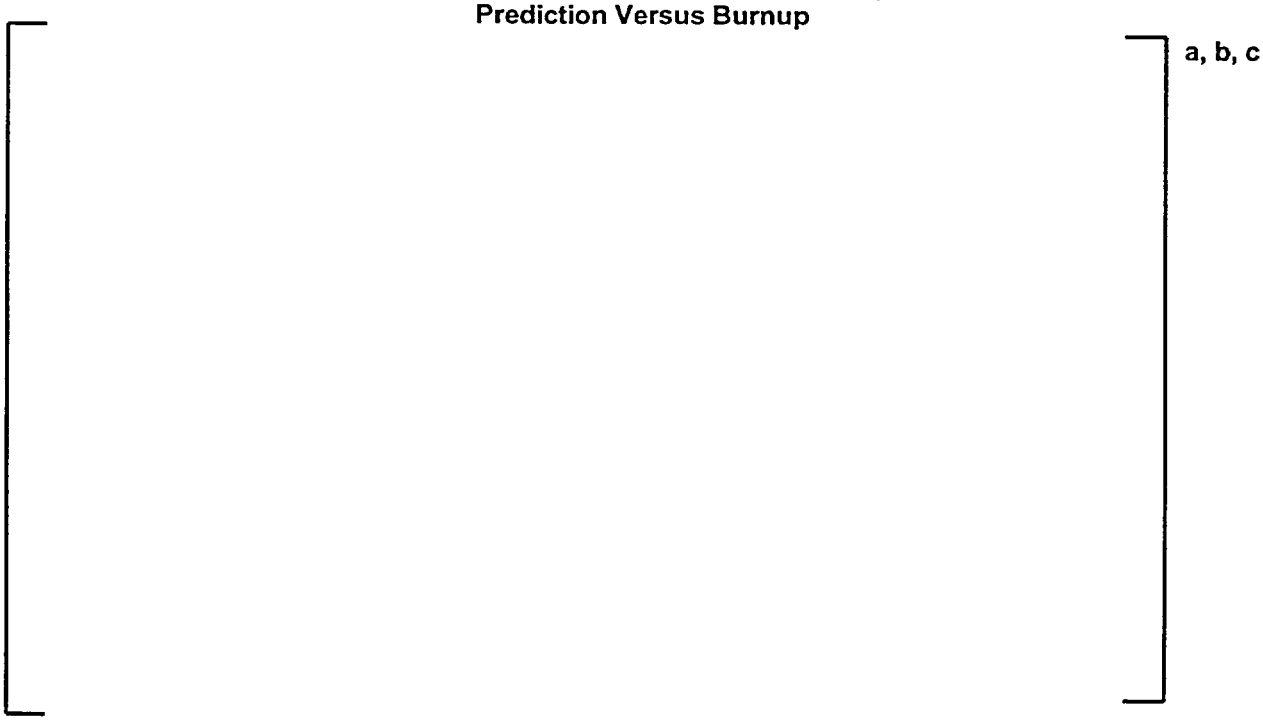

Figure 3-60: Yankee Core Evaluation Program (Zircaloy Clad): PARAGON Pu^{240}/Pu^{241} Prediction Versus Burnup

Figure 3-61: Yankee Core Evaluation Program (Zircaloy Clad): PARAGON Pu^{241}/Pu^{242} Prediction Versus Burnup

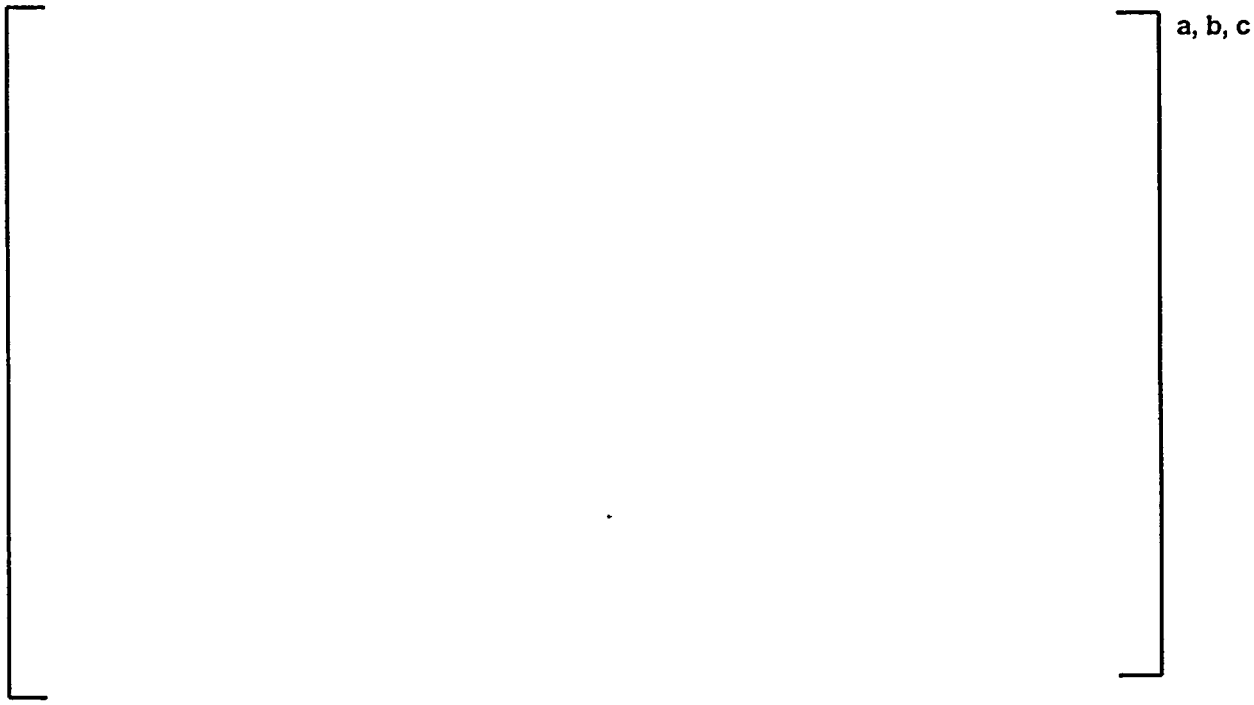

Figure 3-62: Yankee Core Evaluation Program (Zircaloy Clad): PARAGON U^{236}/U^{235} Prediction Versus Burnup

Figure 3-63: Yankee Core Evaluation Program (Zircaloy Clad): PARAGON U^{235}/U^{238} Prediction Versus Burnup

[a, b, c]

Section 4.0: Plant Qualification

The basic methodology of PARAGON was qualified in Section 3 by demonstrating the accuracy of the code in predicting the results of critical experiments and isotopic evaluations. However, the primary use of PARAGON will be to generate nuclear data for use in various core simulators. Thus, the most important qualification for PARAGON is comparisons of the results of core calculations using PARAGON supplied nuclear data against plant measured data. These comparisons are provided in this section.

For PWR cores, a Westinghouse core simulator currently being used for core design and safety calculations is the Advanced Nodal Code (ANC) which was licensed by the NRC for PWR core design in 1986 (Reference 4-1). Since 1988, ANC has been using nuclear data provided by the Westinghouse transport code PHOENIX-P (Reference 4-2). The PHOENIX-P/ANC code system has been a primary nuclear design system in use at Westinghouse for PWR core analysis and has been used in the design of over 400 PWR cores.

This section will present ANC results for PWR core calculations with nuclear data supplied by PARAGON. These results will be compared to corresponding plant measurements where available and to PHOENIX-P/ANC results for the same calculations. These calculations demonstrate the accuracy of the PARAGON nuclear data when applied to a complete nuclear design code system.

Section 4-1 describes the plant cycles which were used in these comparisons. Section 4-2 will present comparisons of PARAGON/ANC calculations to plant measurements and PHOENIX-P/ANC calculations for startup physics tests. These include all rods out (ARO) hot zero power (HZP) beginning of life (BOC) critical boron concentration, ARO HZP BOC isothermal temperature coefficient (ITC) and HZP BOC control rod worths. Section 4-3 will present critical boron versus burnup comparisons of PARAGON/ANC against both measurement and PHOENIX-P/ANC results for a large number of plant cycles. Section 4-4 will present radial power (assembly power) distribution comparisons of PARAGON/ANC against measurement. Section 4-5 will present comparisons of PARAGON/ANC results against PHOENIX-P/ANC results for radial and axial power distributions for a variety of cores . Section 4-5 will also present comparisons of PARAGON/ANC results against those of PHOENIX-P/ANC for worst stuck rod, dropped rod, and rod ejection calculations for several plants.

4.1 Plant Cycles used for Comparisons

The database of plant cycles used for the PARAGON/ANC comparisons to plant measurements is listed in Table 4-1. These particular cycles were chosen based on the need to cover a large variety of plant types, lattice types, burnable absorber types, and axial blanket types. The availability of reliable plant data was also a basic consideration. The PARAGON qualification included 24 cycles and 11 plants. The plants included both Westinghouse (15 cycles) and Combustion Engineering (9 cycles) type cores. All Westinghouse core configurations were included (2 loop: 121 assemblies, 3 loop: 157 assemblies, 4 loop: 193 assemblies). CE cores in the database included 177, 217, and 241 assembly cores. For Westinghouse plants, all lattice configurations were covered (14x14, 15x15, 16x16, and 17x17). Both the 14x14 and 16x16 CE lattices were included in the database of plants. Fuel rod sizes ranged from 0.360 to 0.440 inches diameter. The enrichment range covered was from 1.30 w/o to 4.95 w/o U^{235}. One core with mixed oxide fuel was also included. The burnable absorber types covered were 1) the integral fuel burnable absorber (IFBA), 2) the wet annular burnable absorber (WABA), 3) pyrex burnable absorbers, 4) gadolinia burnable absorbers, 5) erbia burnable absorbers, and 6) fuel displacing B_4C burnable absorbers. One plant (Plant D) had multiple burnable absorbers (IFBA and WABA) in the same assembly. Axial blanket designs range from enriched annular to natural solid axial blankets (Thus bounding all Westinghouse design configurations). Some of the included cores had no axial blankets. Cycle lengths for the cycles ranged from 310 to 654 EFPD. The cores included 2 first cores and 20 reload cycles Not all cycles are used for every type of calculation in this report. A particular cycle may not be used for a certain calculation because of a lack of a complete set of data. For comparisons against PHOENIX-P/ANC calculations, a representative subset of the cores

shown in Table 4-1 was used. In all calculations, the particular cores being used for that calculation are clearly identified.

The large variety in the cycles chosen for this qualification serves two purposes: 1) it demonstrates the robustness of PARAGON and its library to analyze over a large range of cycle designs, and 2) it serves to qualify PARAGON to analyze each feature by direct comparison of results.

4.2 Startup Test Results Comparisons

Three common tests performed at PWR startups are: ARO HZP critical boron, ARO isothermal temperature coefficient, and HZP rodworth measurements. Since these measurements are taken in the just-loaded core at zero power, the complexities which come into play in analyzing a core at power with depletion including power history, feedback effects and B^{10} depletion are not present. Thus, these tests provide a good measure of the accuracy of the code system since the core conditions are well-defined and can be simulated with high reliability in the ANC code.

A comparison of HZP ARO startup critical boron results for 22 cycles is presented in Table 4-2. The table includes the measured critical boron as well as the value calculated by both PARAGON/ANC and PHOENIX-P/ANC. All calculations are within the measured to predicted difference review criteria of 50 ppm with the largest difference for PARAGON/ANC at [ ]^{a,c} and for PHOENIX-P/ANC at [ ]^{a,c} The mean measured minus predicted differences are negative for both codes meaning that both codes have a tendency to overpredict BOC HZP critical boron. The difference in the mean values is about [ ]^{a,c} with PARAGON being slightly more negative but with both codes having acceptable means. Both codes have very small standard deviations: [ ]^{a,c} for PARAGON/ANC and [ ]^{a,c} for PHOENIX-P/ANC. Over the last several years, Westinghouse has noticed a reduction in the standard deviation for the measured minus predicted BOC HZP critical boron to about [ ]^{a,c} This is directly in line with the mean value seen in Table 4-2 for PHOENIX-P/ANC. The PARAGON/ANC standard deviation value shown in Table 4-2, [ ]^{a,c}. This small standard deviation is especially good considering the wide variety of lattice types, enrichments, and burnable absorbers included in the 22 core cycles shown in the table and demonstrates the wide range of applicability for PARAGON/ANC. The performance of PARAGON/ANC for BOC HZP critical boron is thus very good.

Table 4-3 shows a comparison of startup HZP isothermal temperature coefficient results for both PARAGON/ANC and PHOENIX-P/ANC for the same 22 cycles reported in Table 4-2. The results in Table 4-3 show that there is no significant difference in the performance of the two code systems for predicting ITC. The mean for PARAGON/ANC is within [ ]^{a,c} of the mean of PHOENIX-P/ANC. [ ]^{a,c}

Rodworth comparison results for PARAGON/ANC against measurement and PHOENIX-P/ANC b met the individual rodworth criteria of 15% difference on an individual bank or 100 pcm for small worth banks. The average difference over all the rods in all nine cycles for the PARAGON/ANC code system was [ ]^{a,c} with a standard deviation of [ ]^{a,c} For the PHOENIX-P/ANC code system the corresponding values are [ ]^{a,c} and [ ]^{a,c} The average difference for total rodworth was [ ]^{a,c} for the PARAGON/ANC code system with a standard deviation of [ ]^{a,c} The corresponding values for the PHOENIX-P/ANC code system are [ ]^{a,c}

4.3 Critical Boron versus Burnup Comparisons

PARAGON/ANC predictions for at-power critical boron versus burnup are presented for 22 plant cycles in Figures 4-1 through 4-23. Measured critical boron and the PHOENIX-P/ANC predictions are also presented in these figures. Examining the figures, the following conclusions can be made:

1-1 Both PARAGON/ANC and PHOENIX-P/ANC generally predict the shape of the boron letdown curve and the end of cycle well. PARGON/ANC does slightly better in [

]^{a,c}.

1-2 Most cycles present clear evidence of significant B^{10} depletion. B^{10} isotopic information was not available for most of the cycles used in this analysis. Therefore, depletion was not included in any of the predictions or measured values. B^{10} depletion is characterized by the measured to predicted critical boron difference becoming larger throughout the middle of the cycle, then becoming smaller at end of cycle when the boron concentration is low and the B^{10} depletion is no longer important. B^{10} depletion has become a significant effect in boron letdown curves since, over the last several years, plants are operating with very few shutdowns and B^{10} depletion effects can be larger than [ ]^{a,c} The effect of B^{10} depletion, unless accurately accounted for, makes statistical analysis of the measured to predicted critical boron differences yield an inaccurate measure of how well a code system predicts reactivity. In all cases except [ ]^{a,c}, the measured critical boron values are larger than the predicted critical boron values, accounting for B^{10} depletion thus making the measured to predicted differences smaller. This is because, if B^{10} depletion is accounted for in the prediction, the predicted values will get larger since they are currently based on a larger B^{10} concentration than is actually in the core. If the measured values are adjusted, they will get smaller since they inherently include a smaller isotopic percentage of B^{10}. Either way of accounting for B^{10} depletion will improve the mid-cycle measured to predicted critical boron differences [

]^{a,c}

1-3 An interesting case is presented in Figure 4-7. This cycle had several very long shutdowns and took about 3 years to complete. [

]^{a,c}

1-4 Figure 4-10, which presents the results for a 121 assembly core with MOX fuel, shows the [

]^{a,c} The B^{10} depletion effect is small for this cycle.

1-5 Figure 4-20 shows the results for a first core. [

]^{a,c}

4.4 Radial Power Distributions

In addition to reactivity, a nuclear code system must be able to calculate core power distributions accurately. To provide this evidence for the PARAGON/ANC system, assembly power comparisons were made for five plants For these plants, measured assembly power values based on core flux maps were compared to predicted assembly powers from PARAGON/ANC at the same conditions. Maps from five plants were used in this analysis. These plants are:

Plant	Lattice	Fuel	Assemblies in core	Cycles
A	17x17	UO_2	157	10, 11
B	16x16	UO_2	121	17,18
C	14x14	UO_2	121	25, 26
D	15x15	UO_2	193	10, 11
J	17x17	UO_2	193	10,11

The measured to predicted comparisons for these maps are presented in Figures 4-24 through 4-51. For each cycle, two or three maps are presented at different burnups during the cycle. The cycle burnups range for the maps is from [

]^{a,c} The average difference between the measured and predicted normalized powers is shown in each figure as well as the standard deviation of these differences The measured to predicted average difference over all twenty-eight maps is [ ]^{a,c} and the average standard deviation of the differences over all the maps is [ ]^{a,c} These very small values show that PARAGON/ANC predicts assembly power with high accuracy over a wide range of different lattice types and over the large burnup range seen in plant cycles.

4.5 PARAGON/ANC versus PHOENIX-P/ANC Comparisons

As described earlier in this report, the PHOENIX-P/ANC nuclear code system has been licensed by the NRC since 1988 and has had extensive use in PWR safety and design calculations. Therefore, as part of the qualification of PARAGON, comparisons have been made between the results of core calculations with the two systems to demonstrate that PARAGON/ANC predictions for operating PWR cores are essentially of the same quality, or better, as those of PHOENIX-P/ANC and therefore any [ ]^{a,c}used for the PHOENIX-P/ANC system will be applicable to the PARAGON/ANC code system. Reactivity comparisons between the two code systems have been shown in the HZP ARO critical boron results presented in section 4-2 and in the at-power critical boron versus burnup results presented in section 4-3. Comparisons for rodworths between the two code systems were also made in section 4-2. In this section, comparisons are made between radial and axial power distributions calculated by both code systems for several different plants with different lattices and core sizes. In addition, the results of calculations for core conditions which are [

]^{a,c}

Figures 4-52 through 4-78 show comparisons of radial power and burnup distributions calculated with both PARAGON/ANC and PHOENIX-P/ANC. The cycles shown are listed in the table below:

Plant	Lattice	Fuel	Assemblies in core	Cycles
A	17x17	UO_2	157	10, 11
C	14x14	UO_2	121	25, 26
D	15x15	UO_2	193	10, 11
E	14x14	MOX	121	25
F	16x16 CE	UO_2	217	11, 12

For each cycle, comparisons between the normalized assembly powers from both code systems are shown at BOC and EOC. In addition, the radial assembly burnups predicted at EOC from both code systems are compared. As can be seen by examining these figures, the differences between the PARAGON/ANC predictions and those of PHOENIX-P/ANC for both power and burnup are very small.

Figures 4-79 to 4-102 show comparisons of axial power predictions from PARAGON/ANC versus those from PHOENIX-P ANC for four plants listed in the table below:

Plant	Lattice	Fuel	Assemblies in core	Cycles
A	17x17	UO_2	157	10, 11
C	14x14	UO_2	121	25, 26
F	16x16 CE	UO_2	217	11, 12
G	14x14 CE	UO_2	217	13, 14

Plants A and C are Westinghouse type plants with axial blankets. Plants F and G are Combustion Engineering type plants with no axial blankets. Axial power comparisons are made for three times in life for each cycle: BOC, MOC (i.e., middle of cycle), and EOC. As can be seen by examining each of these figures, the axial power shapes predicted by the two code systems are virtually identical.

Table 4-13 presents the results from worst stuck rod calculations for the following four plants:

Plant	Lattice	Fuel	Assemblies in core	Cycles
A	17x17	UO_2	157	11
B	16x16	UO_2	121	17
C	14x14	UO_2	121	24
D	15x15	UO_2	193	10

These calculations were performed in full core geometry at BOC HZP conditions with all the rods completely inserted (ARI) except the highest worth rod (called the worst stuck rod or WSR) which was completely withdrawn from the core. The parameters of interest for this calculation are the worth of the worst stuck rod, and the total peaking factor Fq, the radial peaking factor $F\Delta h$, and the axial peaking factor Fz. The worth of the worst stuck rod is determined by performing a calculation at the same conditions except all the rods are inserted. The difference between the ARI and ARI-WSR eigenvalues is the worth of the WSR. Table 4-13 summarizes the results of the ARI-WSR calculation for the four plants for both code systems. As can be seen from the table, the PARAGON/ANC results are within [ ]^{a,c} for the worth of the WSR. The peaking factors are also similar with the largest difference being [ ]^{a,c} [ ]^{a,c} in Plant C.

Table 4-14 presents the results from BOC dropped rod calculations for the same four plants performed with PARAGON/ANC and PHOENIX-P/ANC. The table presents the rodworth, the total peaking factor Fq, the radial peaking factor FΔh, and the axial peaking factor Fz for the dropped rod calculation from each code system As seen in the table, the dropped rod worths for the two code systems are within [ ]^{a,c} and the peaking factors differences are also very small, the largest being [ ]^{a,c} for Fq of Plant D.

Table 4-15 presents the results from rod ejection calculations performed with both code systems for the same four plants. Four rod ejection calculations were performed for each plant: BOC HFP, BOC HZP, EOC HFP, and EOC HZP. Rod ejection calculations are similar to stuck rod calculations except that feedback is frozen at the pre-ejection conditions because of the speed of the event. This leads to much larger rod worths and peaking factors. Comparing the rod ejection cases, the differences in rodwoth between the calculations from the two code systems show that the largest difference in rod worth is [ ]^{a,c} The differences in peaking factors between the PARAGON/ANC cases and the PHOENIX-P/ANC cases are also within expected differences considering the large peaking factor values for ejected rod cases.

Table 4-16 presents results for hot full power, end of cycle moderator temperature coefficient calculations performed in both PHOENIX-P/ANC and PARAGON/ANC These calculations were performed at [ ]^{a,c} with all rods withdrawn. These calculations demonstrate that the PARAGON-based model calculates EOC HFP MTC values within [ ]^{a,c} of the PHOENIX-P model.

The results presented in this section demonstrate that PARAGON-based models compare well to measurements and to PHOENIX-P model results. The good agreement between PHOENIX-P models and PARAGON models has been shown for startup measurement parameters such as HZP boron, HZP ITC, and HZP rodworths and for full power critical boron letdown predictions. This good agreement has also been demonstrated for off normal calculations such as ARI –WSR, dropped rod, and ejected rod calculations. EOC HFP MTC predictions are also very similar between PARAGON-based models and PHOENIX-P-based models. The calculations documented in this section demonstrate that PARAGON can be used as a replacement for PHOENIX-P without changing any licensing bases currently in place for PHOENIX-P based models.

Table 4-1: Plant and Cycle Descriptions

a, b, c

Table 4-1 (cont'd): Plant and Cycle Descriptions

[a, b, c]

Table 4-1 (cont'd): Plant and Cycle Descriptions

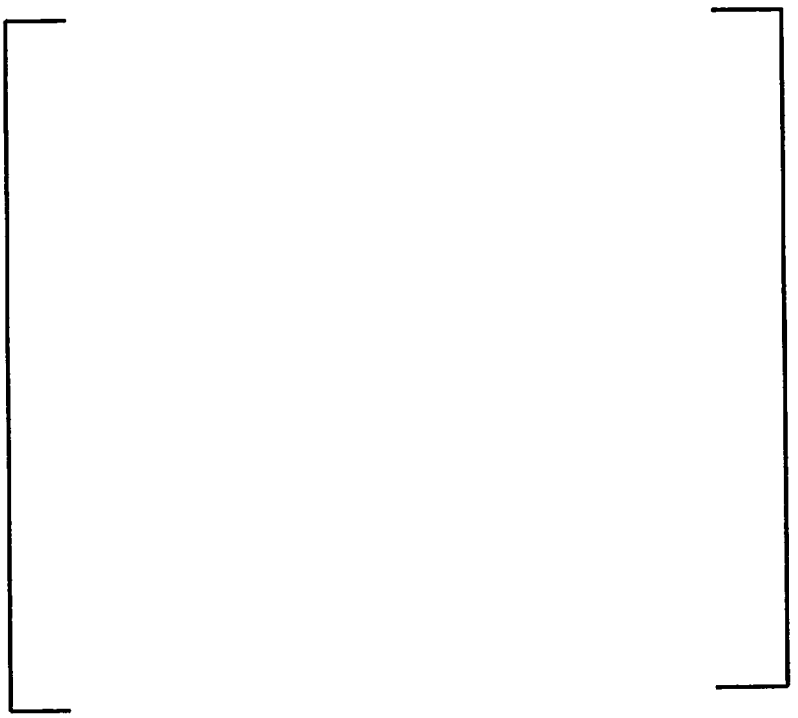

a, b, c

Table 4-2: Hot Zero Power All Rods Out Critical Boron

a, b, c

Table 4-3: Hot Zero Power All Rods Out Isothermal Temperature Coefficients

a, b, c

Table 4-4: Hot Zero Power Contol Bank Worth: Plant A, Cycle 11

a, b, c

[ ]

Table 4-5: Hot Zero Power Contol Bank Worth: Plant B, Cycle 17

a, b, c

[ ]

Table 4-6: Hot Zero Power Contol Bank Worth: Plant C, Cycle 24

a, b, c

[

]

Table 4-7: Hot Zero Power Contol Bank Worth: Plant D, Cycle 10

a, b, c

[

]

Table 4-8: Hot Zero Power Control Bank Worth: Plant E, Cycle 24

a, b, c

Table 4-9: Hot Zero Power Contol Bank Worth: Plant I, Cycle 13

a, b, c

Table 4-10: Hot Zero Power Contol Bank Worth: Plant I, Cycle 14

a, b, c

Table 4-11: Hot Zero Power Contol Bank Worth: Plant J, Cycle 10

a, b, c

[ ]

Table 4-12: Hot Zero Power Contol Bank Worth: Plant J, Cycle 11

a, b, c

[ ]

Table 4-13: ARI-WSR Control Rod Worth Comparison:

a, b, c

[

]

Table 4-14: Dropped Rod Worth Comparison

a, b, c

Table 4-15: Rod Ejection Comparison

a, b, c

Table 4-16: End of Life HFP Moderator Temperature Coefficient

a, b, c

[

]

Figure 4-1: Crtical Boron Concentration Versus Cycle Burnup Comparisons: Plant A Cycle 10

[a, b, c]

Figure 4-2: Critical Boron Concentration Versus Cycle Burnup Comparisons: Plant A Cycle 11

[a, b, c

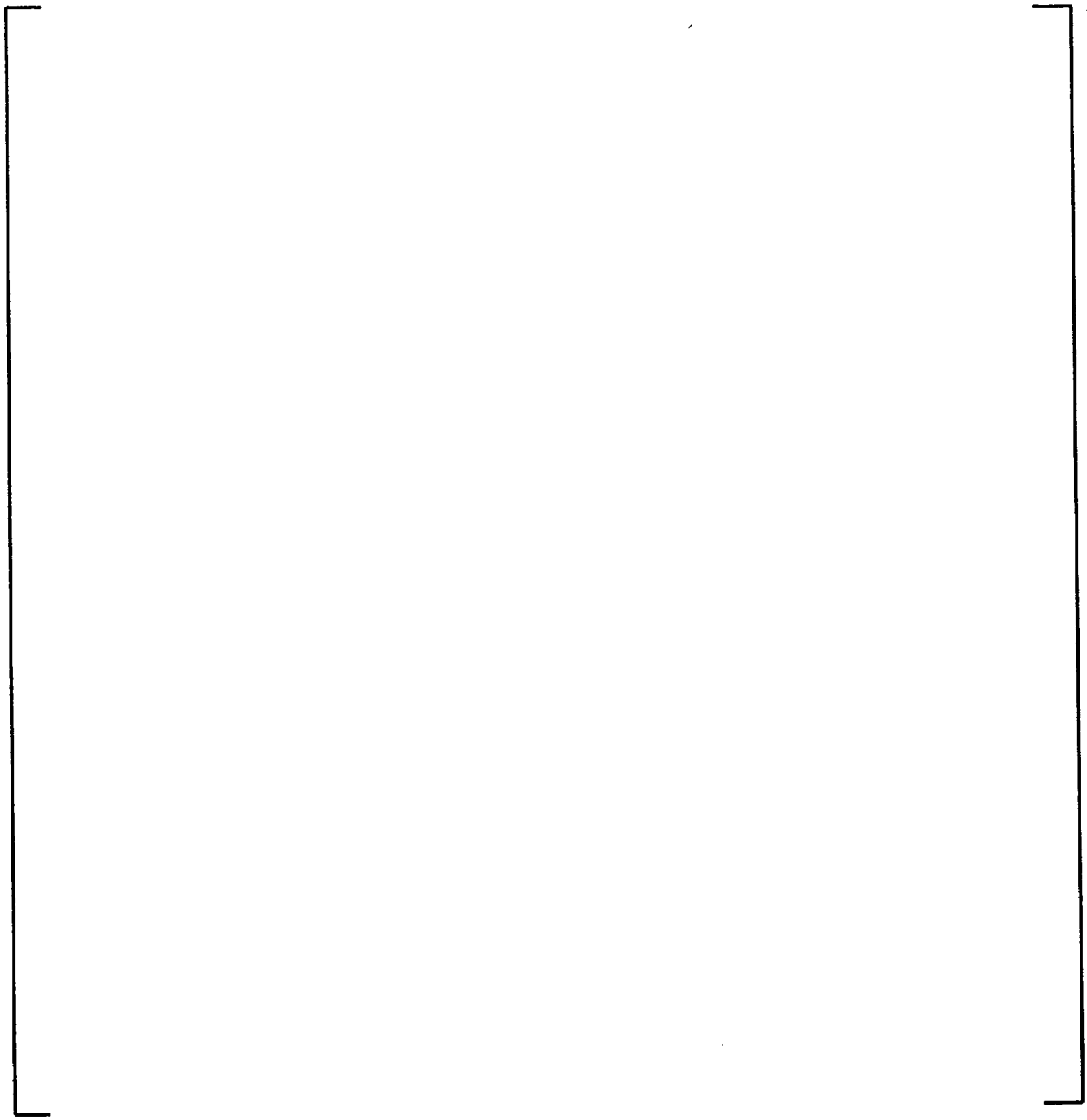

]

Figure 4-3: Crtical Boron Concentration Versus Cycle Burnup Comparisons: Plant B Cycle 17

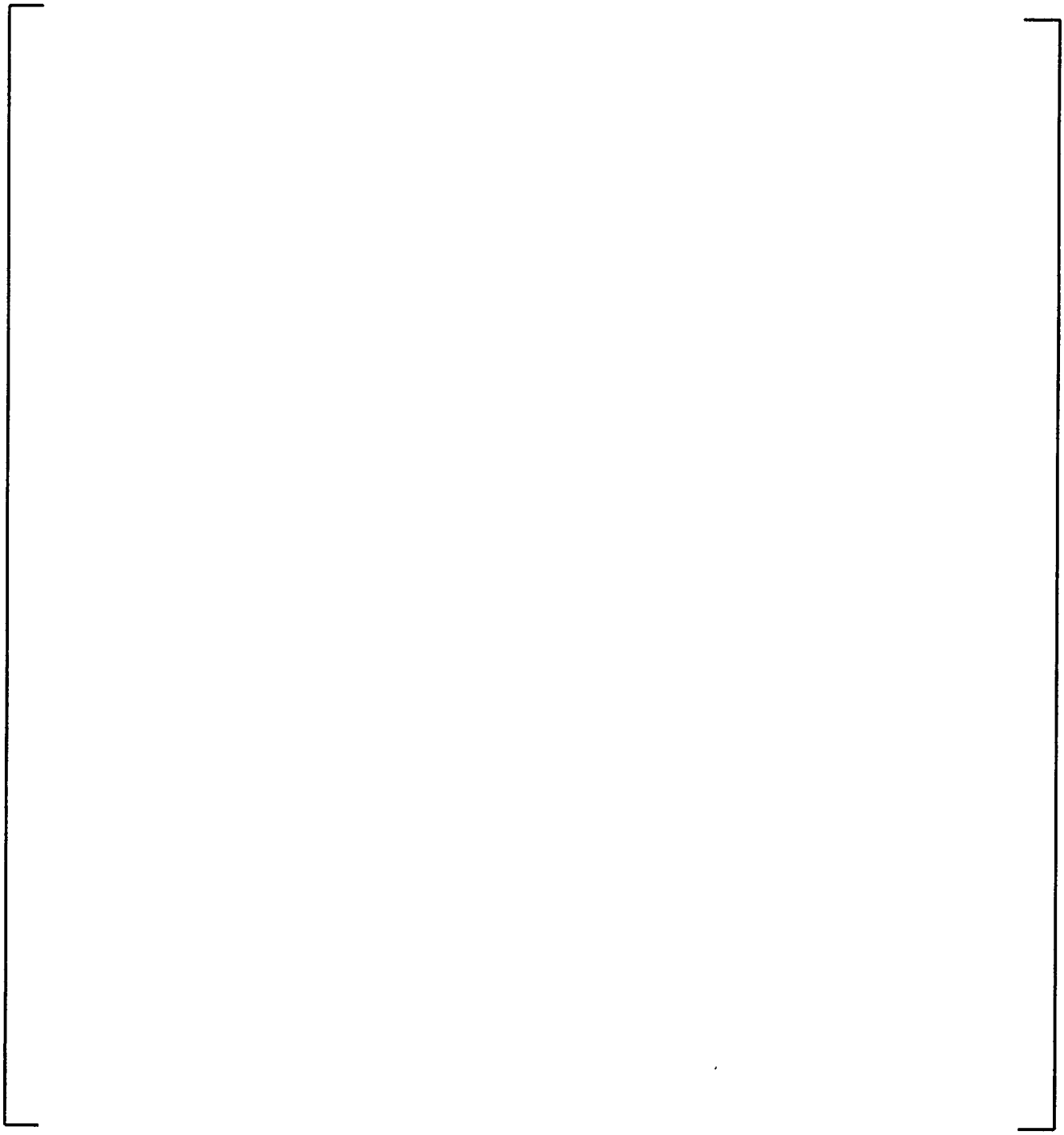

a, b, c

Figure 4-4: Crtical Boron Concentration Versus Cycle Burnup Comparisons: Plant B Cycle 18

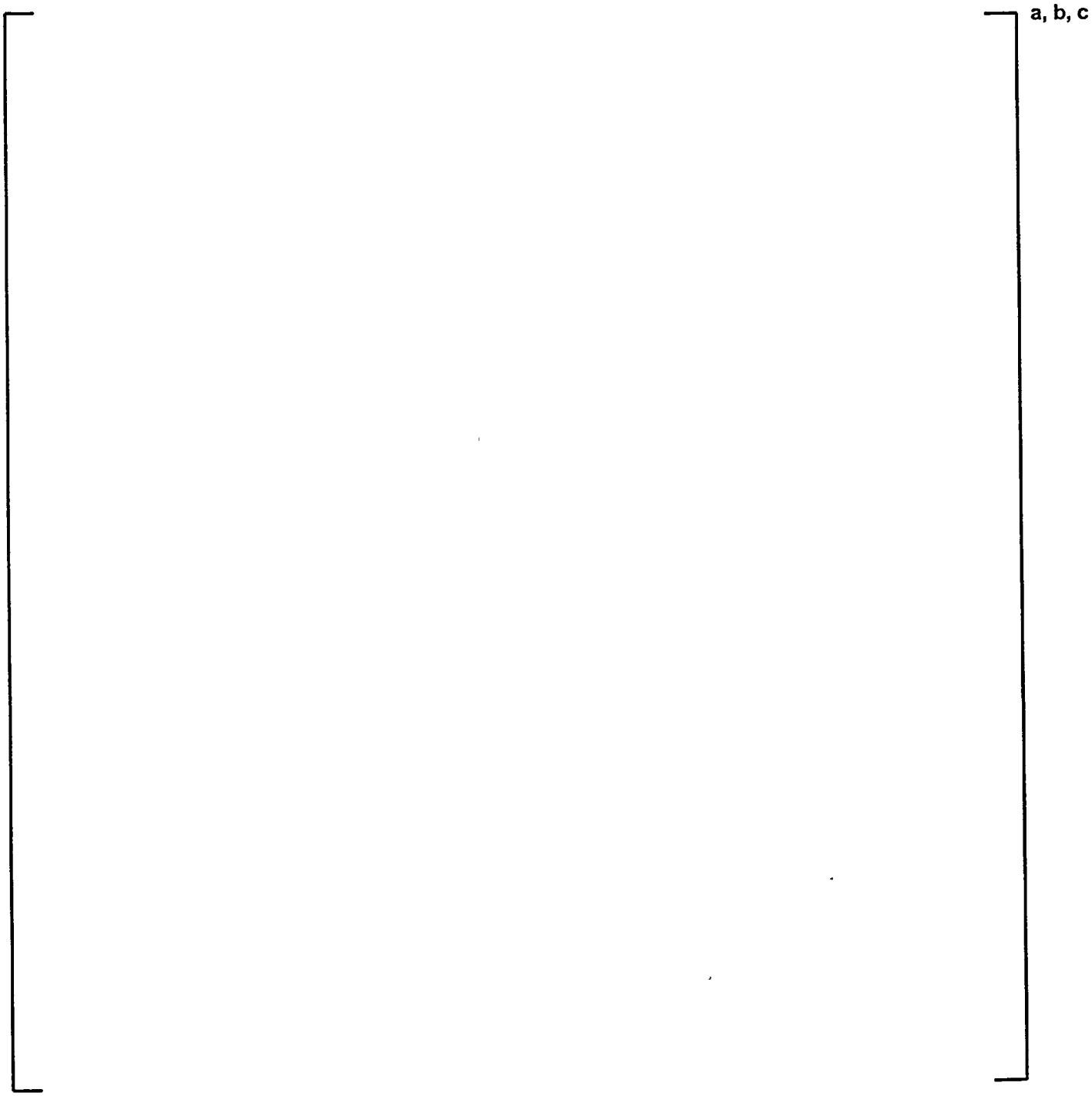

a, b, c

Figure 4-5: Critical Boron Concentration Versus Cycle Burnup Comparisons: Plant C Cycle 25

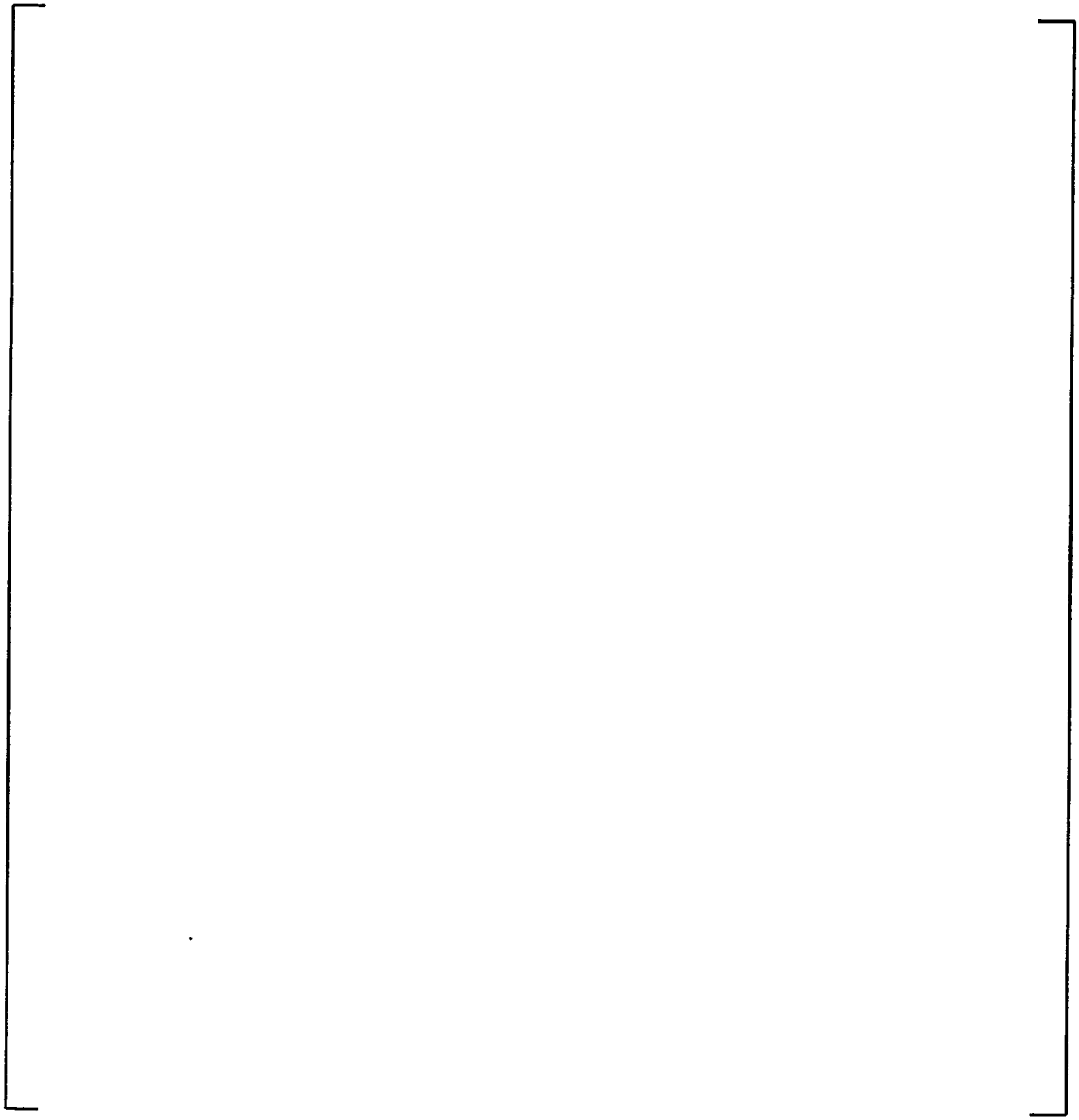

a, b, c

Figure 4-6: Critical Boron Concentration Versus Cycle Burnup Comparisons: Plant C Cycle 26

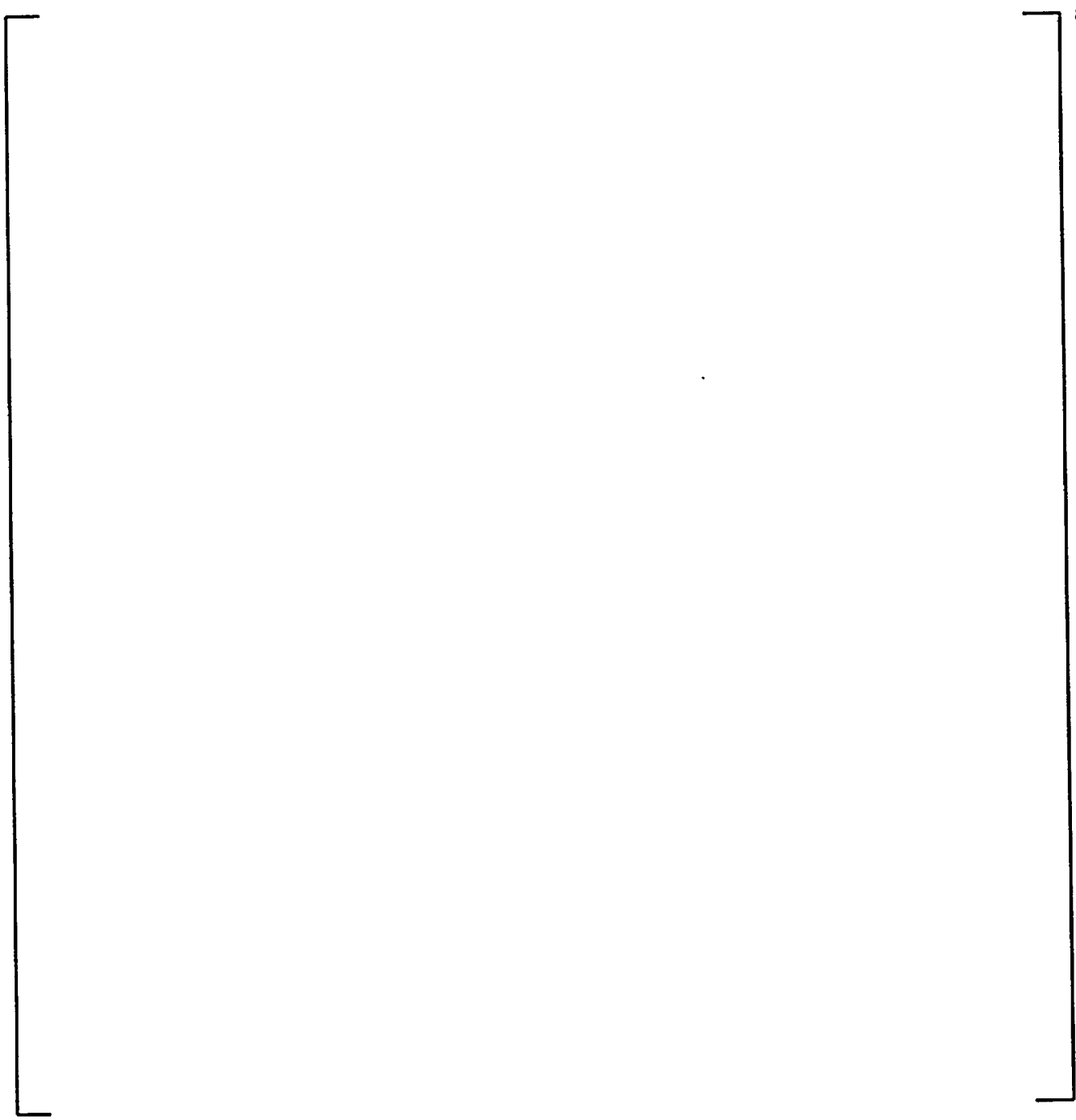

a, b, c

Figure 4-7: Critical Boron Concentration Versus Cycle Burnup Comparisons: Plant D Cycle 9

a, b, c

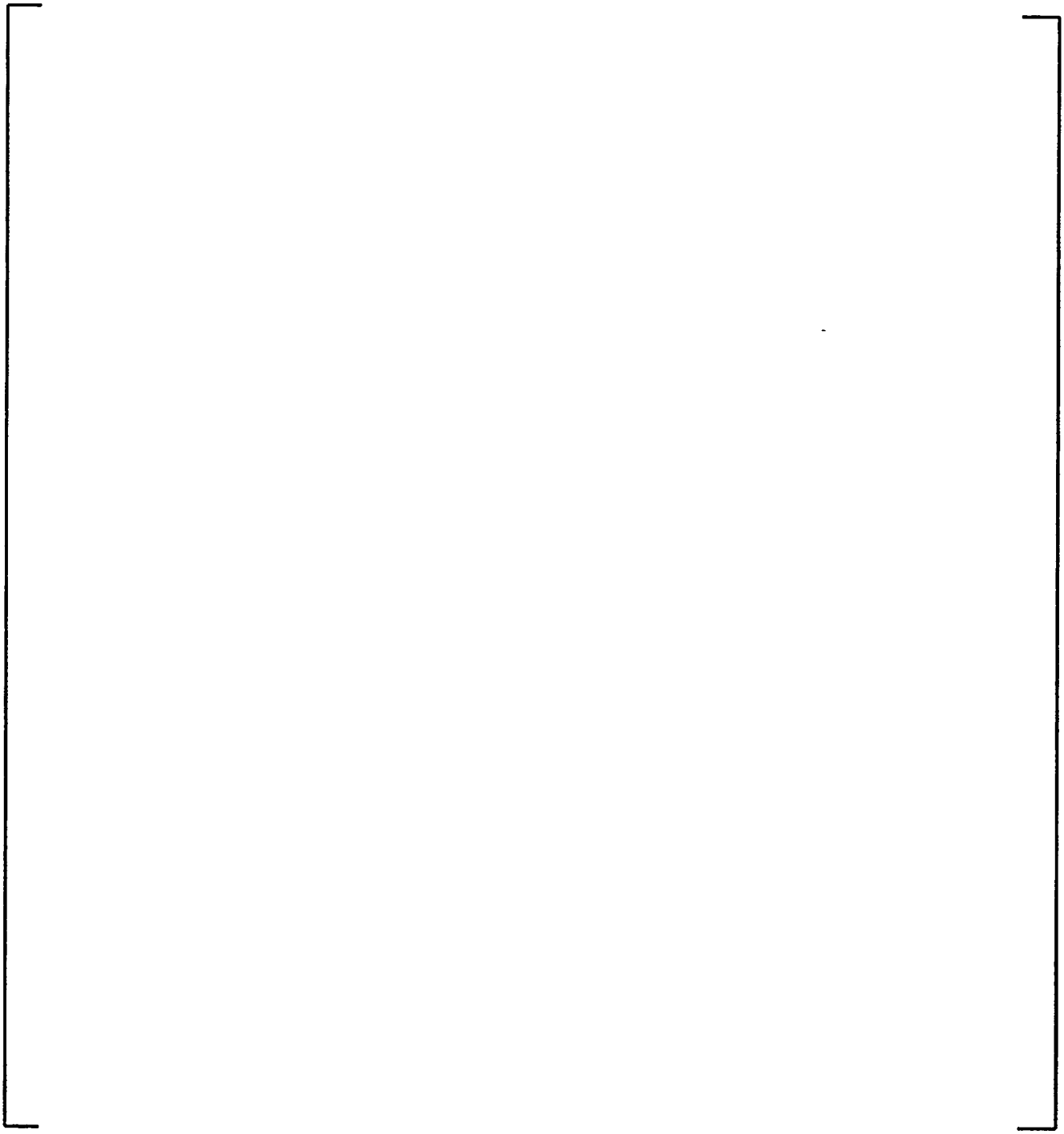

Figure 4-8: Critical Boron Concentration Versus Cycle Burnup Comparisons: Plant D Cycle 10

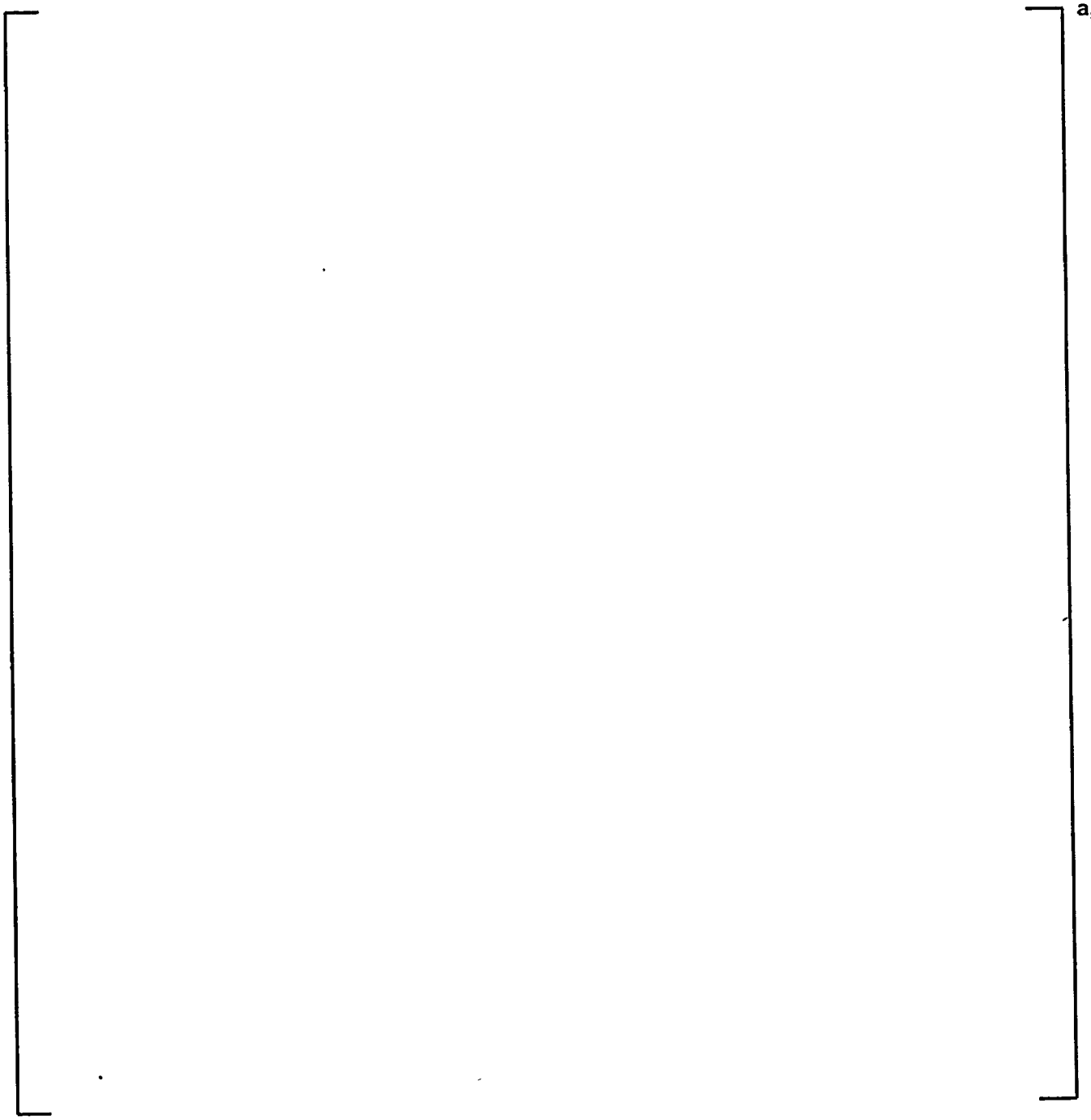

a, b, c

Figure 4-9: Critical Boron Concentration Versus Cycle Burnup Comparisons: Plant D Cycle 11

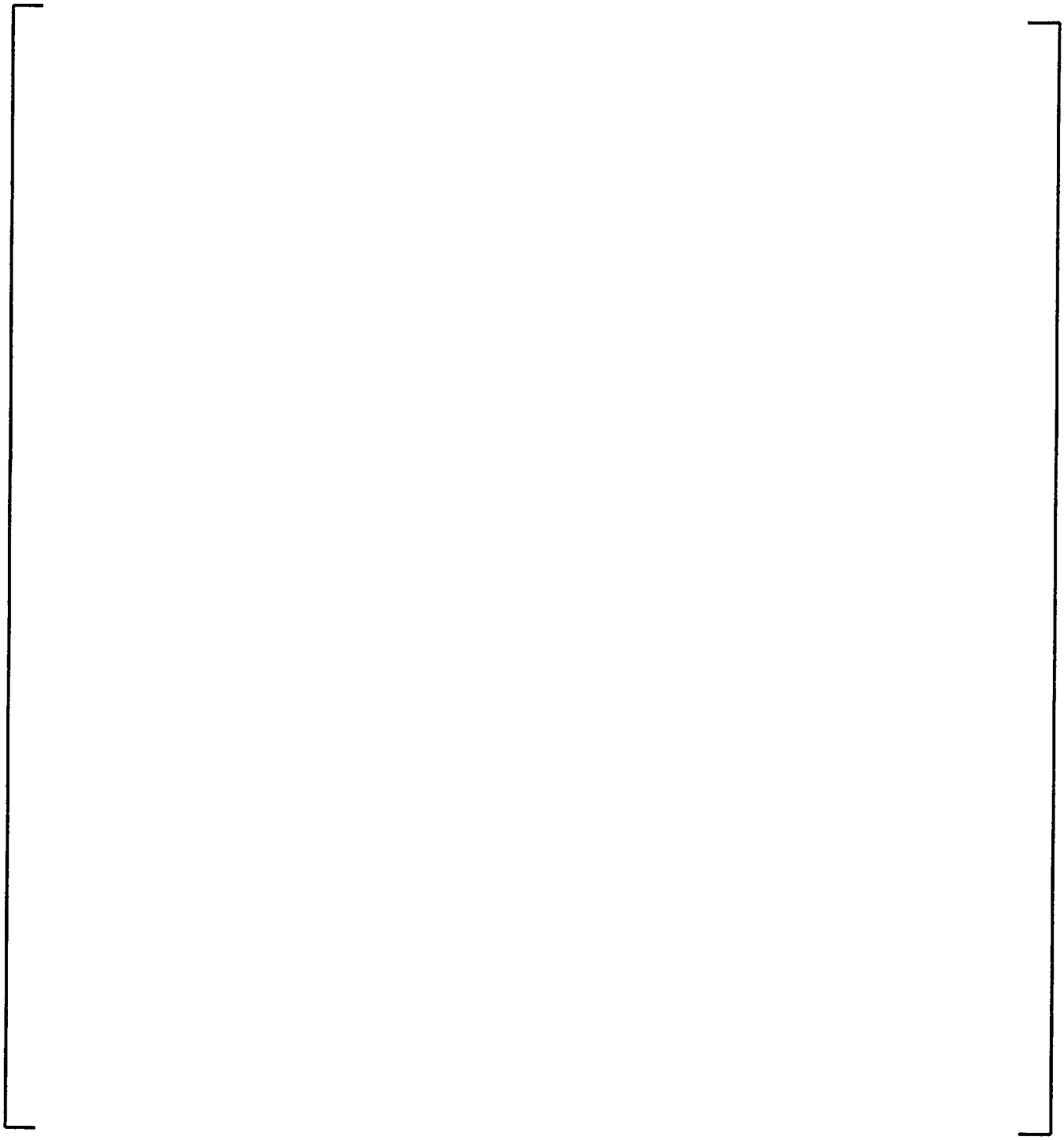

Figure 4-10: Critical Boron Concentration Versus Cycle Burnup Comparisons: Plant E Cycle 25

[a, b, c]

Figure 4-11: Critical Boron Concentration Versus Cycle Burnup Comparisons: Plant F Cycle 10

a, b, c

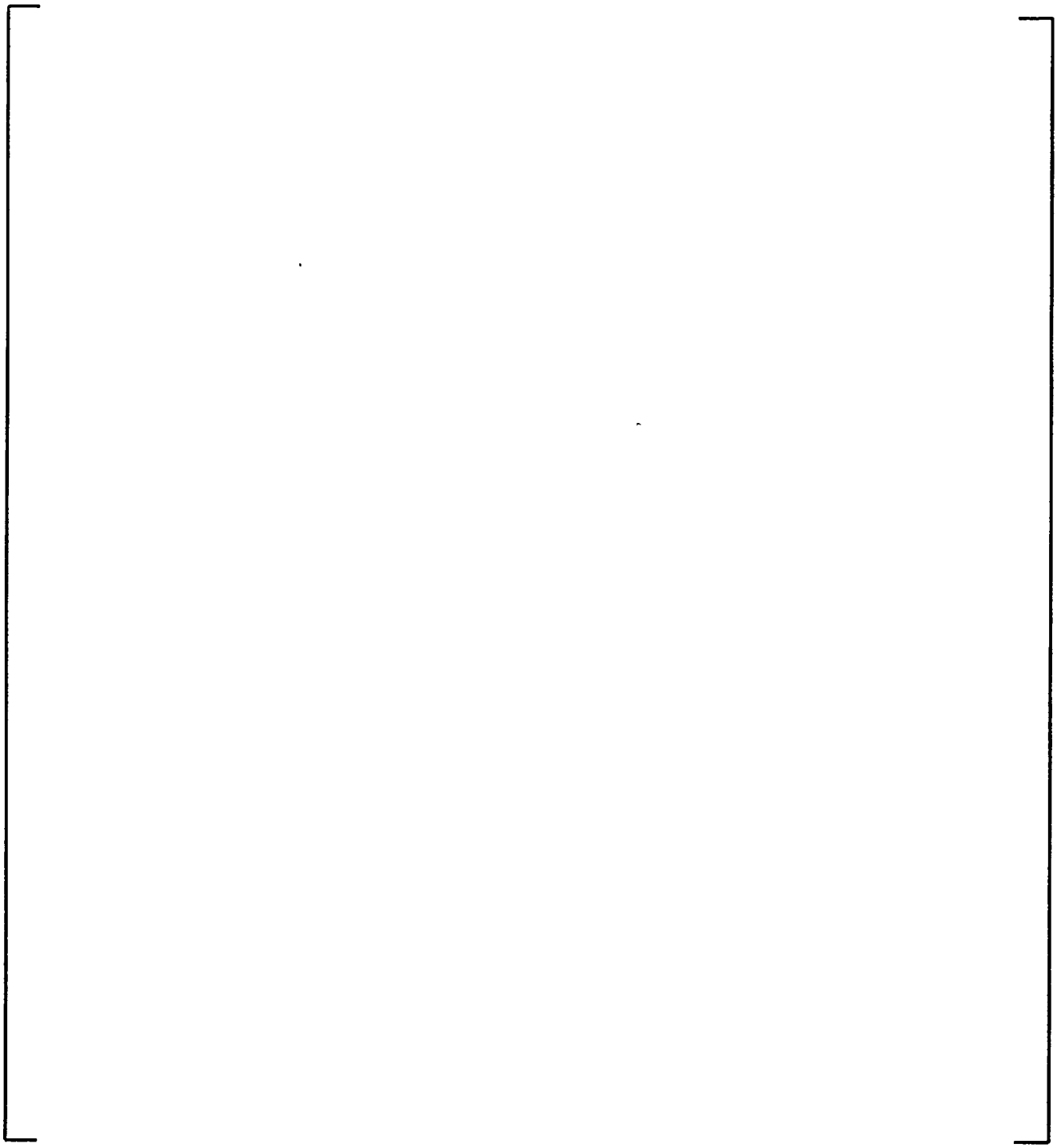

Figure 4-12: Critical Boron Concentration Versus Cycle Burnup Comparisons: Plant F Cycle 11

a, b, c

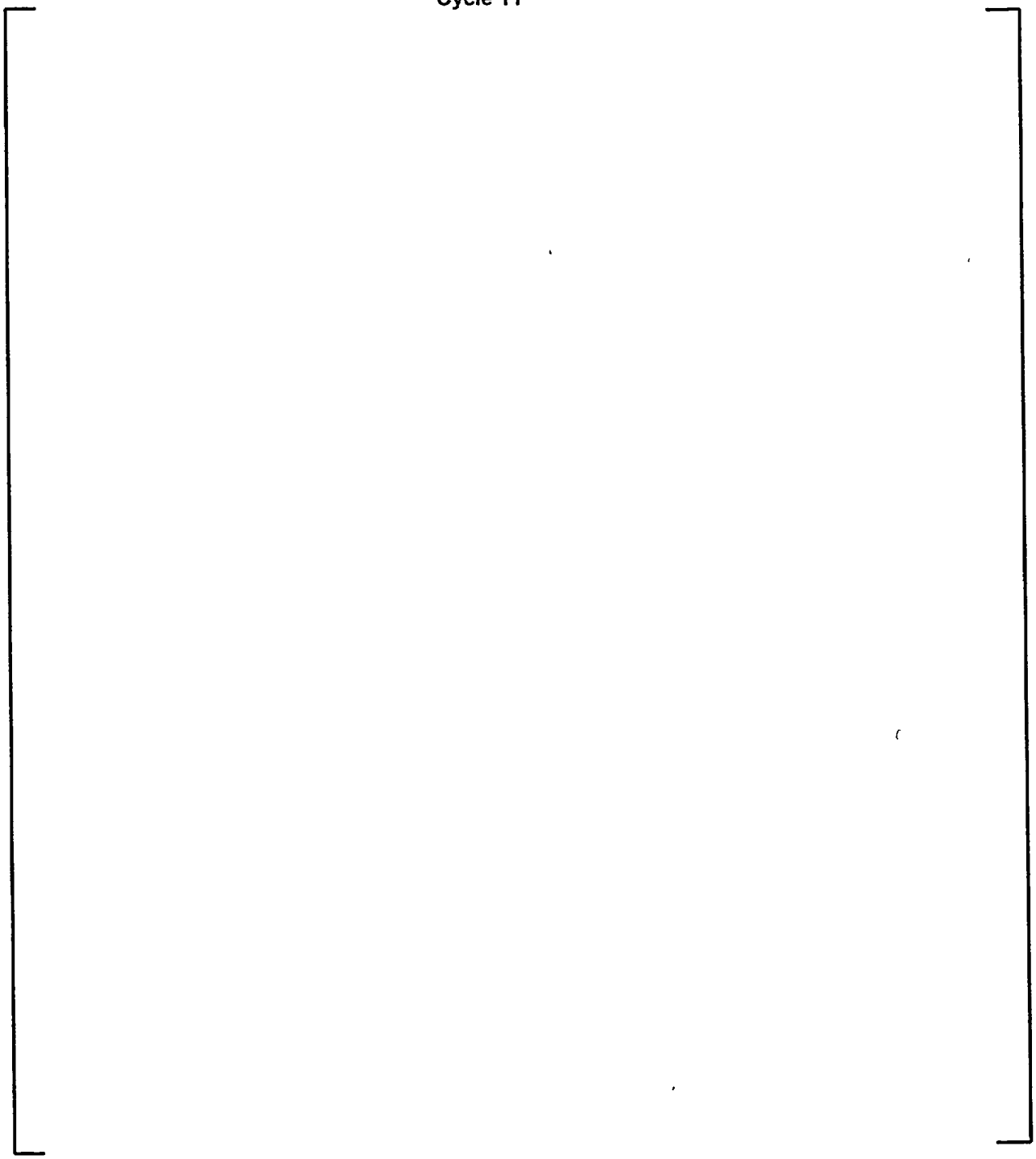

Figure 4-13: Critical Boron Concentration Versus Cycle Burnup Comparisons: Plant F Cycle 12

a, b, c

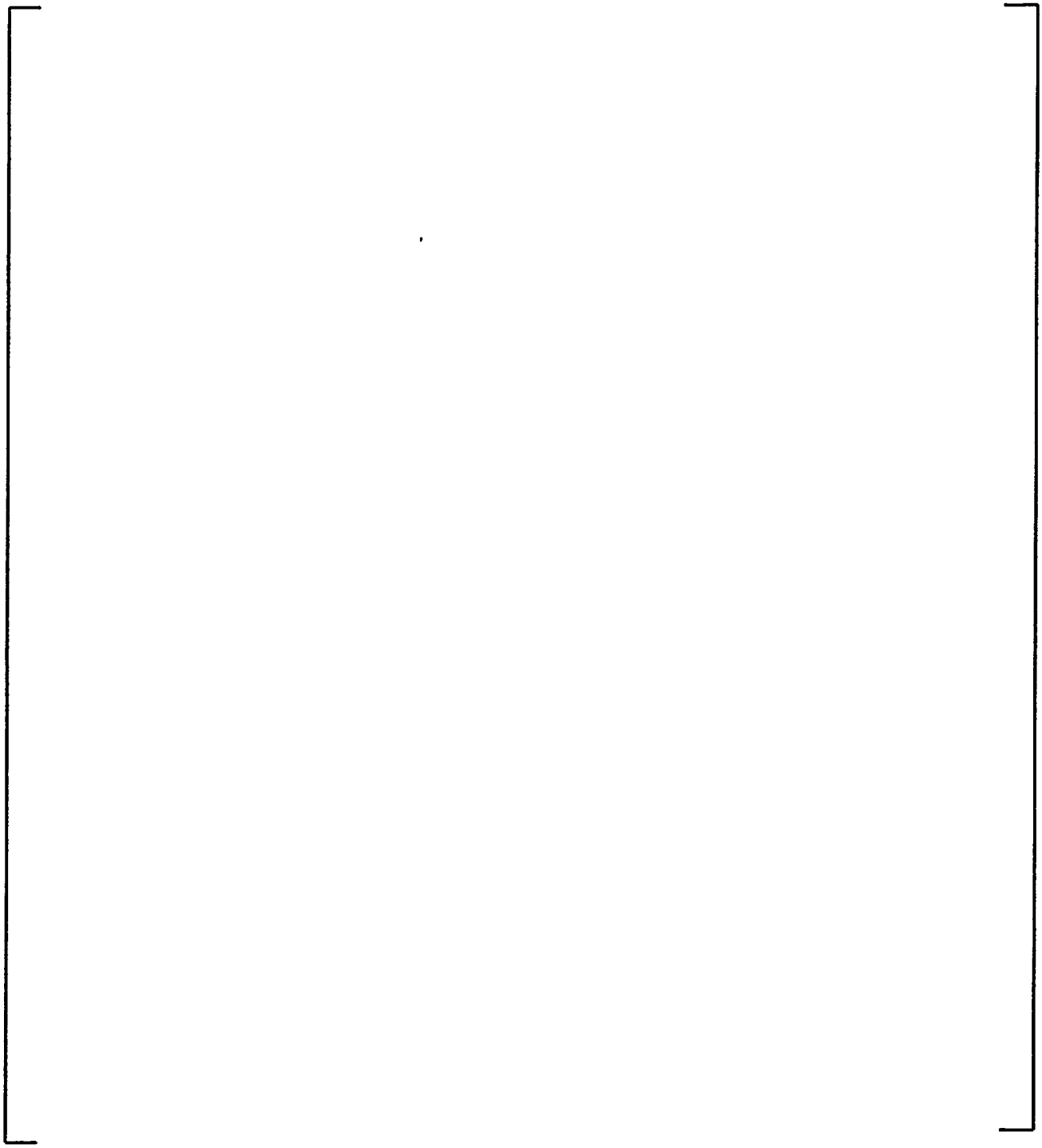

Figure 4-14: Critical Boron Concentration Versus Cycle Burnup Comparisons: Plant G Cycle 13

a, b, c

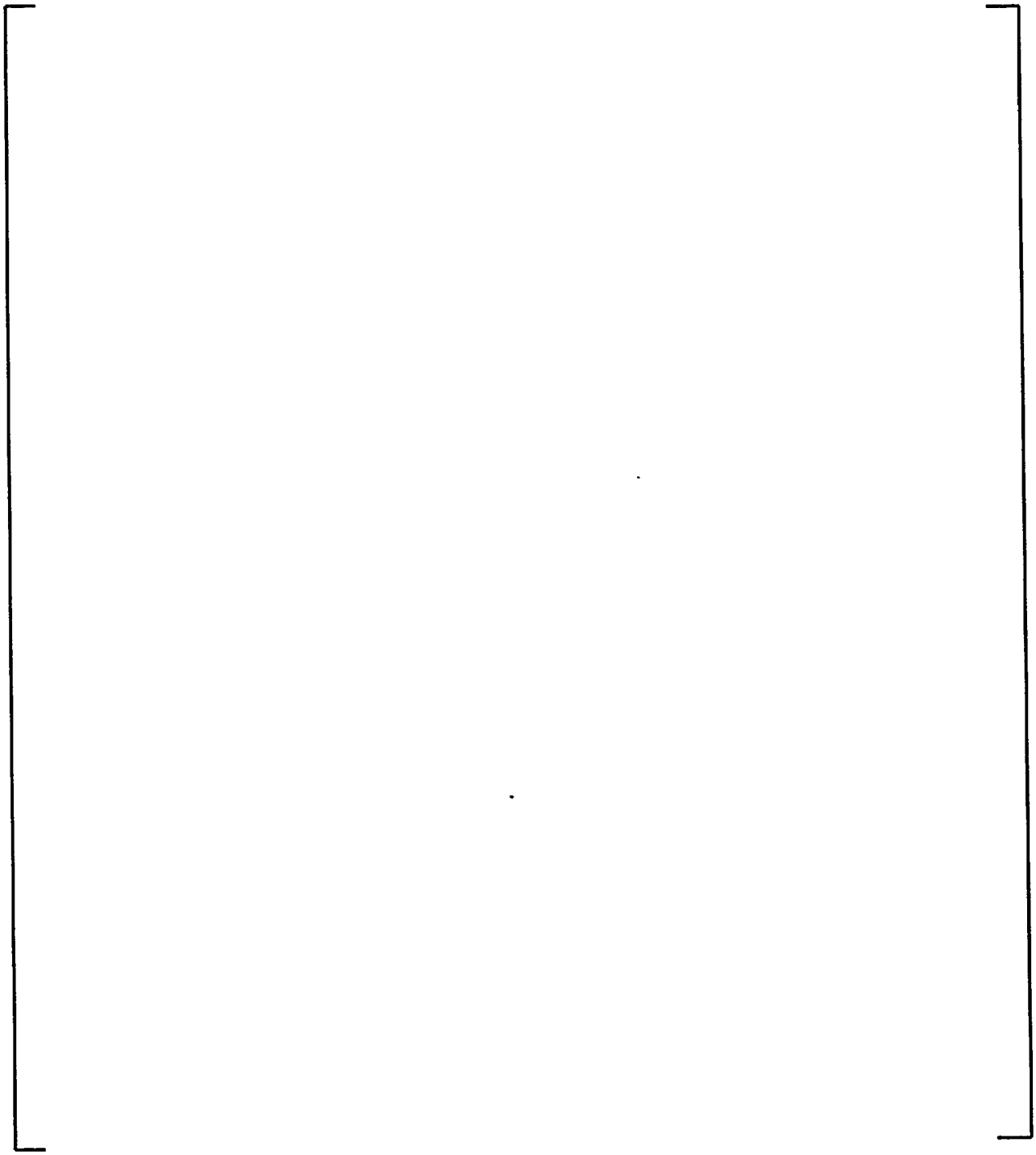

Figure 4-15: Critical Boron Concentration Versus Cycle Burnup Comparisons: Plant H Cycle 1

a, b, c

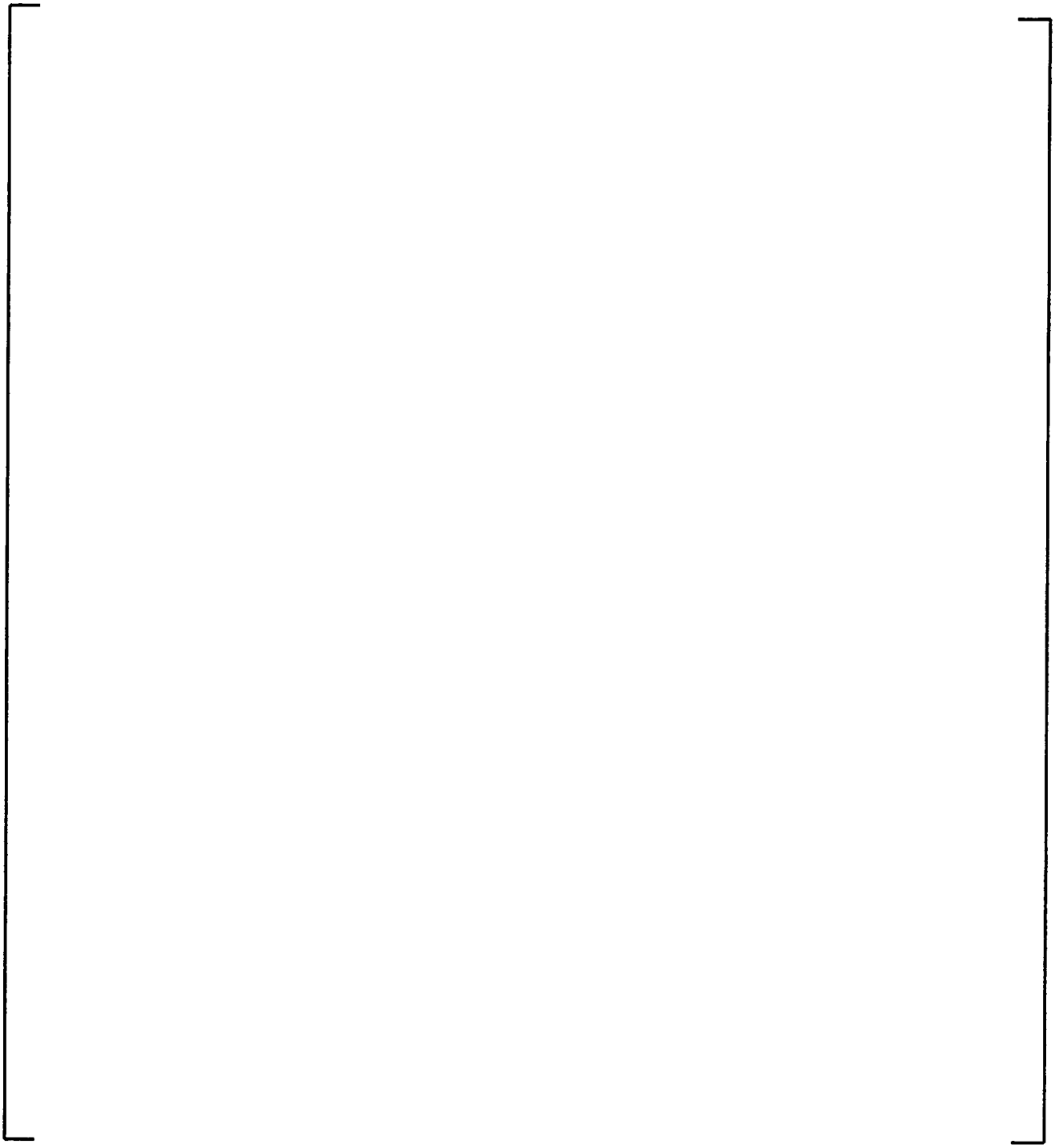

Figure 4-16: Critical Boron Concentration Versus Cycle Burnup Comparisons: Plant I Cycle 13

[a, b, c

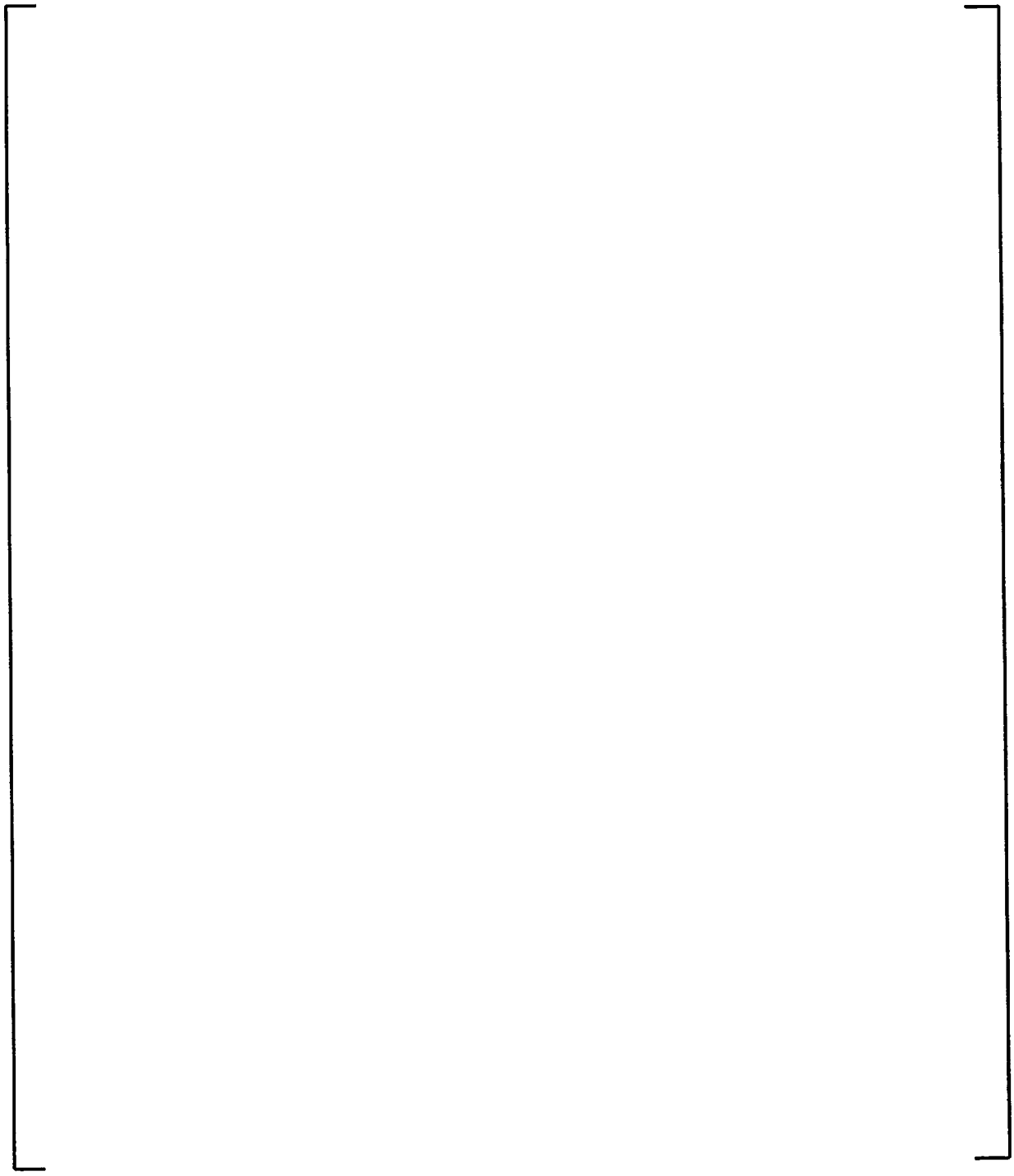

]

Figure 4-17: Critical Boron Concentration Versus Cycle Burnup Comparisons: Plant I Cycle 14

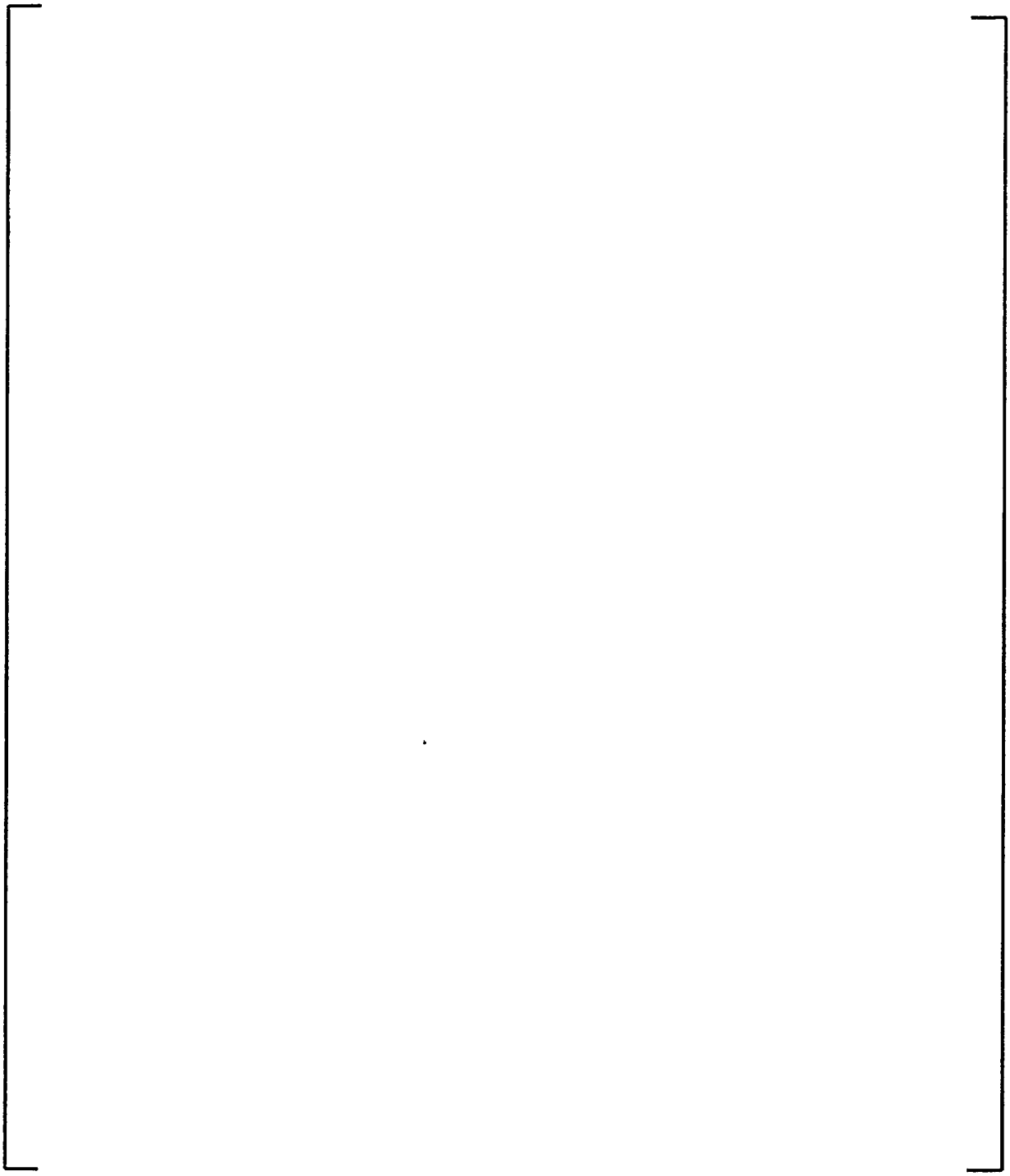

a, b, c

Figure 4-18: Critical Boron Concentration Versus Cycle Burnup Comparisons: Plant J Cycle 10

a, b, c

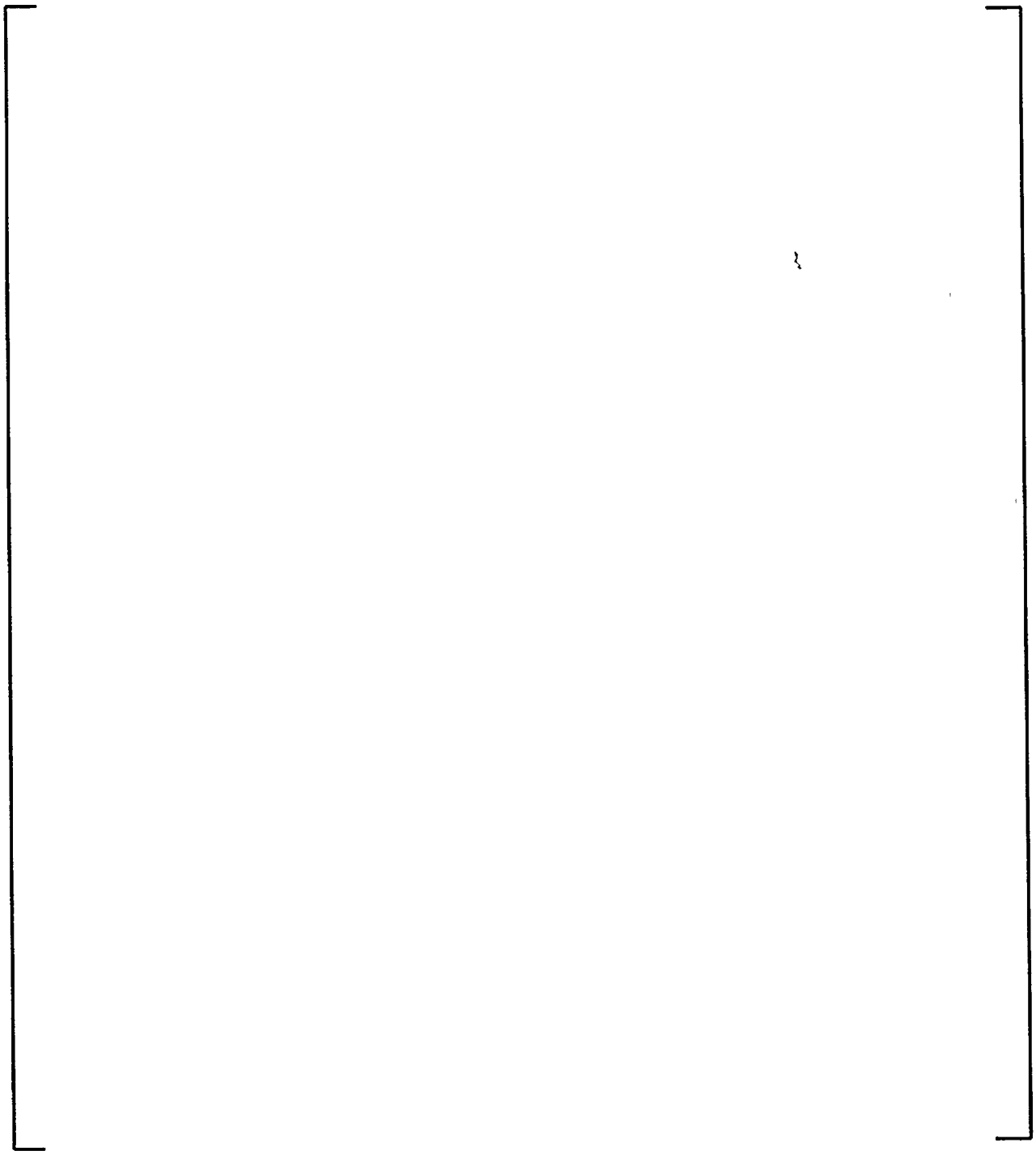

Figure 4-19: Critical Boron Concentration Versus Cycle Burnup Comparisons: Plant J Cycle 11

a, b, c

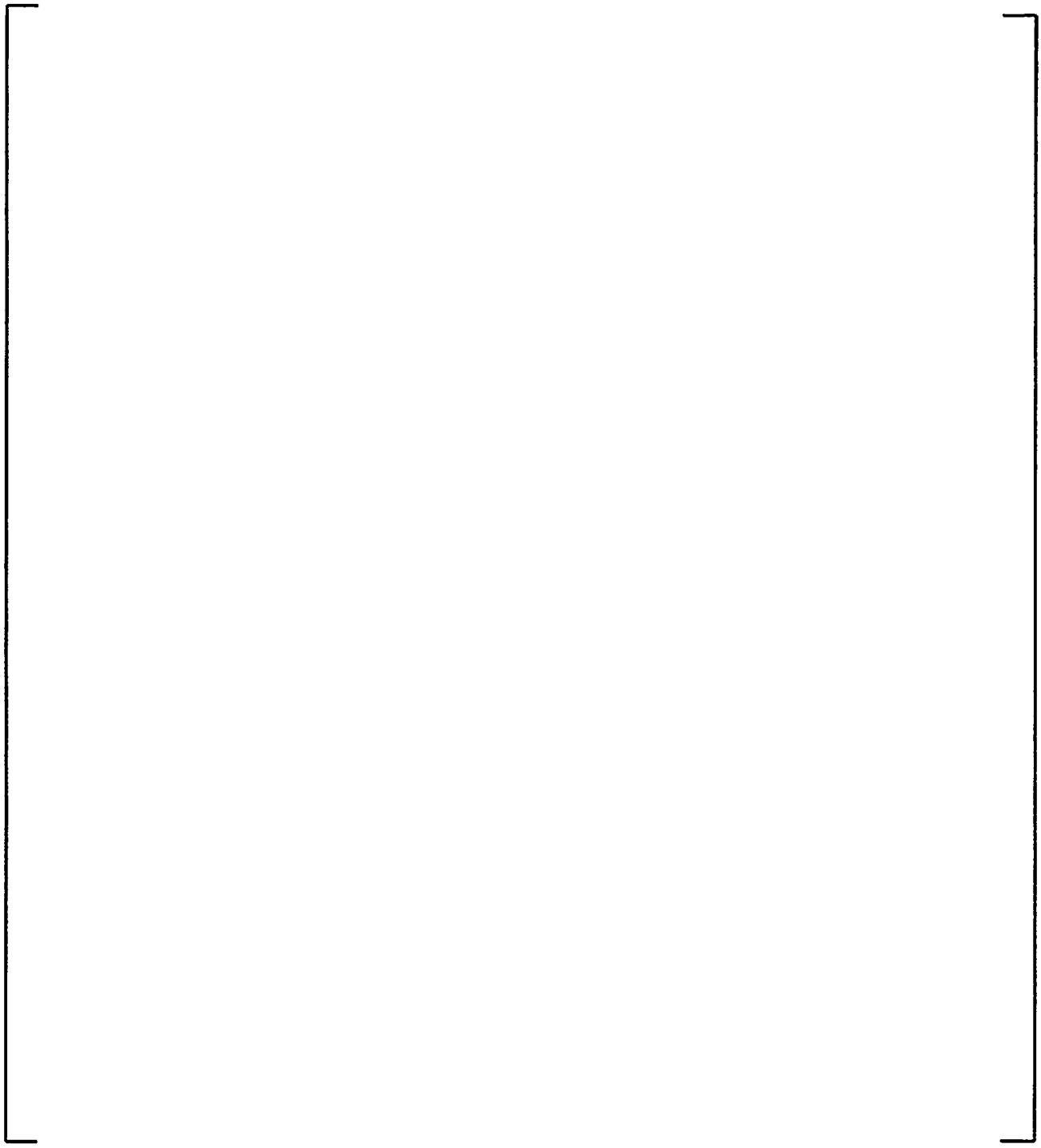

Figure 4-20: Critical Boron Concentration Versus Cycle Burnup Comparisons: Plant K Cycle 1

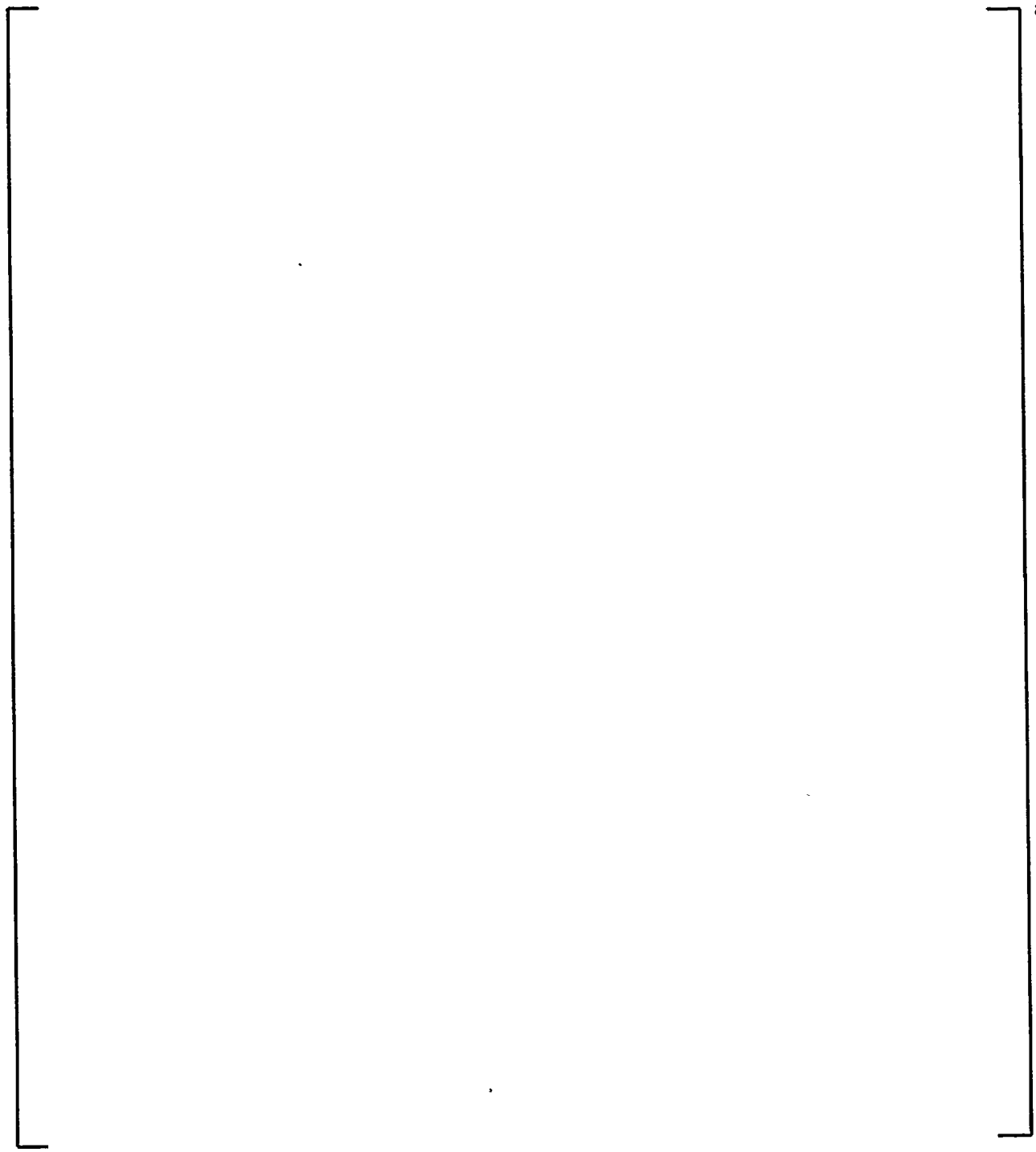

a, b, c

Figure 4-21: Critical Boron Concentration Versus Cycle Burnup Comparisons: Plant K Cycle 2

[a, b, c]

Figure 4-22: Critical Boron Concentration Versus Cycle Burnup Comparisons: Plant K Cycle 3

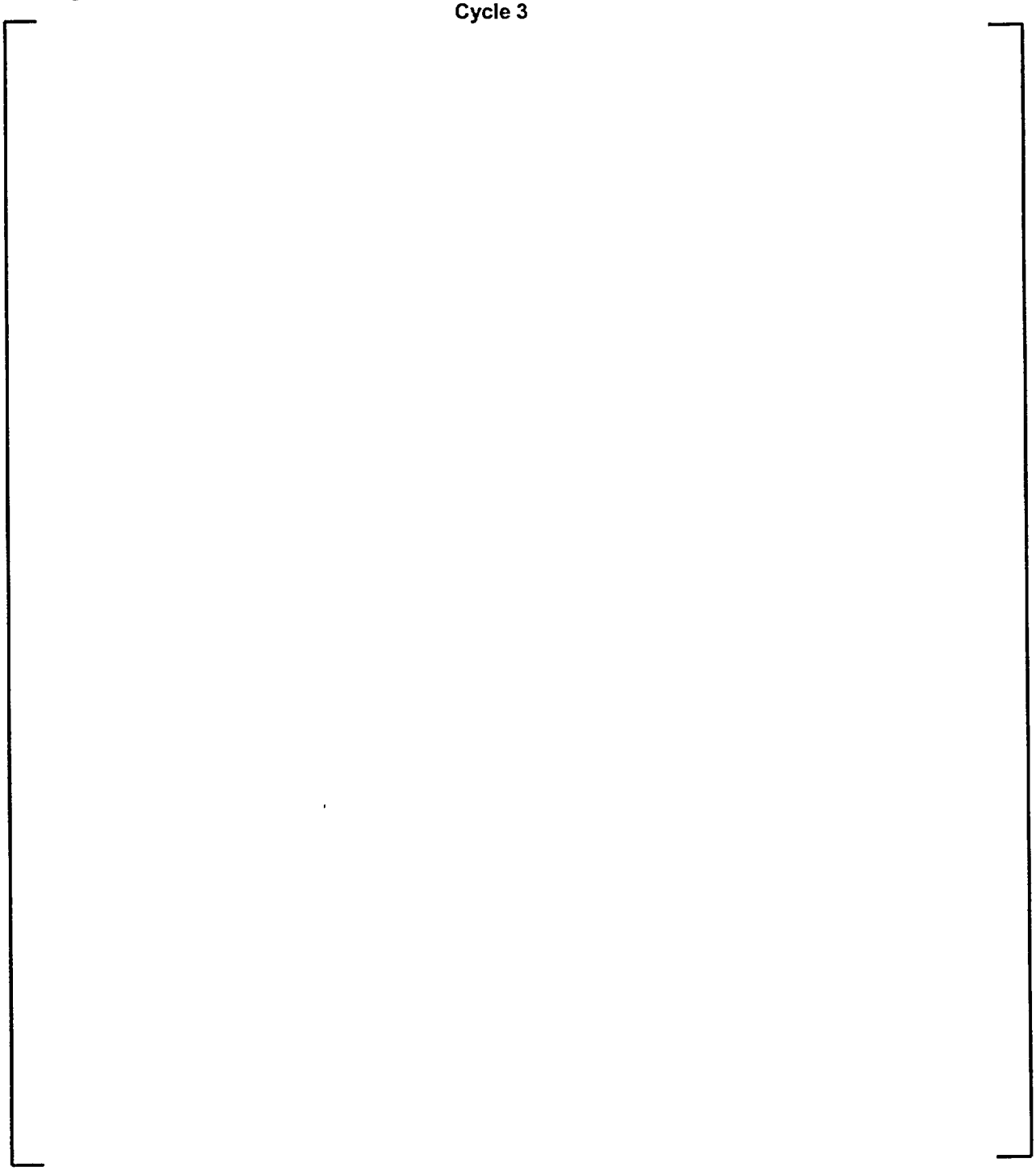

a, b, c

Figure 4-23: Critical Boron Concentration Versus Cycle Burnup Comparisons: Plant F Cycle 11 –Calculated values with and without B10 correction

a, b,

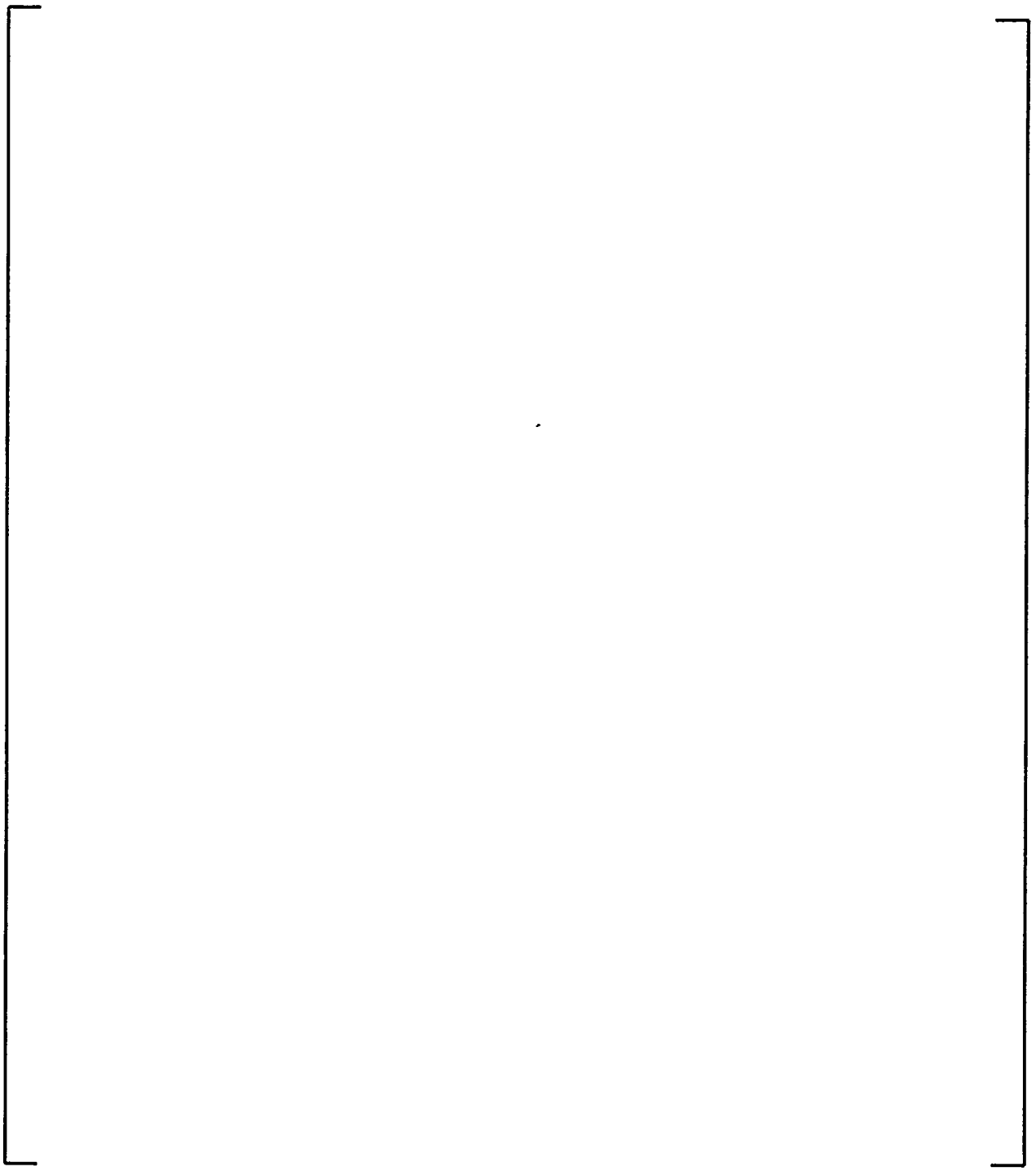

Figure 4-24: Assembly Average Power Distribution: Plant A, Cycle 10, 3355 MWD/MTU burnup

a, b, c

Figure 4-25: Assembly Average Power Distribution: Plant A, Cycle 10, 11958 MWD/MTU burnup

[a, b, c]

Figure 4-26: Assembly Average Power Distribution: Plant A, Cycle 11, 1460 MWD/MTU burnup

[a, b, c]

Figure 4-27: Assembly Average Power Distribution: Plant A, Cycle 11, 13052 MWD/MTU burnup

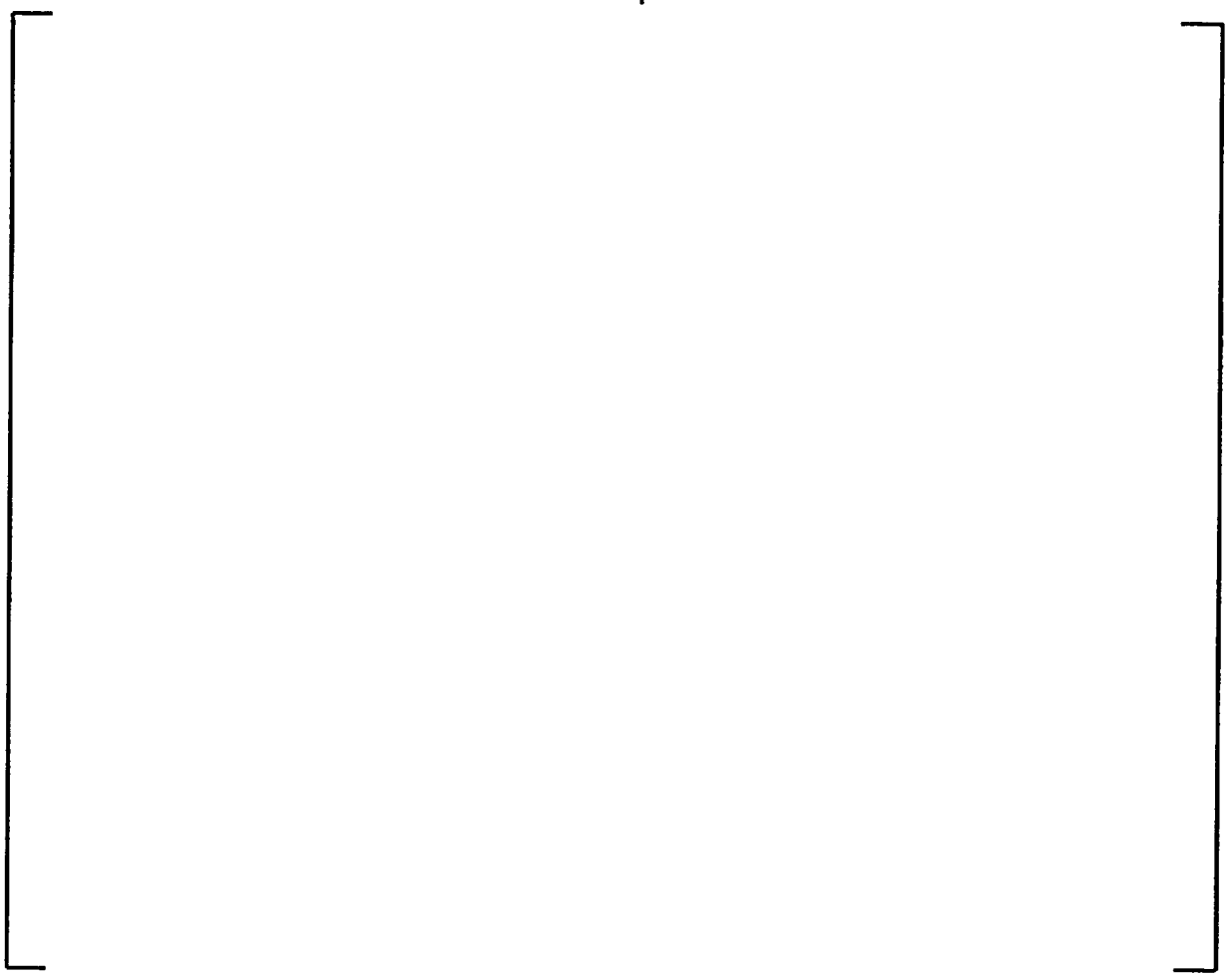

a, b, c

Figure 4-28: Assembly Average Power Distribution: Plant A, Cycle 11, 19738 MWD/MTU burnup

[a, b, c

]

Figure 4-29: Assembly Average Power Distribution: Plant B, Cycle 17, 386 MWD/MTU burnup

a, b, c

Figure 4-30: Assembly Average Power Distribution: Plant B, Cycle 17, 7878 MWD/MTU burnup

a, b, c

Figure 4-31: Assembly Average Power Distribution: Plant B, Cycle 17, 10930 MWD/MTU burnup

a, b, c

Figure 4-32: Assembly Average Power Distribution: Plant B, Cycle 18, 1375 MWD/MTU burnup

a, b, c

Figure 4-33: Assembly Average Power Distribution: Plant B, Cycle 18, 6926 MWD/MTU burnup

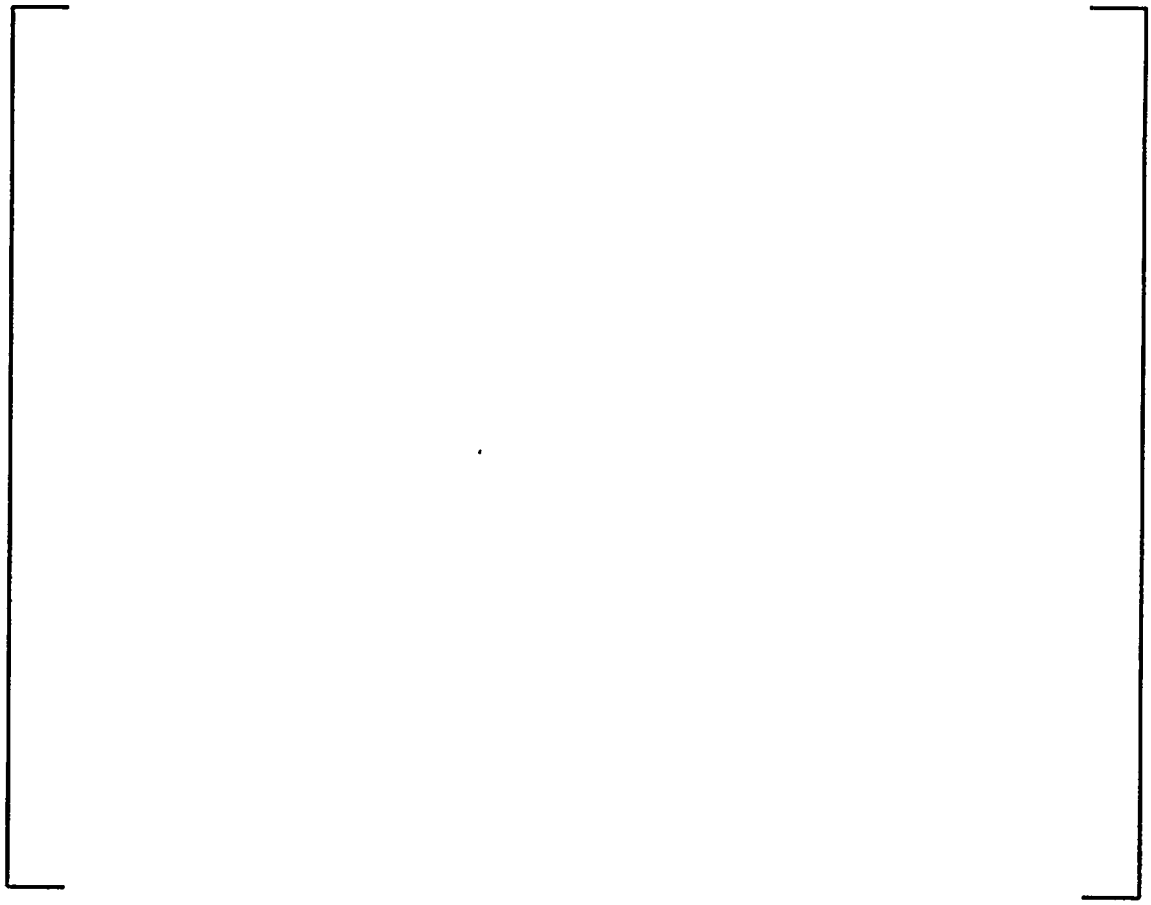

a, b, c

Figure 4-34: Assembly Average Power Distribution: Plant C, Cycle 25, 262 MWD/MTU burnup

a, b, c

Figure 4-35: Assembly Average Power Distribution: Plant C, Cycle 25, 7080 MWD/MTU burnup

a, b, c

Figure 4-36: Assembly Average Power Distribution: Plant C, Cycle 25, 13400 MWD/MTU burnup

Figure 4-37: Assembly Average Power Distribution: Plant C, Cycle 26, 788 MWD/MTU burnup

a, b, c

Figure 4-38: Assembly Average Power Distribution: Plant C, Cycle 26, 8073 MWD/MTU burnup

a, b, c

Figure 4-39: Assembly Average Power Distribution: Plant C, Cycle 26, 14838 MWD/MTU burnup

a, b, c

Figure 4-40: Assembly Average Power Distribution: Plant D, Cycle 10, 1980 MWD/MTU burnup

a, b, c

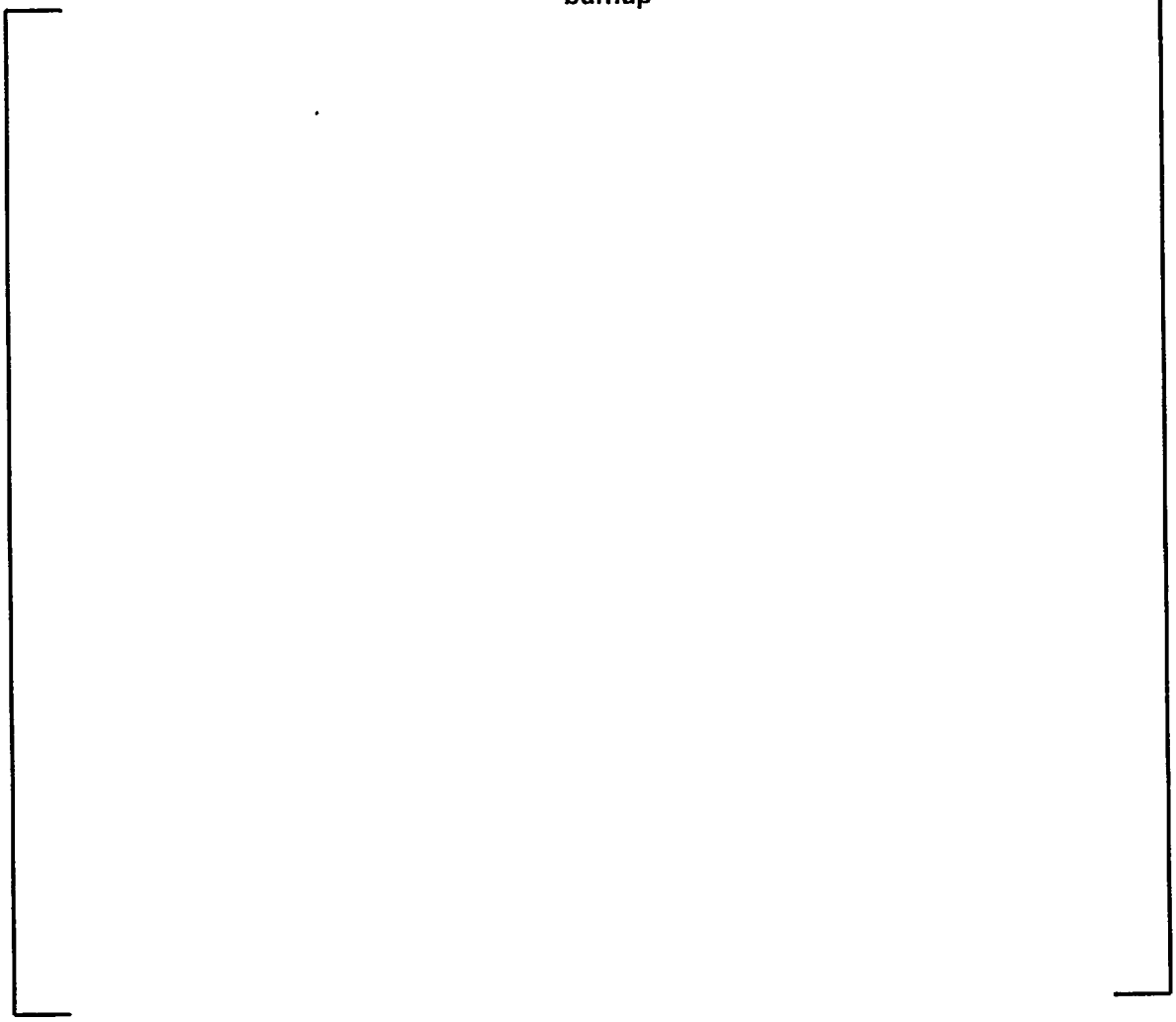

Figure 4-41: Assembly Average Power Distribution: Plant D, Cycle 10, 9700 MWD/MTU burnup

a, b, c

Figure 4-42: Assembly Average Power Distribution: Plant D, Cycle 10, 20829 MWD/MTU burnup

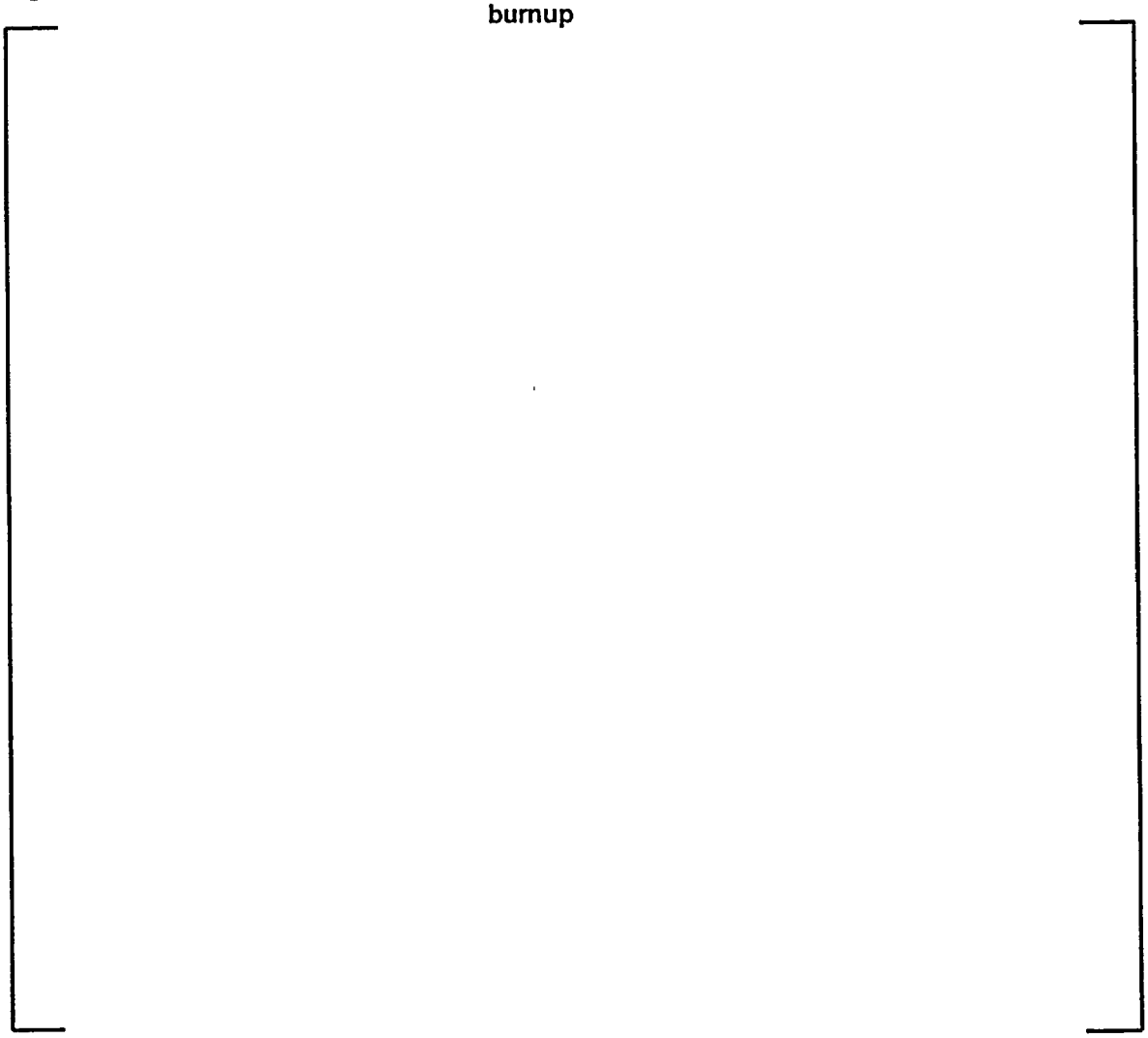

a, b, c

Figure 4-43: Assembly Average Power Distribution: Plant D, Cycle 11, 1010 MWD/MTU burnup

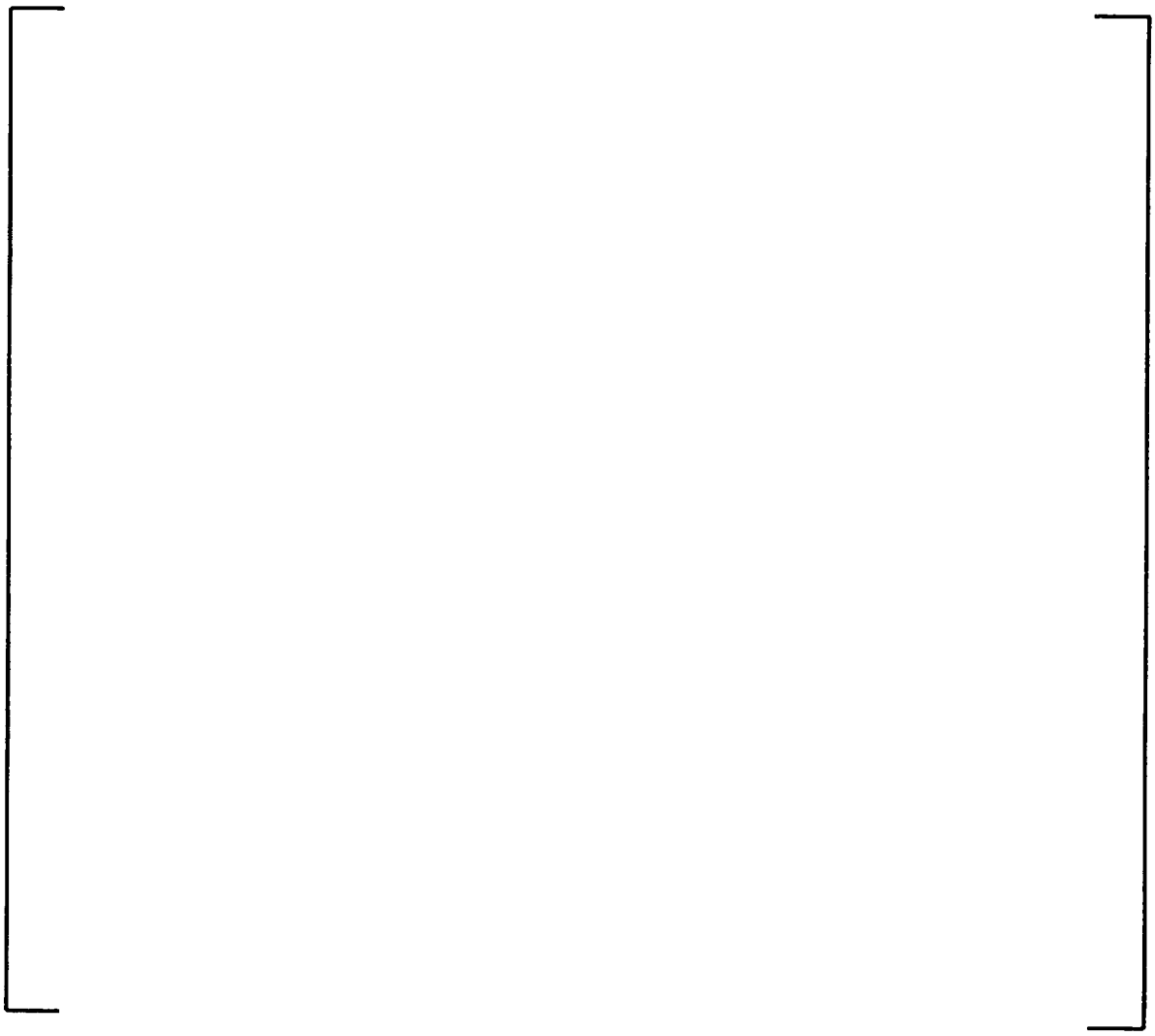

a, b, c

Figure 4-44: Assembly Average Power Distribution: Plant D, Cycle 11, 7309 MWD/MTU burnup

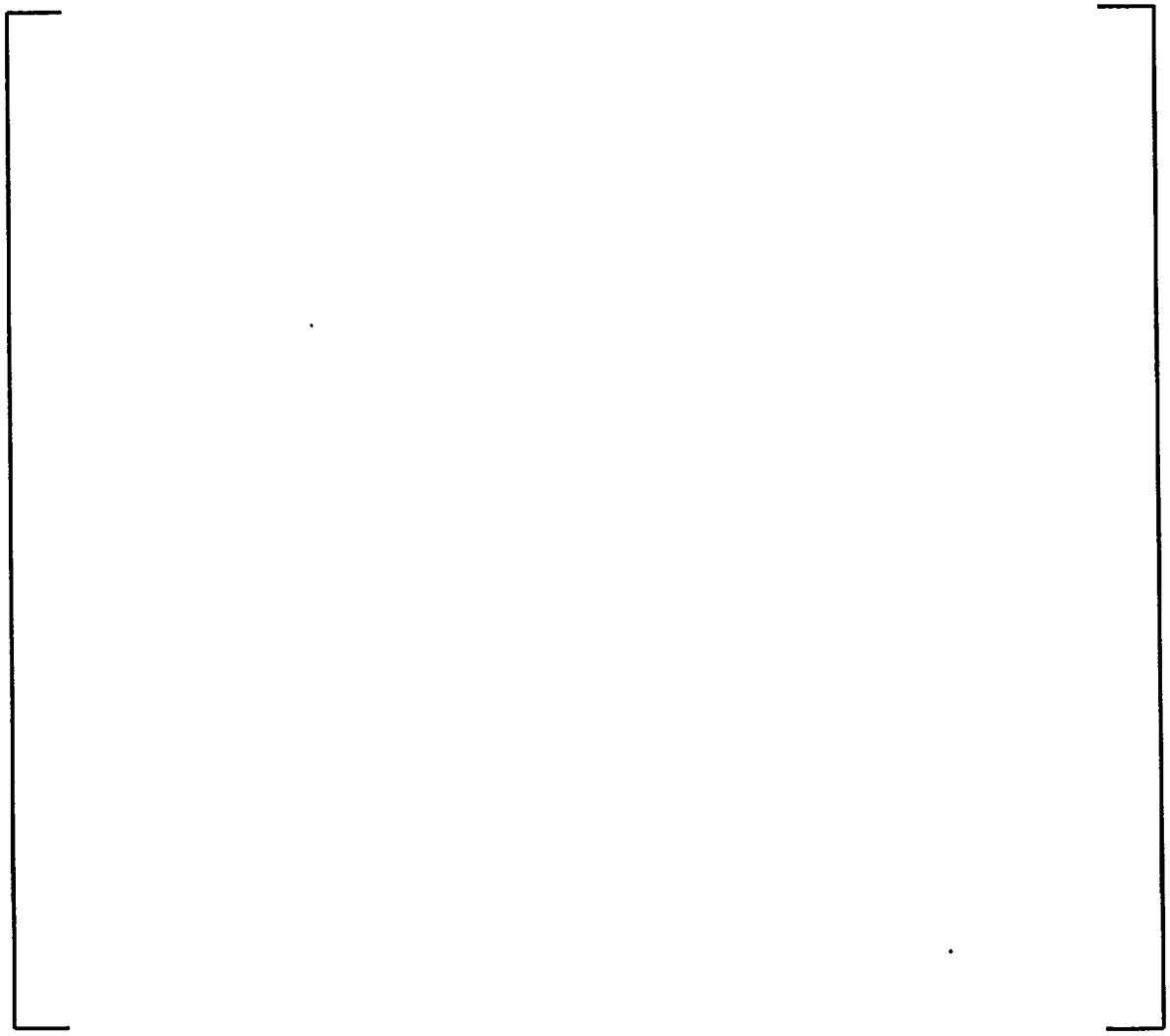

a, b, c

Figure 4-45: Assembly Average Power Distribution: Plant D, Cycle 11, 14998 MWD/MTU burnup

a, b, c

Figure 4-46: Assembly Average Power Distribution: Plant J, Cycle 10, 4282 MWD/MTU burnup

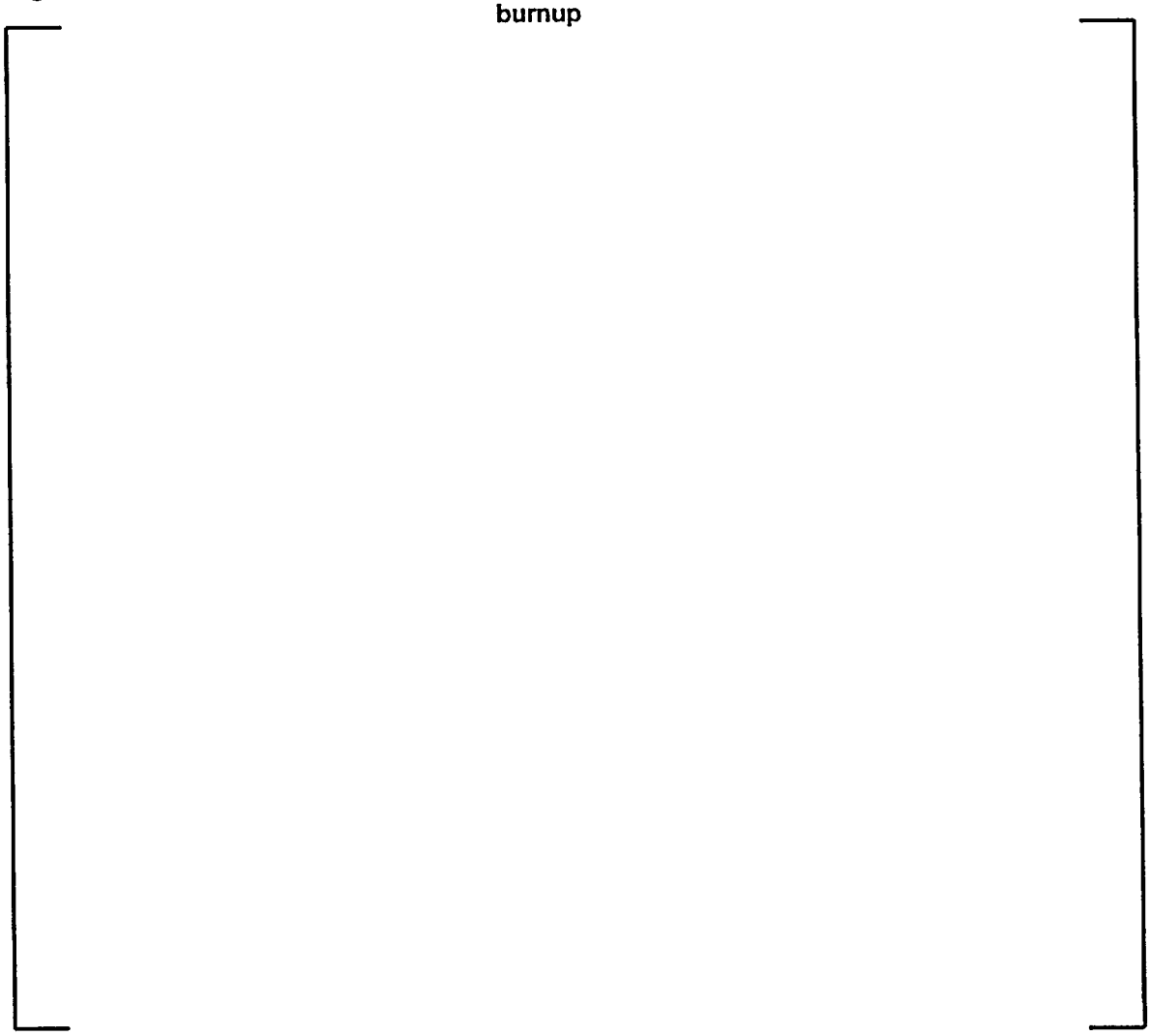

a, b, c

Figure 4-47: Assembly Average Power Distribution: Plant J, Cycle 10, 11864 MWD/MTU burnup

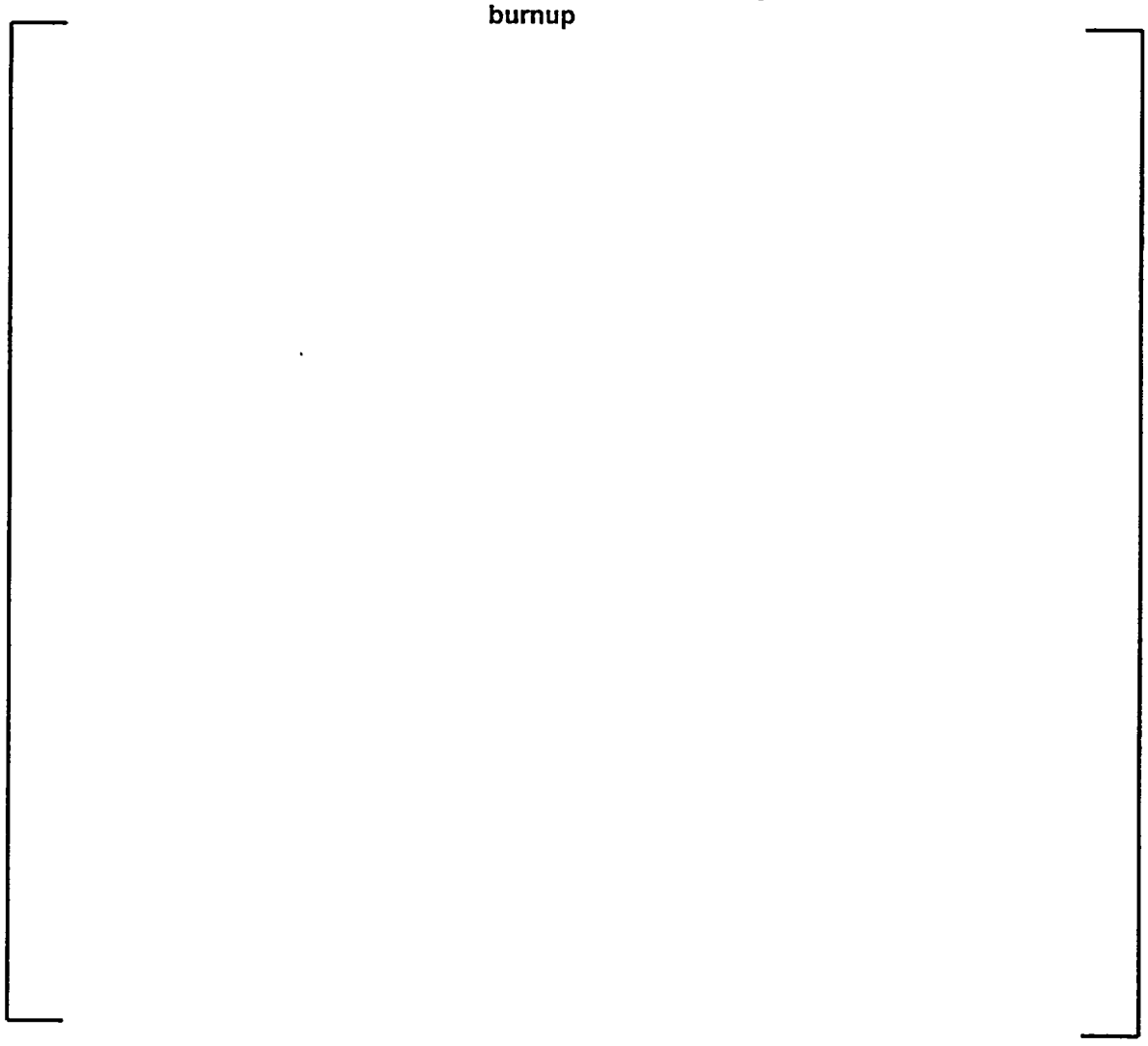

a, b, c

Figure 4-48: Assembly Average Power Distribution: Plant J, Cycle 10, 20700 MWD/MTU burnup

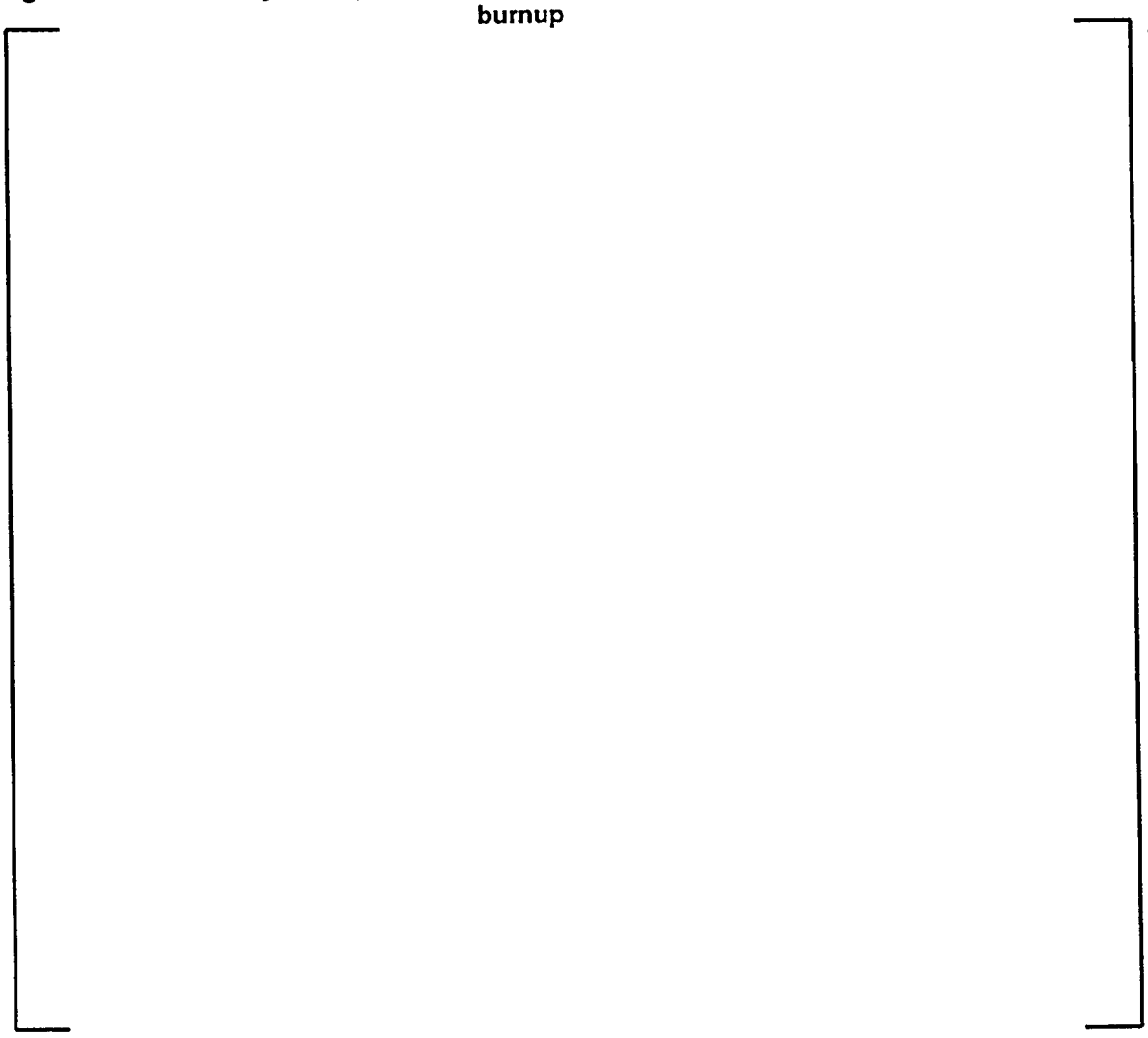

a, b, c

Figure 4-49: Assembly Average Power Distribution: Plant J, Cycle 11, 638 MWD/MTU burnup

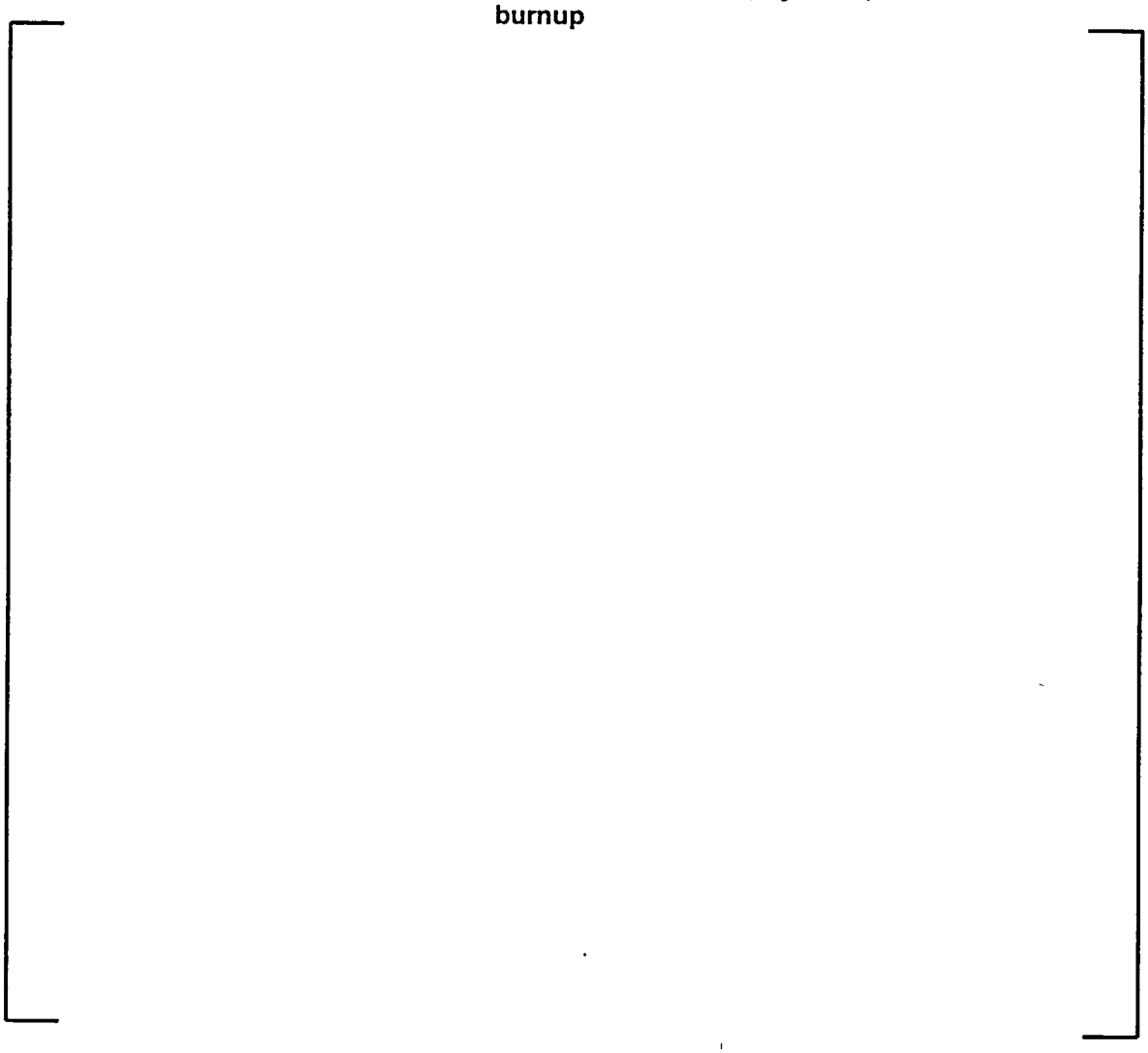

a, b, c

Figure 4-50: Assembly Average Power Distribution: Plant J, Cycle 11, 12294 MWD/MTU burnup

a, b, c

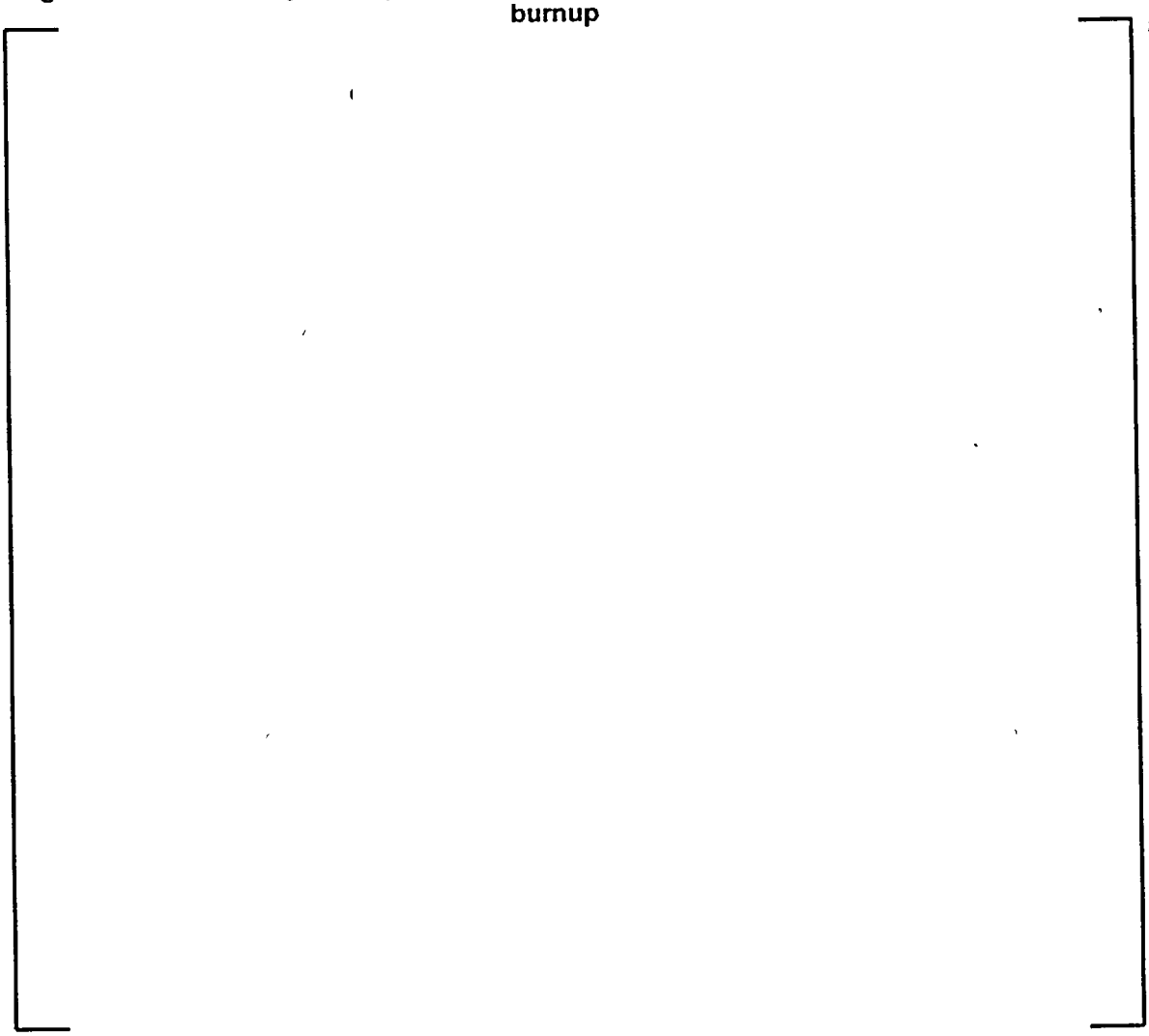

Figure 4-51: Assembly Average Power Distribution: Plant J, Cycle 11, 20539 MWD/MTU burnup

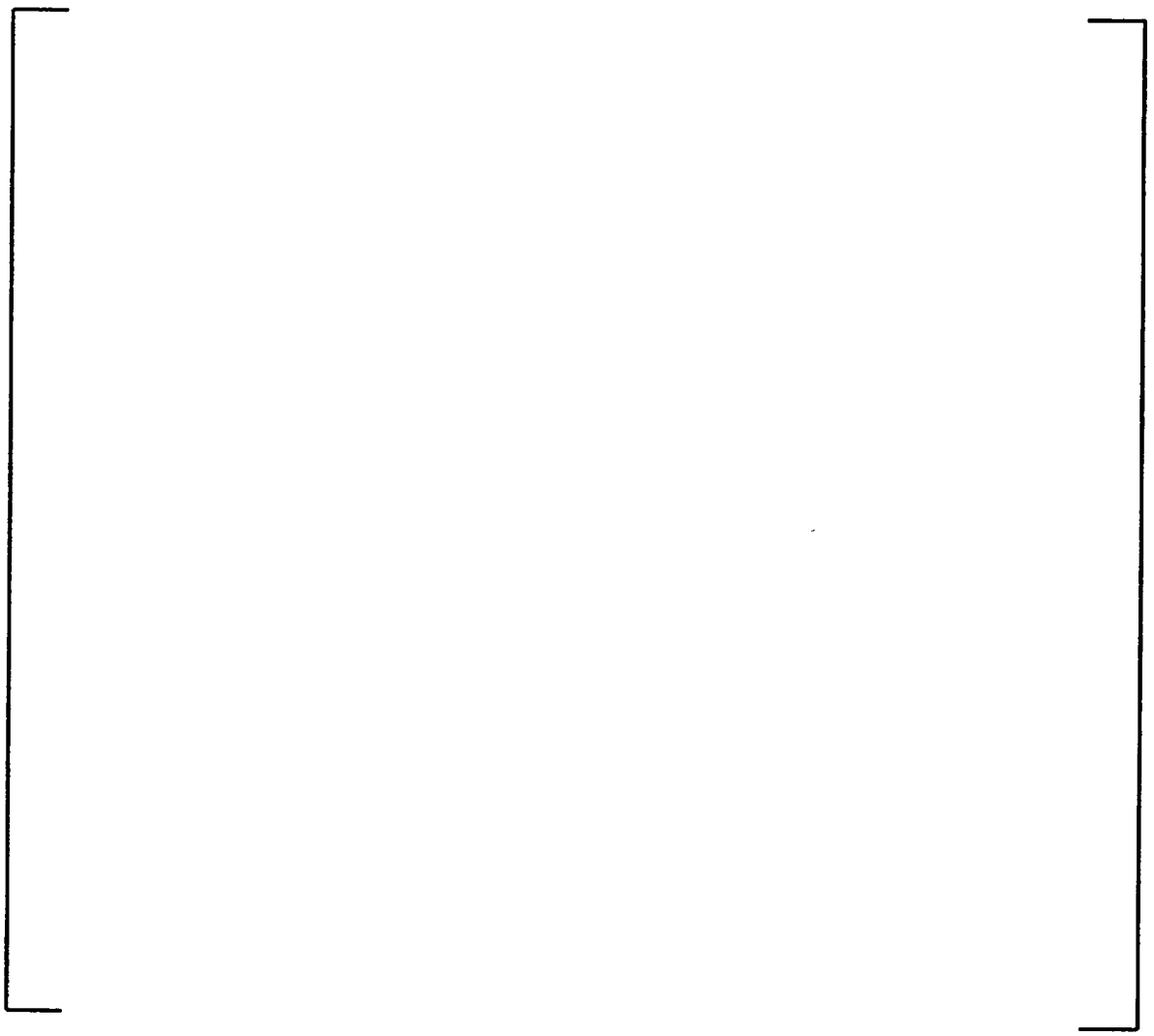

a, b, c

Figure 4-52: Assembly Average Power Distribution (PARAGON versus PHOENIX-P) : Plant A, Cycle 10 BOC

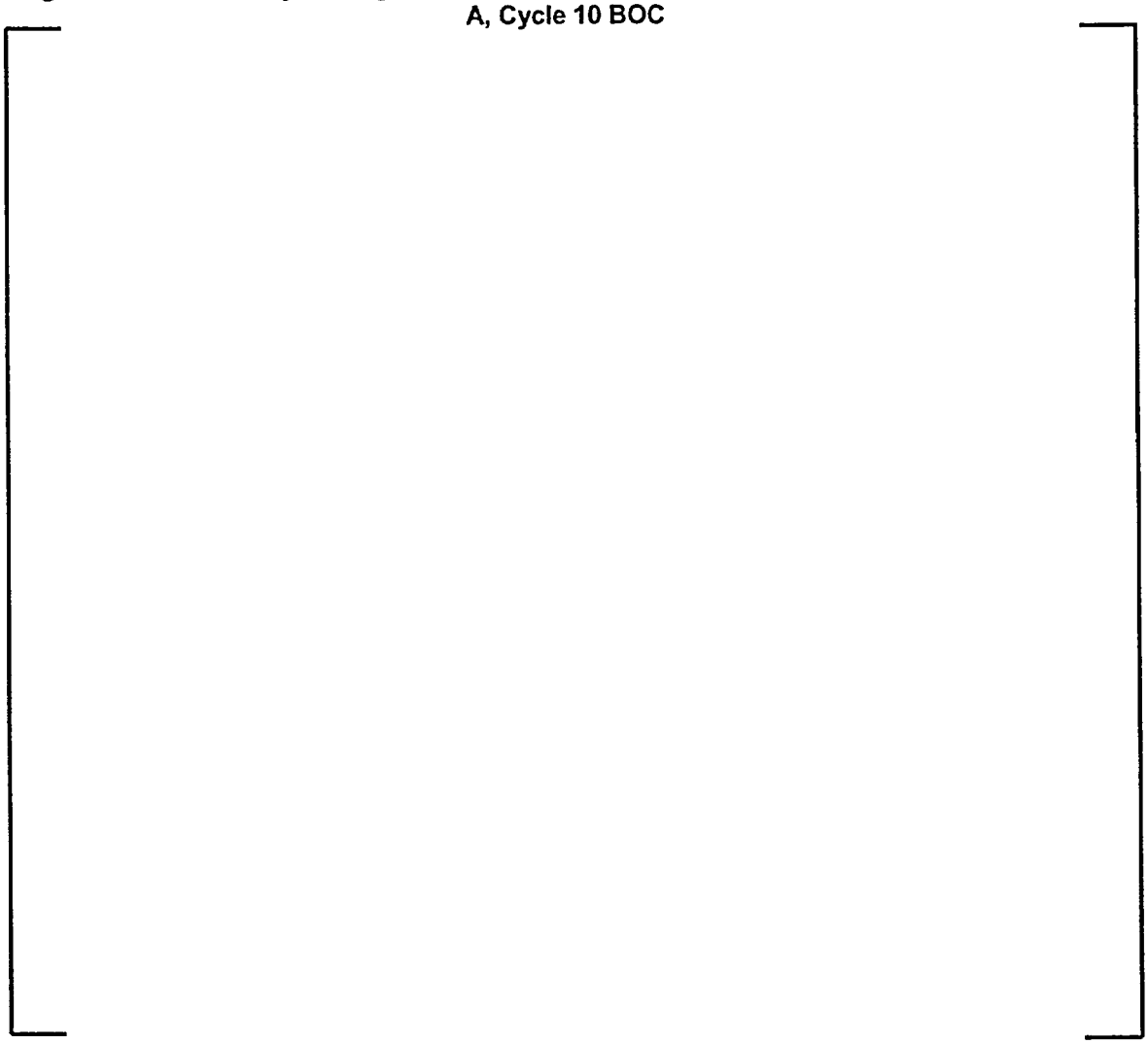

a, b, c

Figure 4-53: Assembly Average Power Distribution (PARAGON versus PHOENIX-P) : Plant A, Cycle 10 EOC

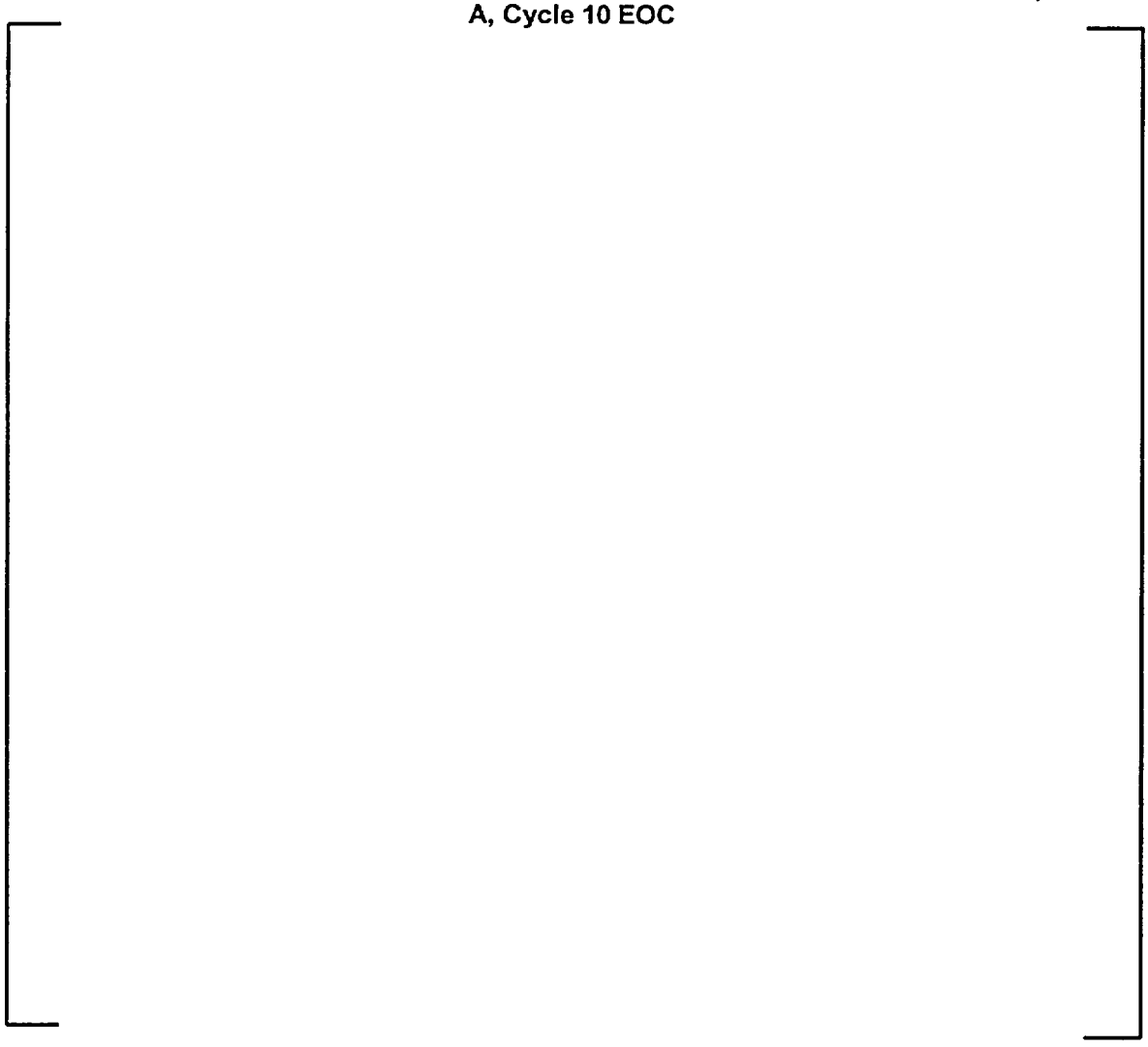

a, b, c

Figure 4-54: Assembly Average Burnup Distribution (PARAGON versus PHOENIX-P) : Plant A, Cycle 10 EOC

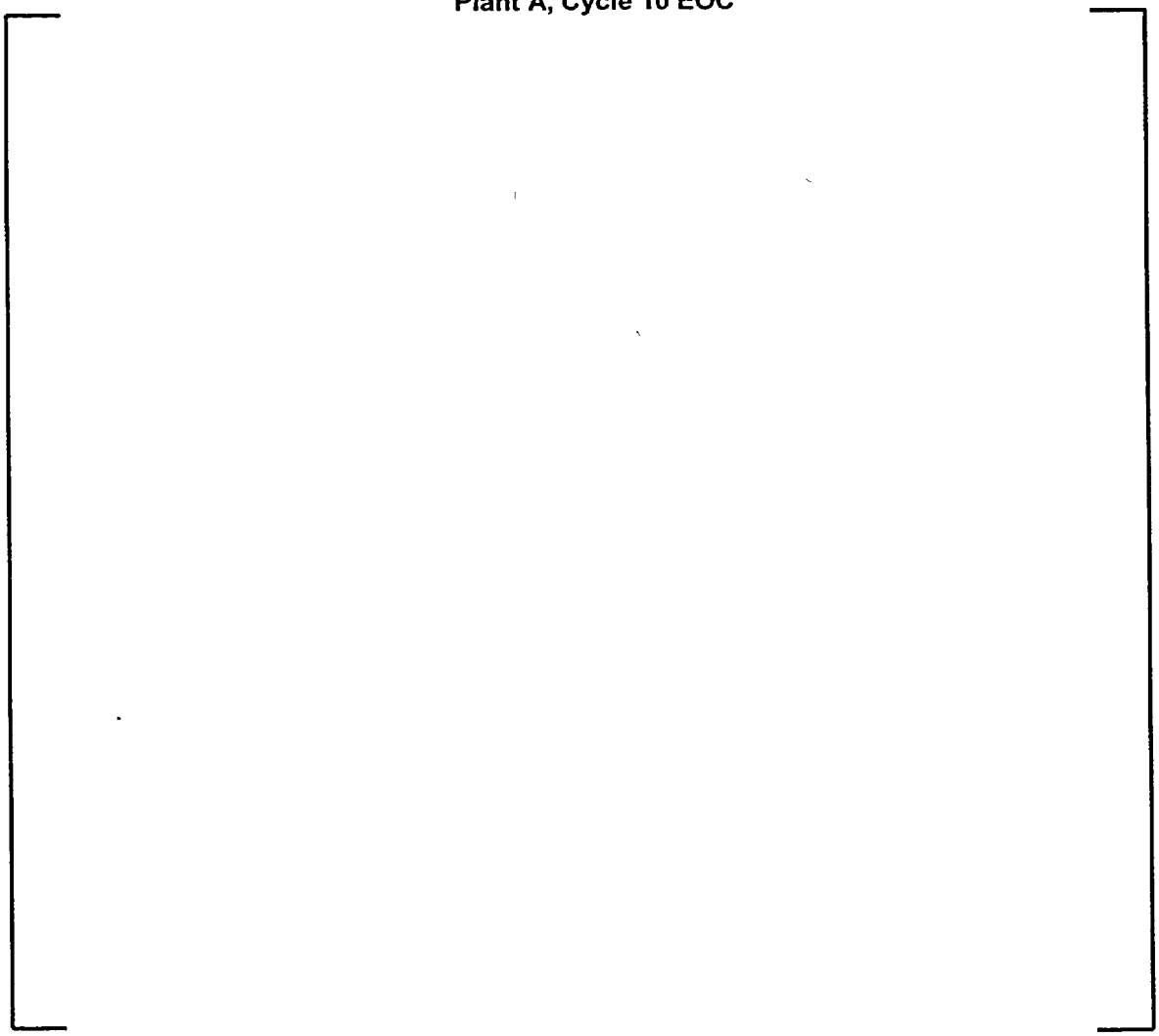

a, b, c

Figure 4-55: Assembly Average Power Distribution (PARAGON versus PHOENIX-P) : Plant A, Cycle 11 BOC

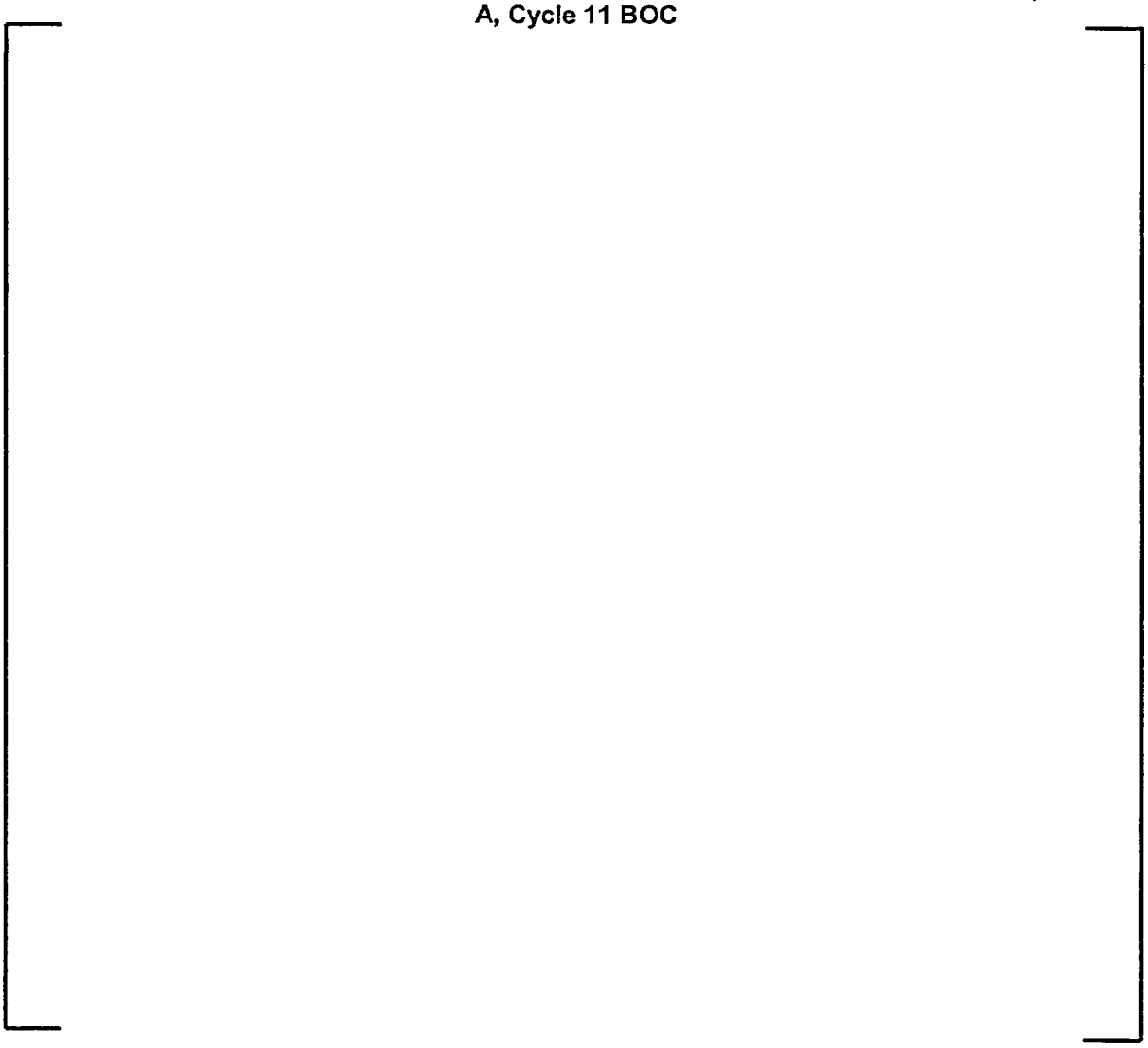

a, b, c

Figure 4-56: Assembly Average Power Distribution (PARAGON versus PHOENIX-P) : Plant A, Cycle 11 EOC

a, b, c

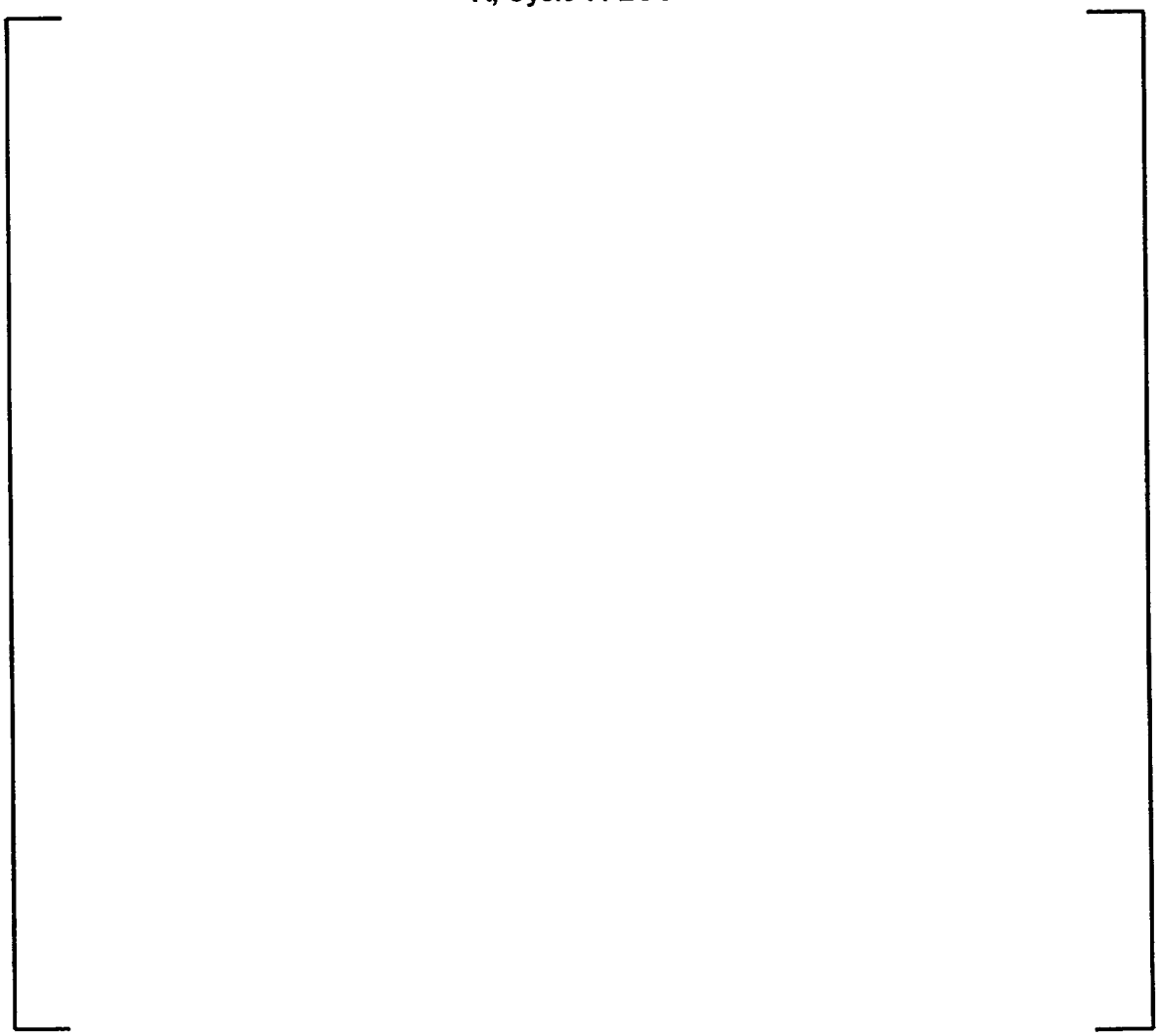

Figure 4-57: Assembly Average Burnup Distribution (PARAGON versus PHOENIX-P) : Plant A, Cycle 11 EOC

a, b, c

Figure 4-58: Assembly Average Power Distribution (PARAGON versus PHOENIX-P) : Plant C, Cycle 25 BOC

a, b, c

Figure 4-59: Assembly Average Power Distribution (PARAGON versus PHOENIX-P) : Plant C, Cycle 25 EOC

a, b, c

Figure 4-60: Assembly Average Burnup Distribution (PARAGON versus PHOENIX-P) : Plant C, Cycle 25 EOC

a, b, c

Figure 4-61: Assembly Average Power Distribution (PARAGON versus PHOENIX-P) : Plant C, Cycle 26 BOC

a, b, c

Figure 4-62: Assembly Average Power Distribution (PARAGON versus PHOENIX-P) : Plant C, Cycle 26 EOC

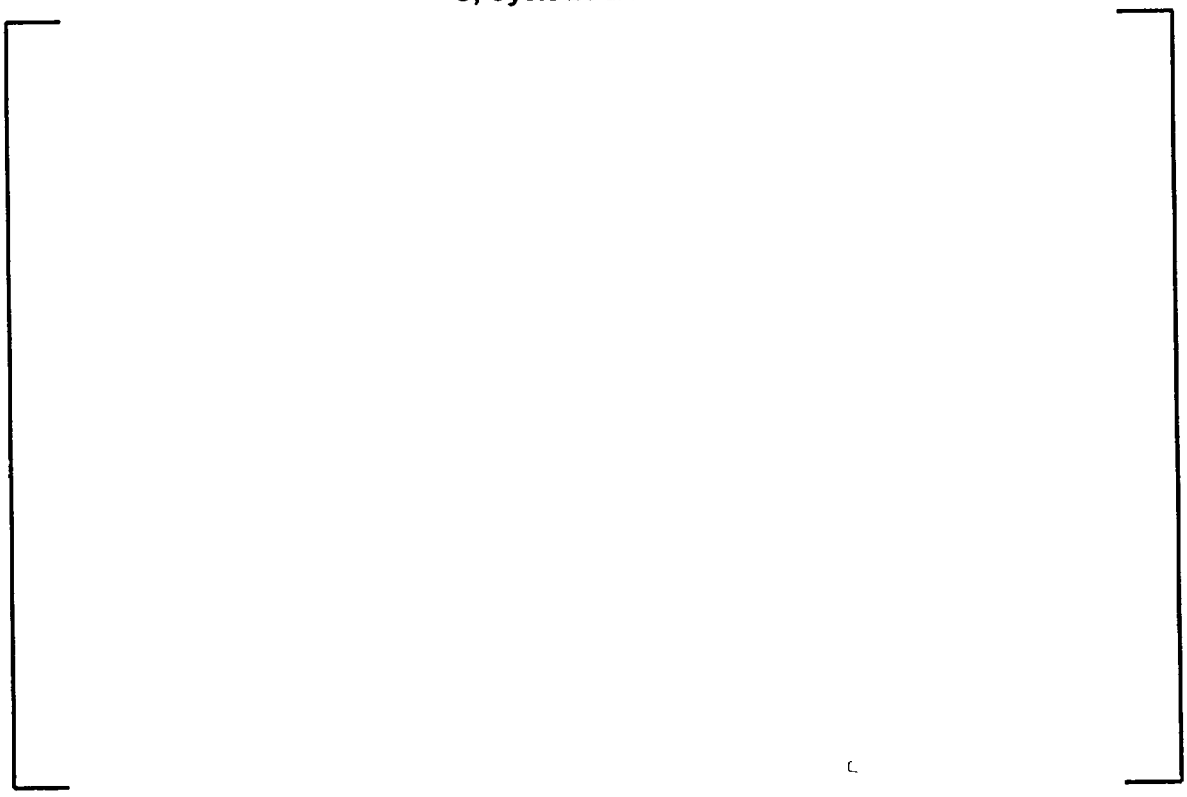

a, b, c

Figure 4-63: Assembly Average Burnup Distribution (PARAGON versus PHOENIX-P) : Plant C, Cycle 26 EOC

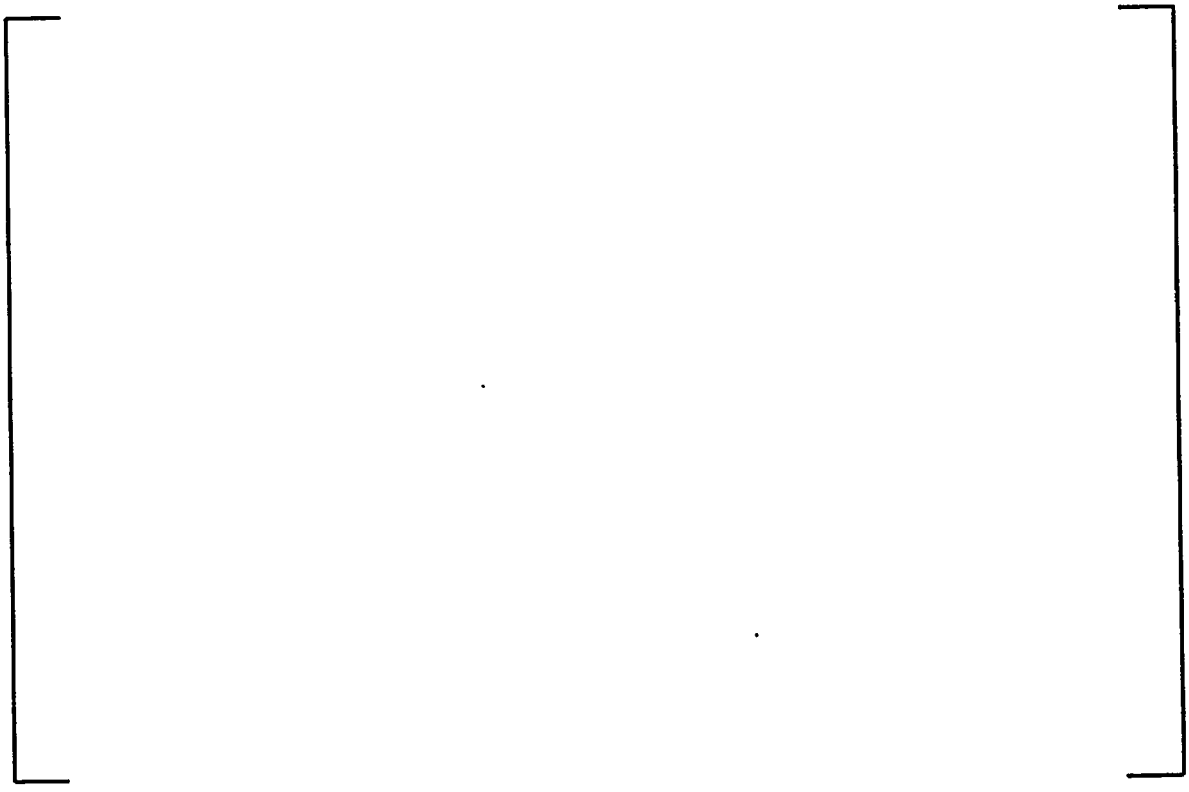

a, b, c

Figure 4-64: Assembly Average Power Distribution (PARAGON versus PHOENIX-P) : Plant D, Cycle 10 BOC

a, b, c

Figure 4-65: Assembly Average Power Distribution (PARAGON versus PHOENIX-P) : Plant D, Cycle 10 EOC

a, b, c

Figure 4-66: Assembly Average Burnup Distribution (PARAGON versus PHOENIX-P) : Plant D, Cycle 10 EOC

[a, b, c]

Figure 4-67: Assembly Average Power Distribution (PARAGON versus PHOENIX-P) : Plant D, Cycle 11 BOC

a, b, c

Figure 4-68: Assembly Average Power Distribution (PARAGON versus PHOENIX-P) : Plant D, Cycle 11 EOC

a, b, c

Figure 4-69: Assembly Average Burnup Distribution (PARAGON versus PHOENIX-P) : Plant D, Cycle 11 EOC

[a, b, c

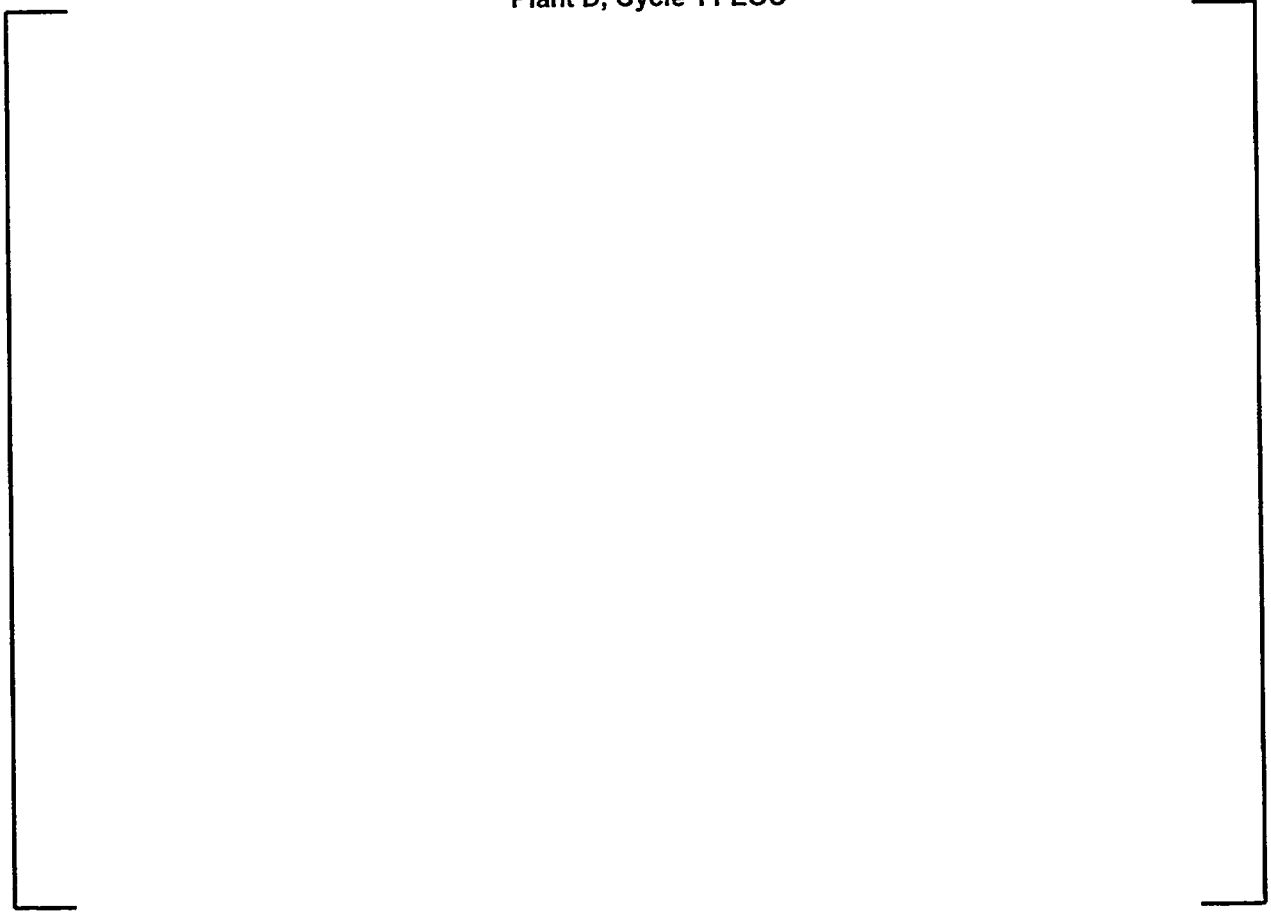

]

Figure 4-70: Assembly Average Power Distribution (PARAGON versus PHOENIX-P) : Plant E, Cycle 25 BOC

a, b, c

Figure 4-71: Assembly Average Power Distribution (PARAGON versus PHOENIX-P) : Plant E, Cycle 25 EOC

a, b, c

Figure 4-72: Assembly Average Burnup Distribution (PARAGON versus PHOENIX-P) : Plant E, Cycle 25 EOC

a, b, c

Figure 4-73: Assembly Average Power Distribution (PARAGON versus PHOENIX-P) : Plant F, Cycle 11 BOC

a, b, c

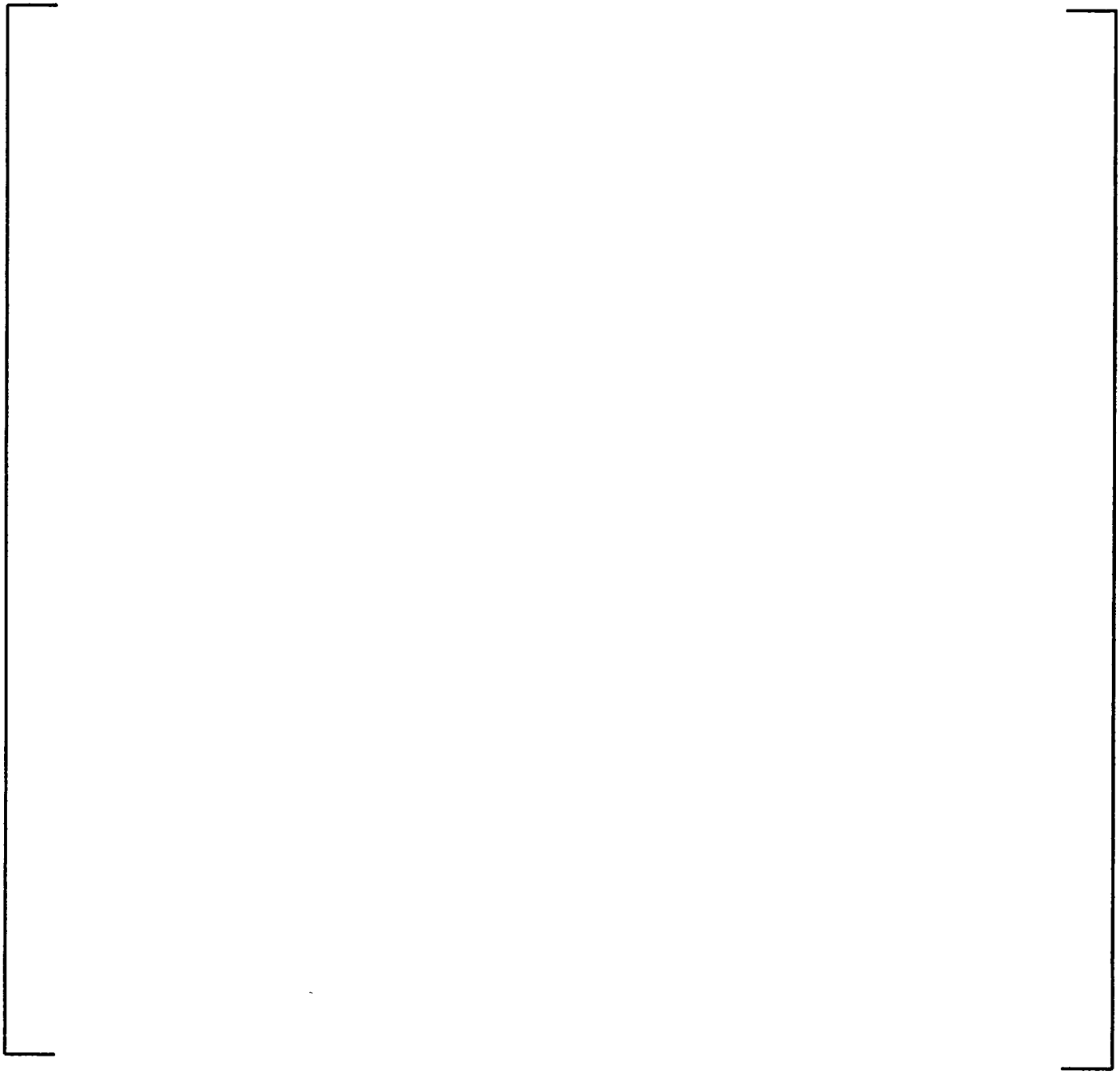

Figure 4-74: Assembly Average Power Distribution (PARAGON versus PHOENIX-P) : Plant F, Cycle 11 EOC

a, b, c

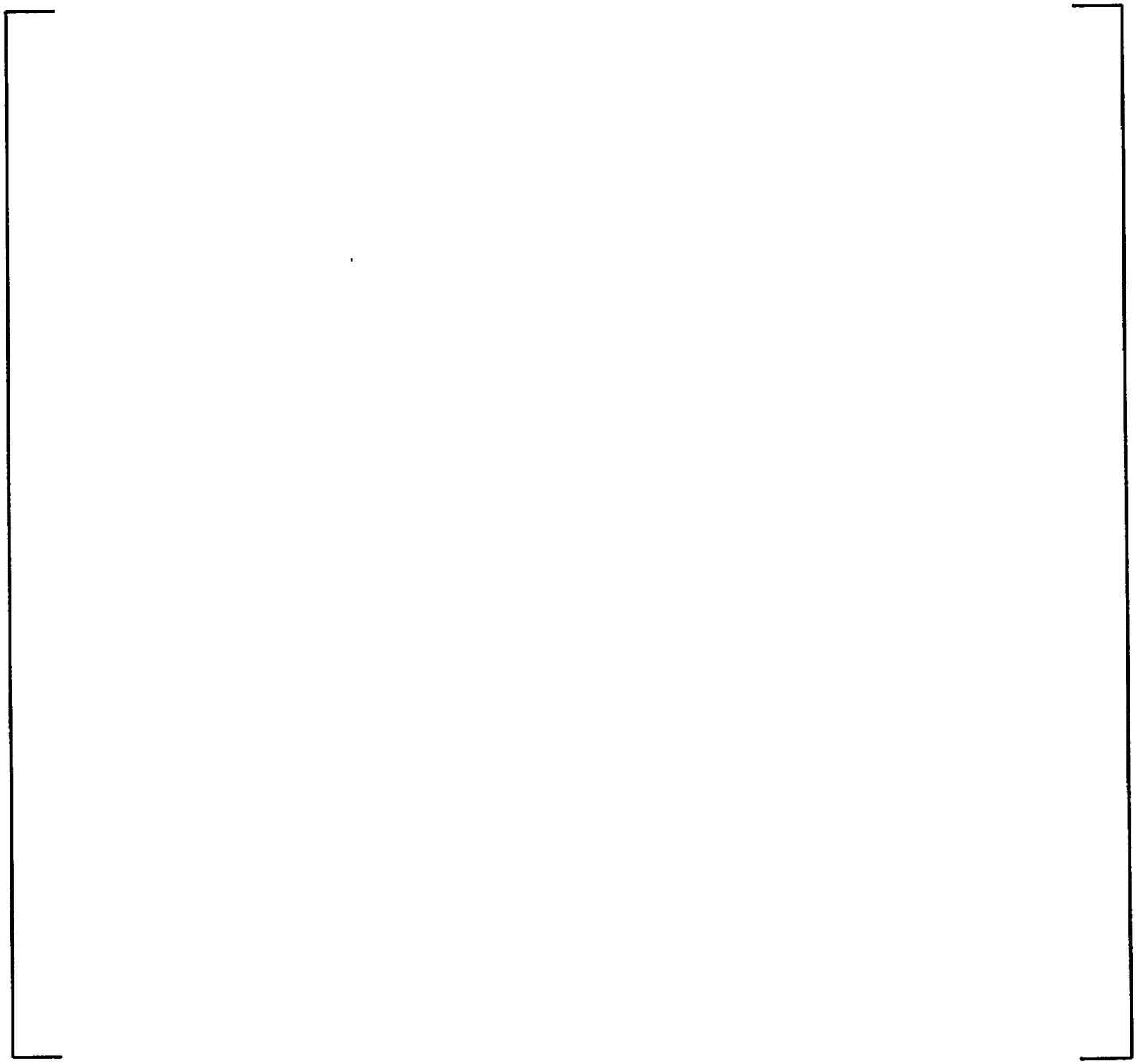

Figure 4-75: Assembly Average Burnup Distribution (PARAGON versus PHOENIX-P) : Plant F, Cycle 11 EOC

a, b, c

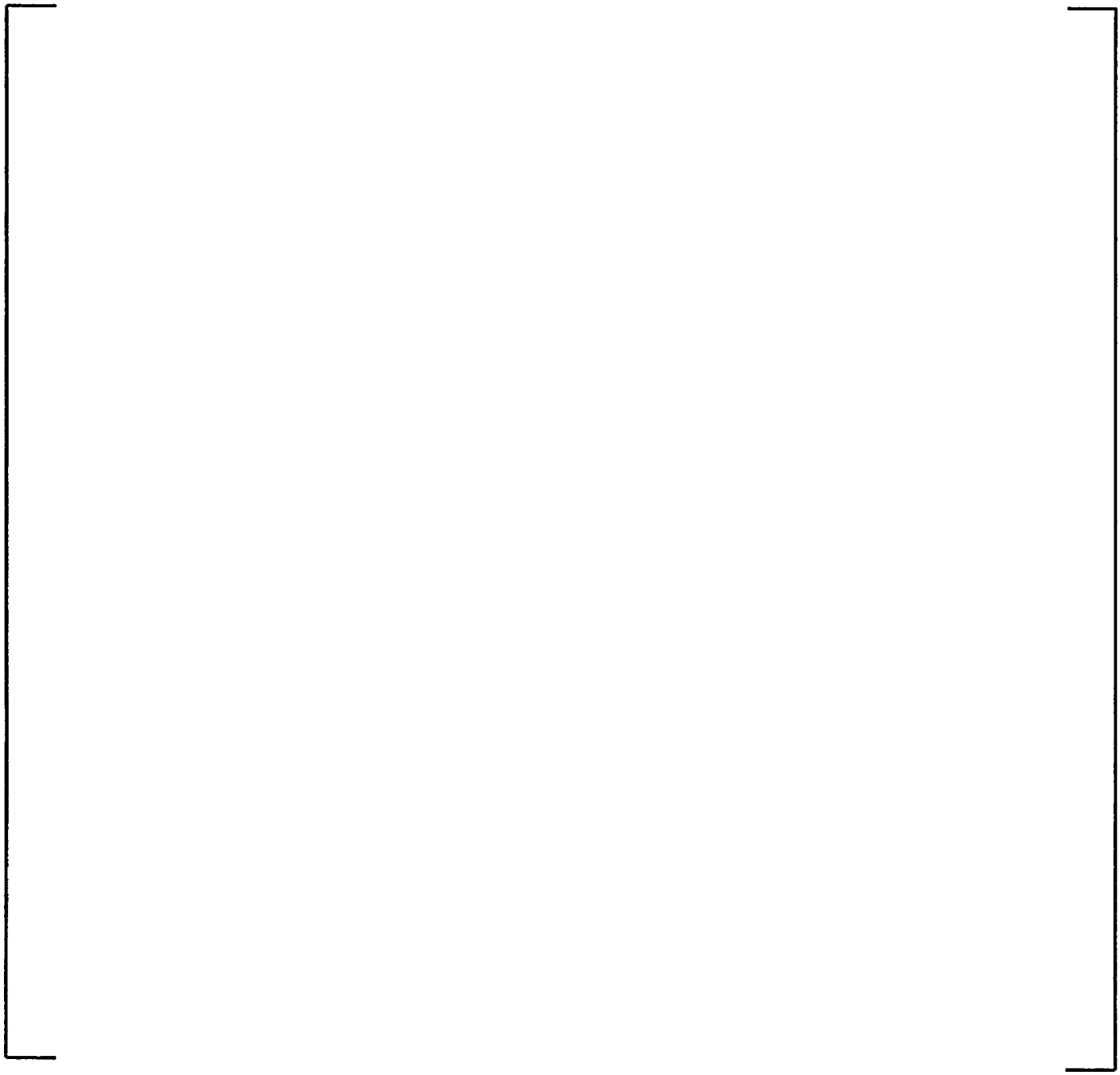

Figure 4-76: Assembly Average Power Distribution (PARAGON versus PHOENIX-P) : Plant F, Cycle 12 BOC

a, b, c

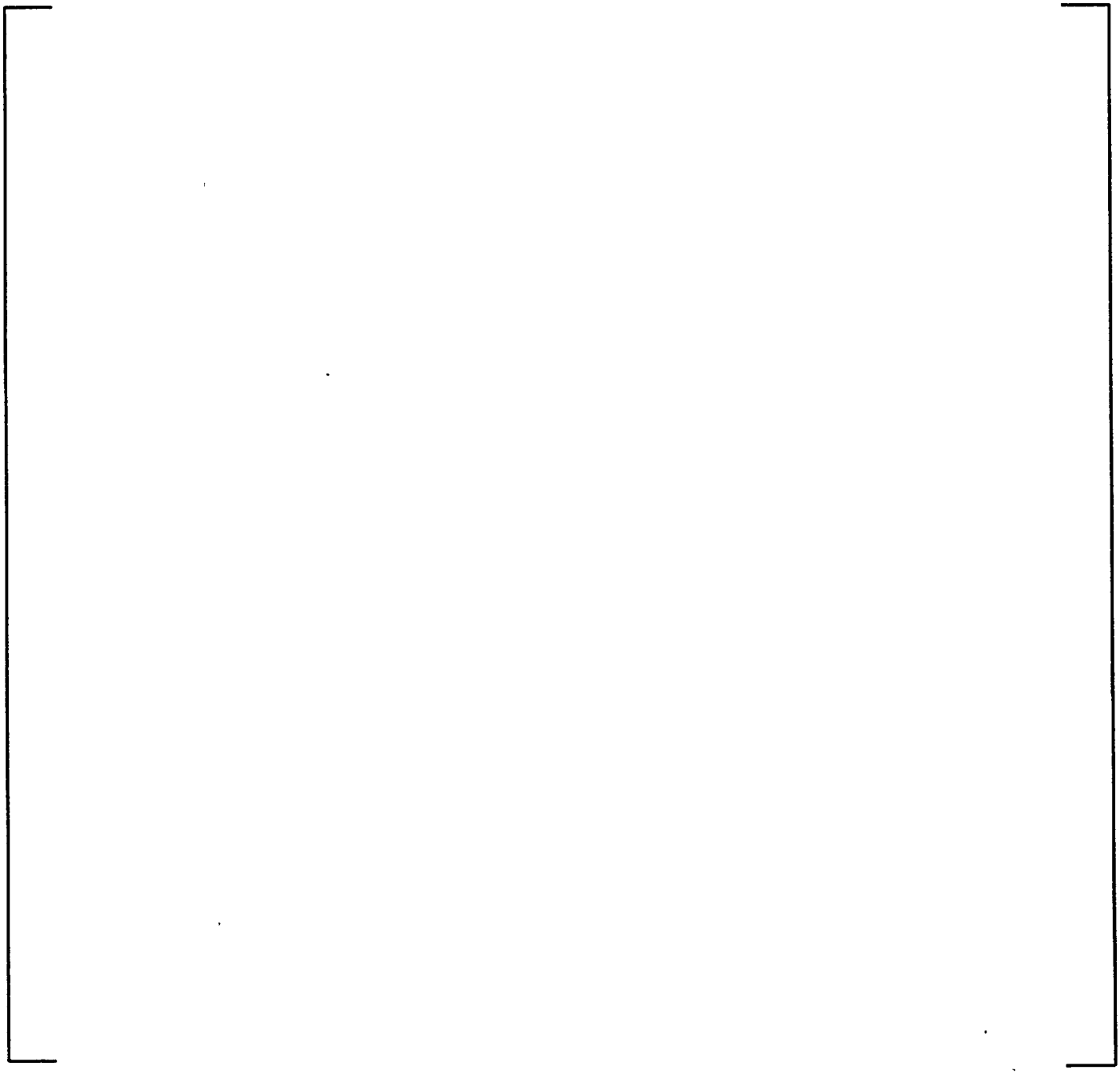

Figure 4-77: Assembly Average Power Distribution (PARAGON versus PHOENIX-P) : Plant F, Cycle 12 EOC

a, b, c

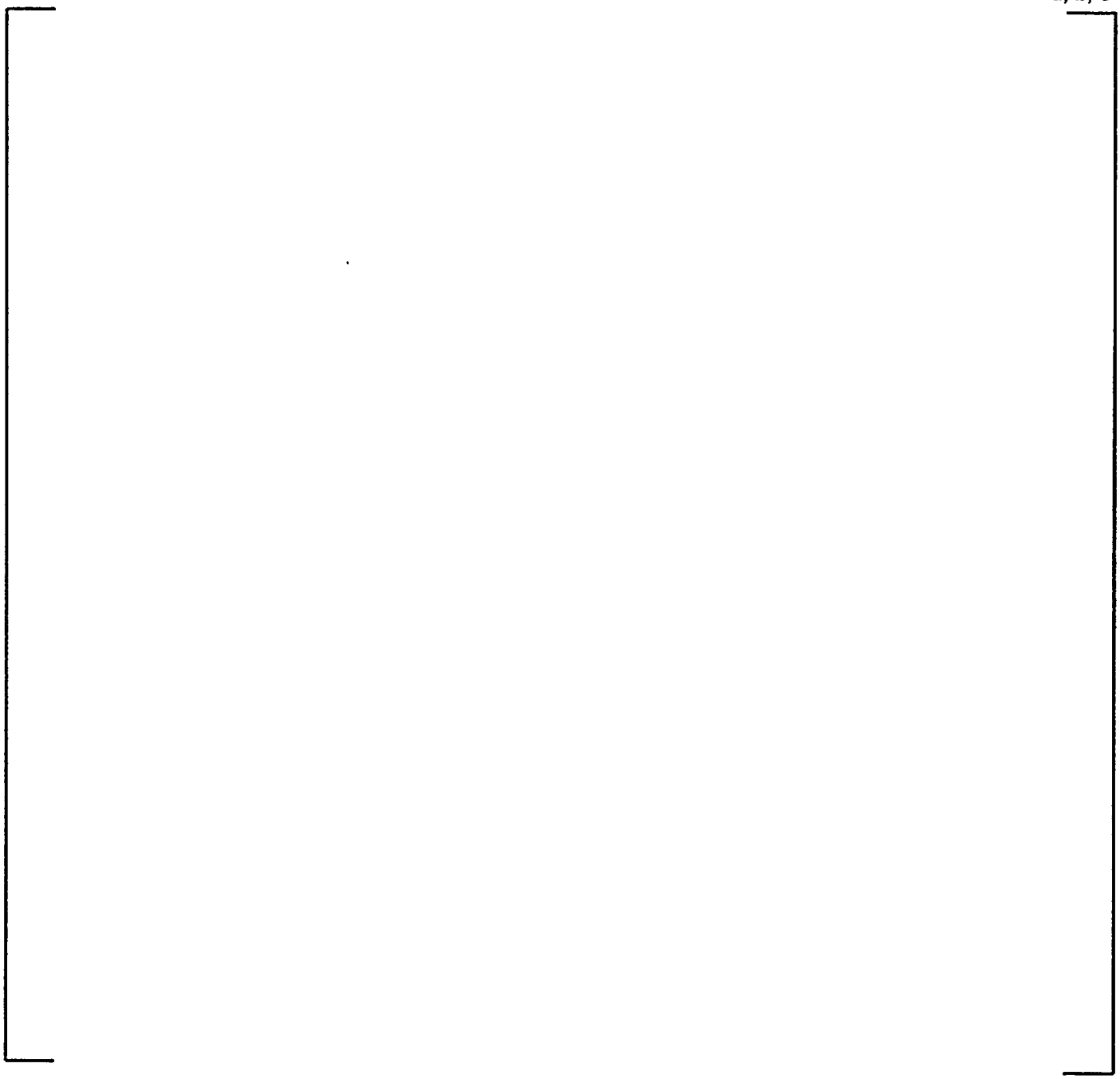

Figure 4-78: Assembly Average Burnup Distribution (PARAGON versus PHOENIX-P) : Plant F, Cycle 12 EOC

a, b, c

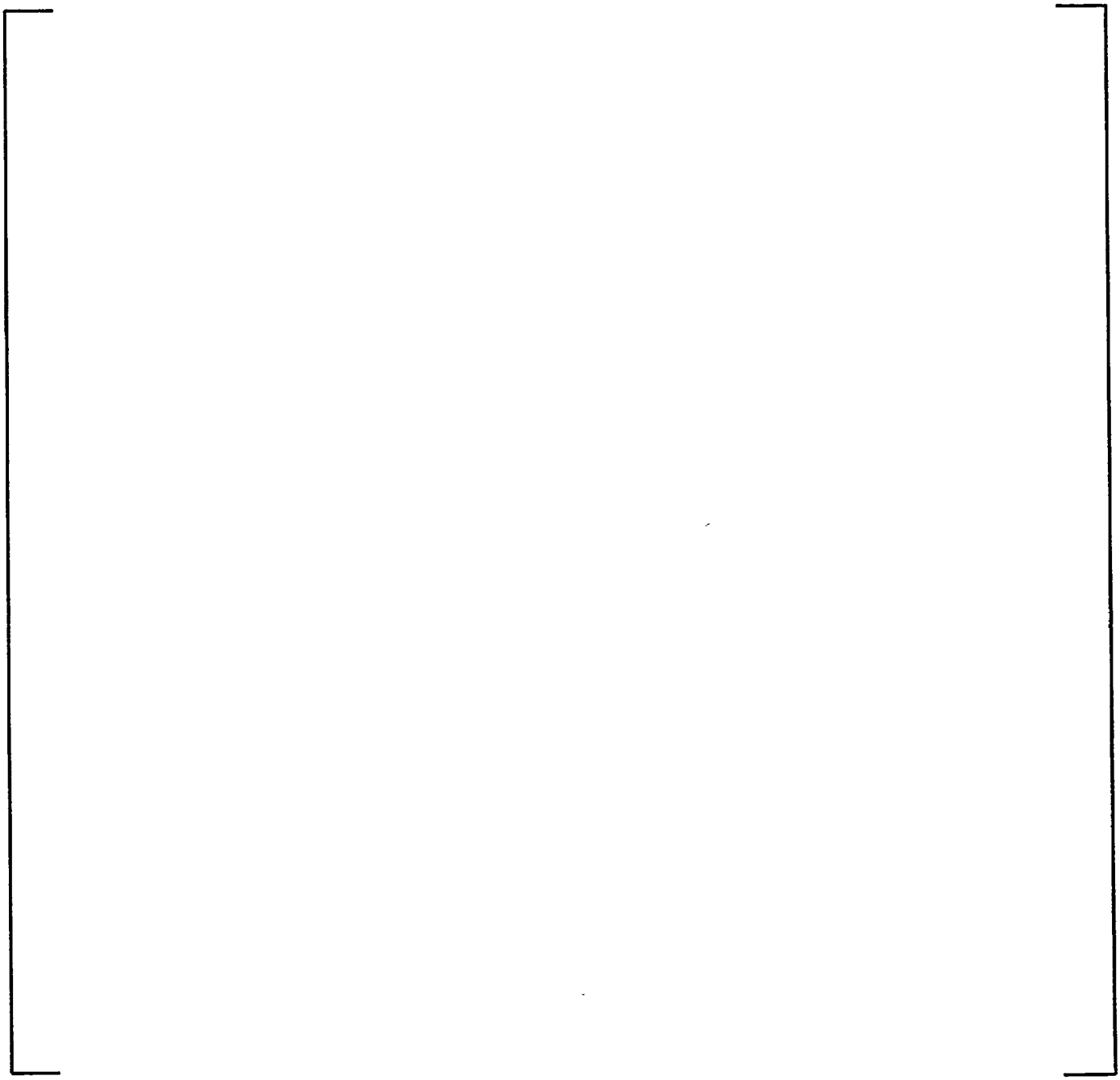

Figure 4-79: Core Average Axial Power Distribution (PARAGON versus PHOENIX-P) : Plant A, Cycle 10, BOC

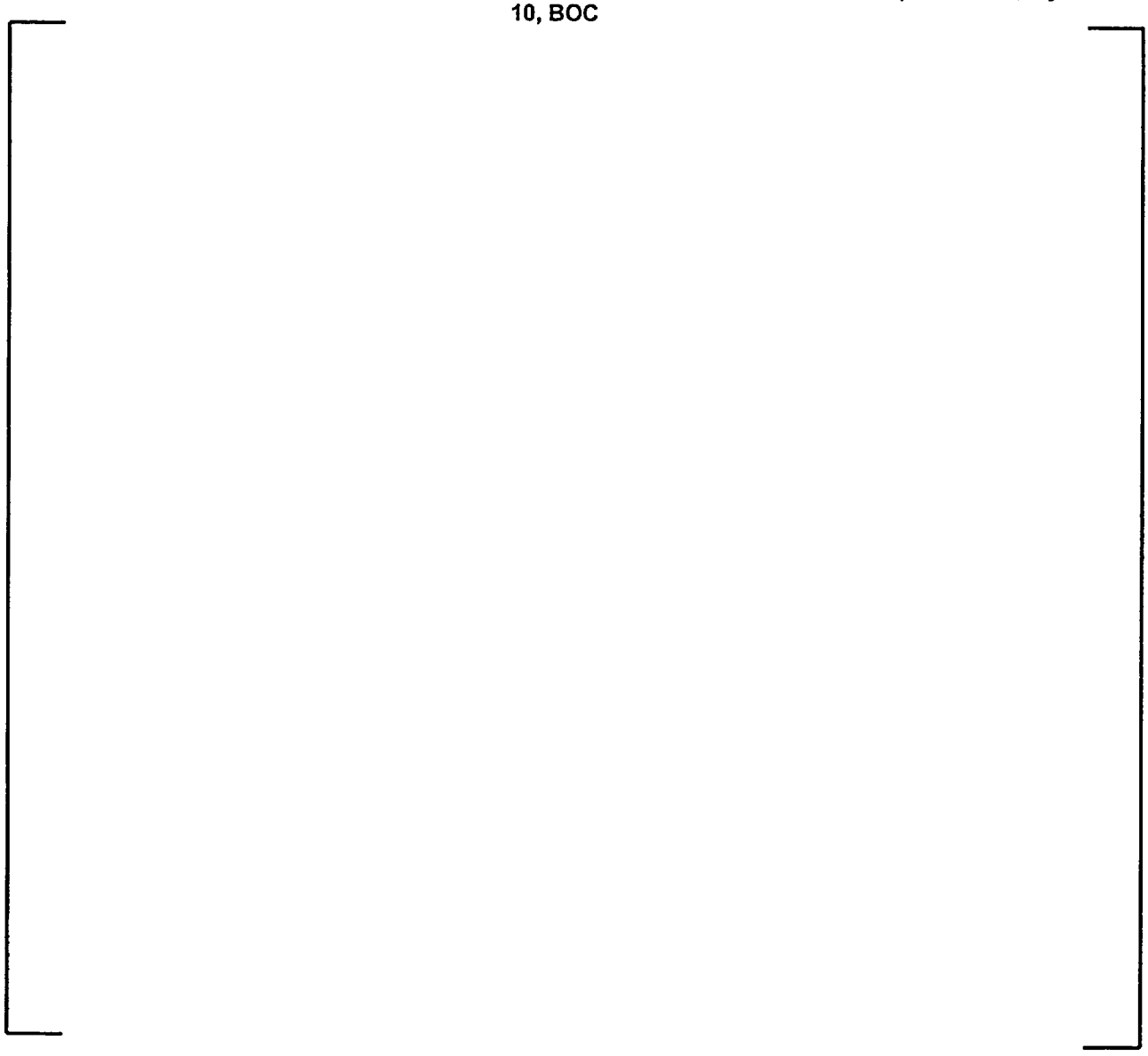

a, b, c

Figure 4-80: Core Average Axial Power Distribution (PARAGON versus PHOENIX-P) : Plant A, Cycle 10, MOC

a, b, c

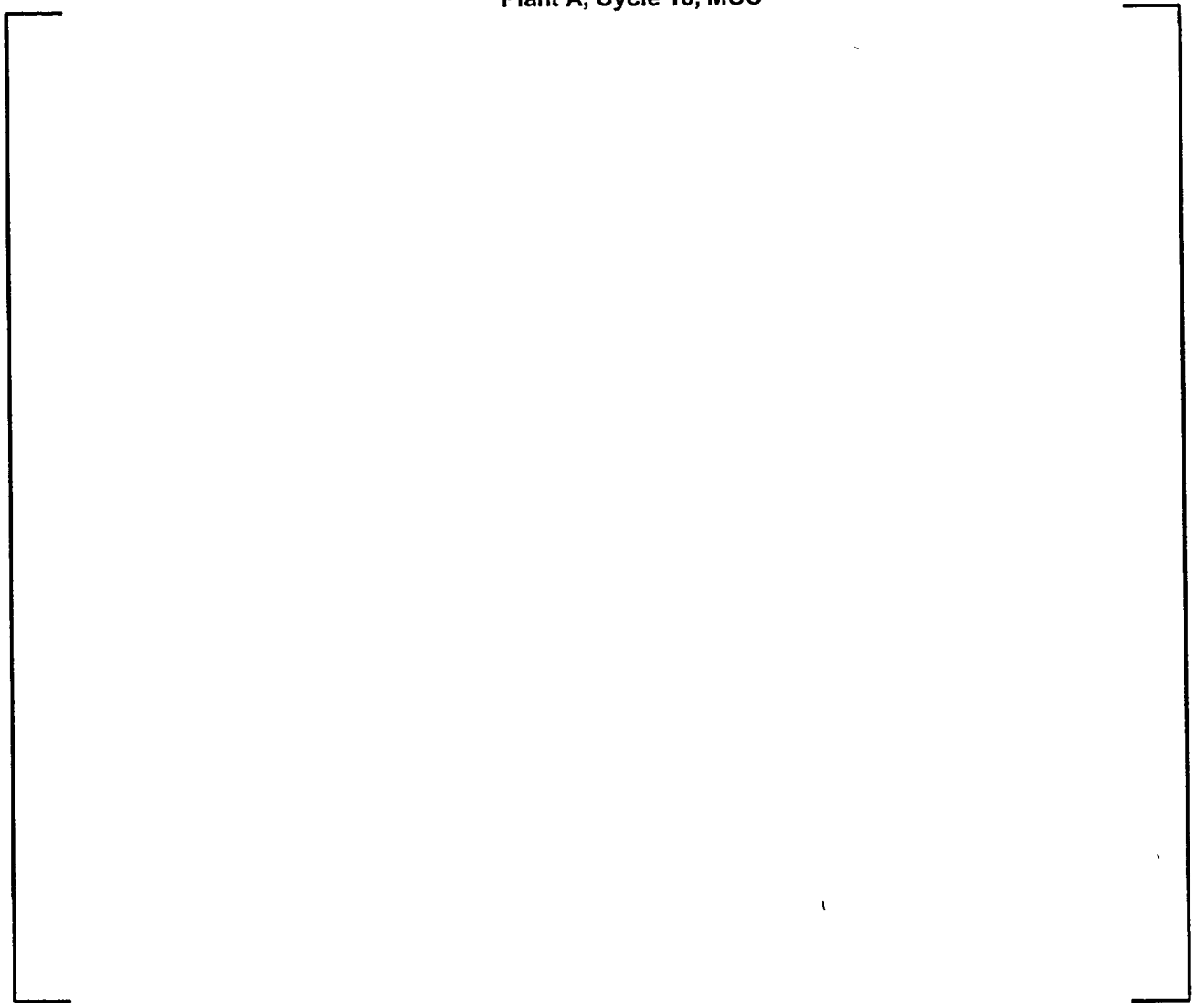

Figure 4-81: Core Average Axial Power Distribution (PARAGON versus PHOENIX-P) : Plant A, Cycle 10, EOC

a, b, c

Figure 4-82: Core Average Axial Power Distribution (PARAGON versus PHOENIX-P) : Plant A, Cycle 11, BOC

a, b, c

Figure 4-83: Core Average Axial Power Distribution (PARAGON versus PHOENIX-P) : Plant A, Cycle 11, MOC

a, b, c

Figure 4-84: Core Average Axial Power Distribution (PARAGON versus PHOENIX-P) : Plant A, Cycle 11, EOC

[a, b, c

]

Figure 4-85: Core Average Axial Power Distribution (PARAGON versus PHOENIX-P) : Plant C, Cycle 25, BOC

[a, b, c]

Figure 4-86: Core Average Axial Power Distribution (PARAGON versus PHOENIX-P) : Plant C, Cycle 25, MOC

a, b, c

Figure 4-87: Core Average Axial Power Distribution (PARAGON versus PHOENIX-P) : Plant C, Cycle 25, EOC

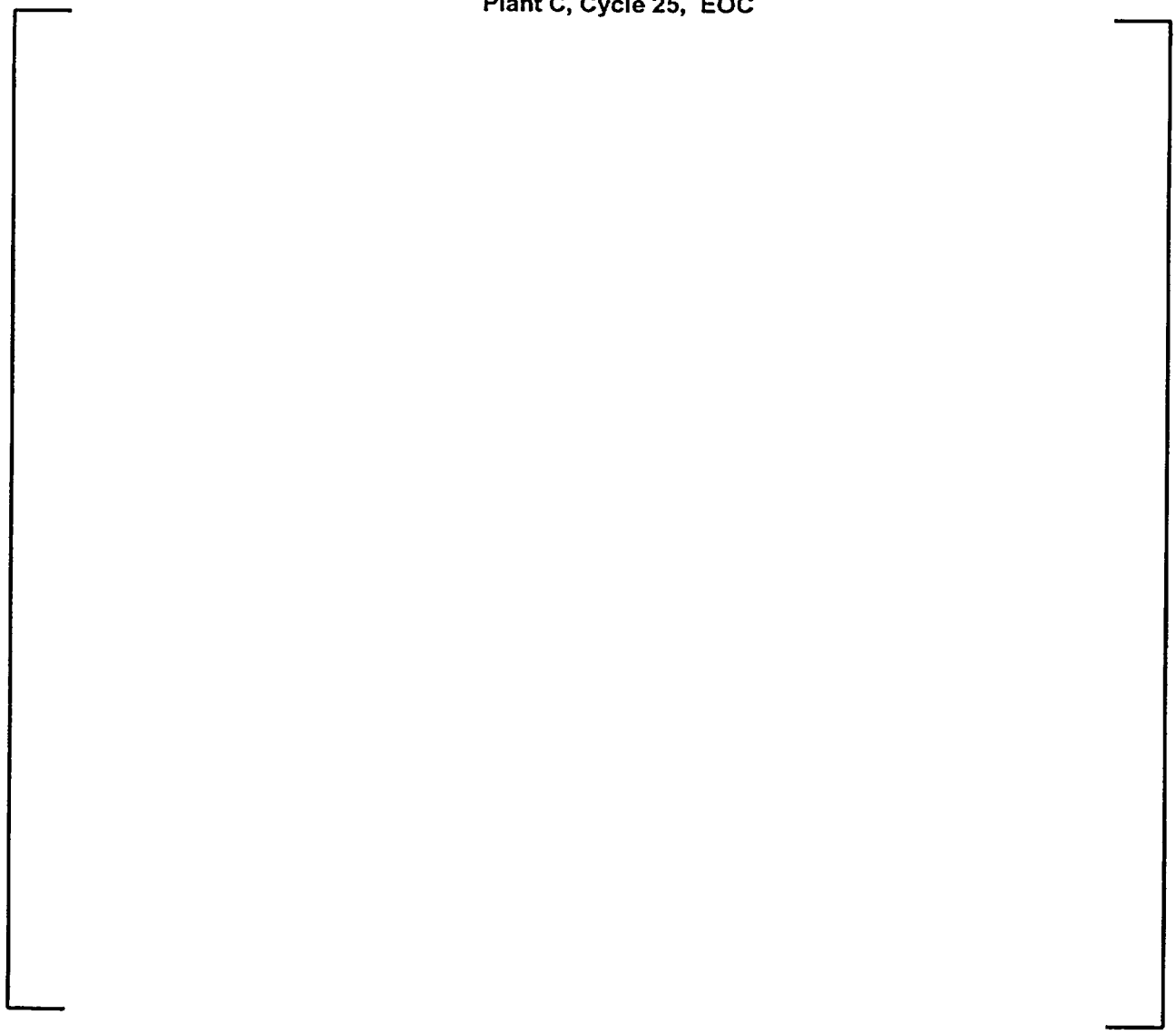

a, b, c

Figure 4-88: Core Average Axial Power Distribution (PARAGON versus PHOENIX-P) : Plant C, Cycle 26, BOC

a, b, c

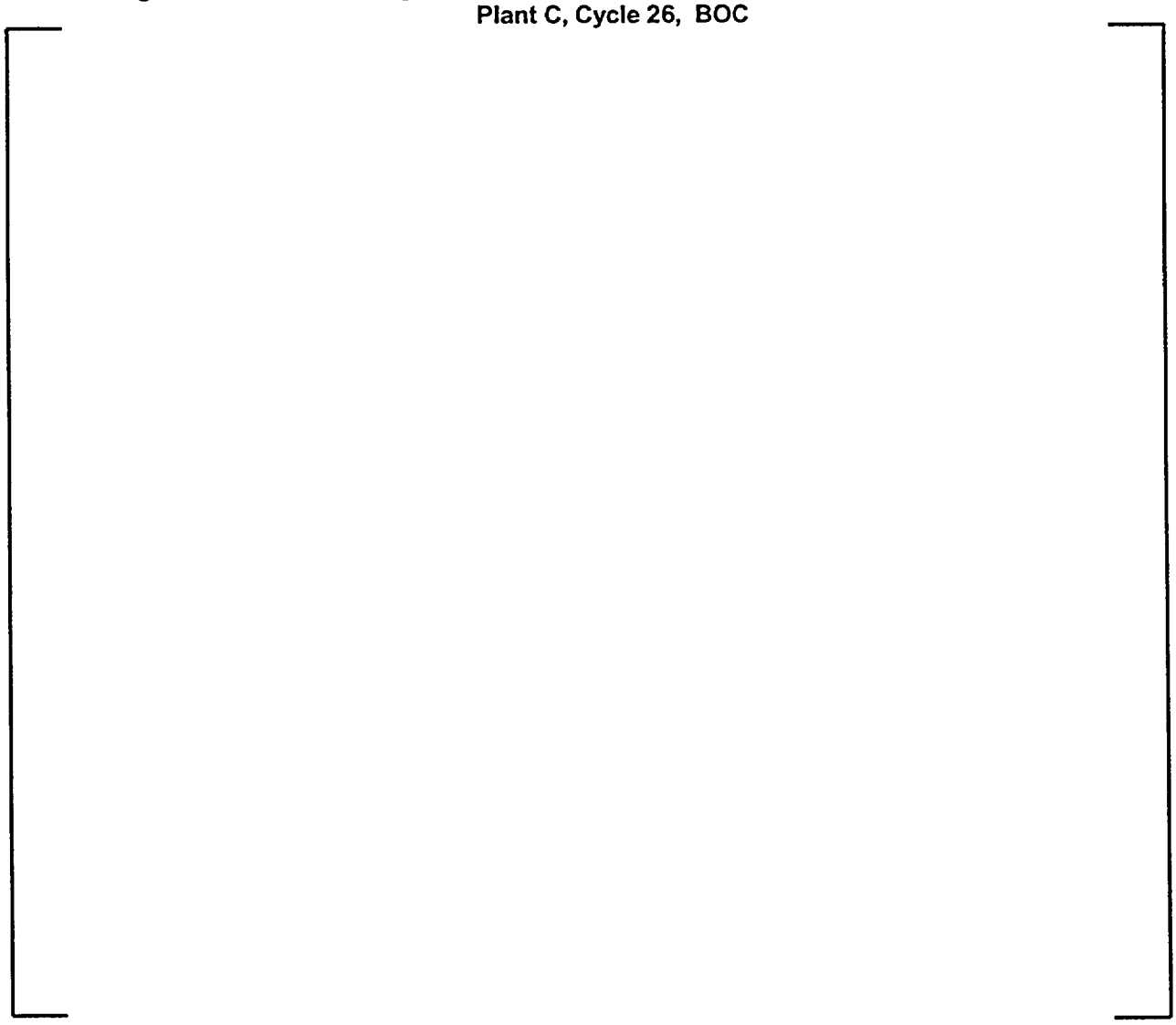

Figure 4-89: Core Average Axial Power Distribution (PARAGON versus PHOENIX-P) : Plant C, Cycle 26, MOC

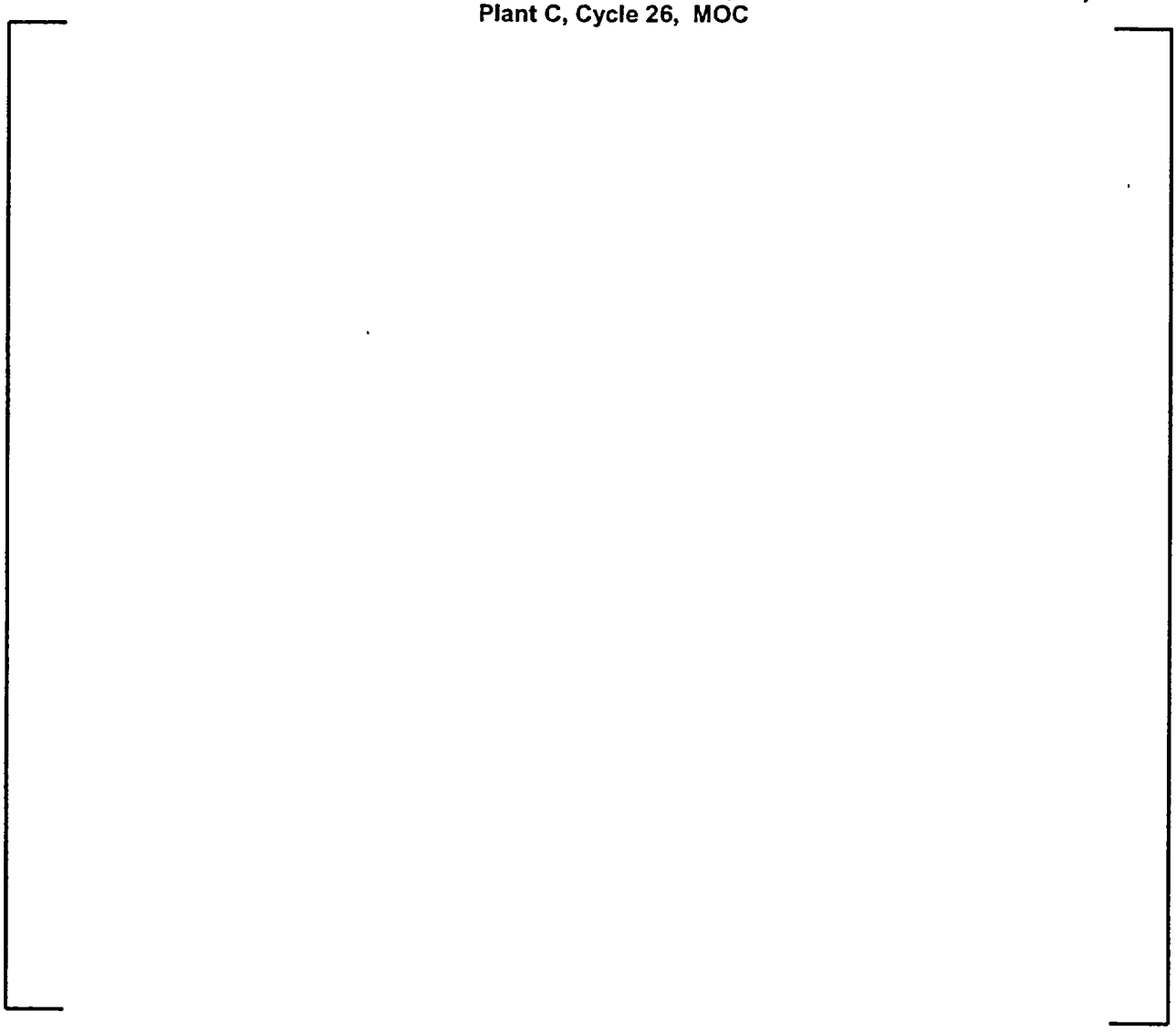

a, b, c

Figure 4-90: Core Average Axial Power Distribution (PARAGON versus PHOENIX-P) : Plant C, Cycle 26, EOC

[a, b, c

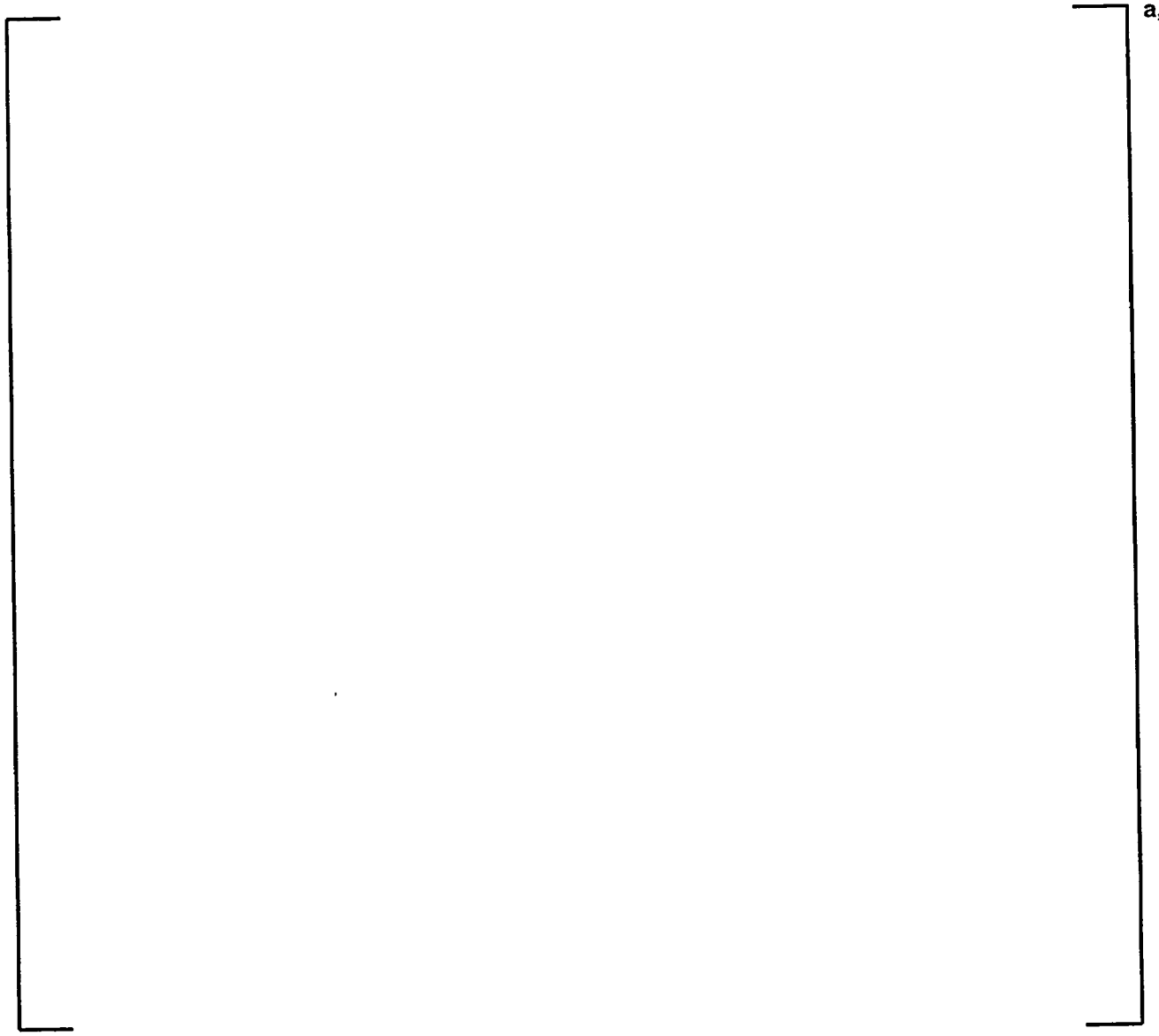

]

Figure 4-91: Core Average Axial Power Distribution (PARAGON versus PHOENIX-P) : Plant F, Cycle 11, BOC

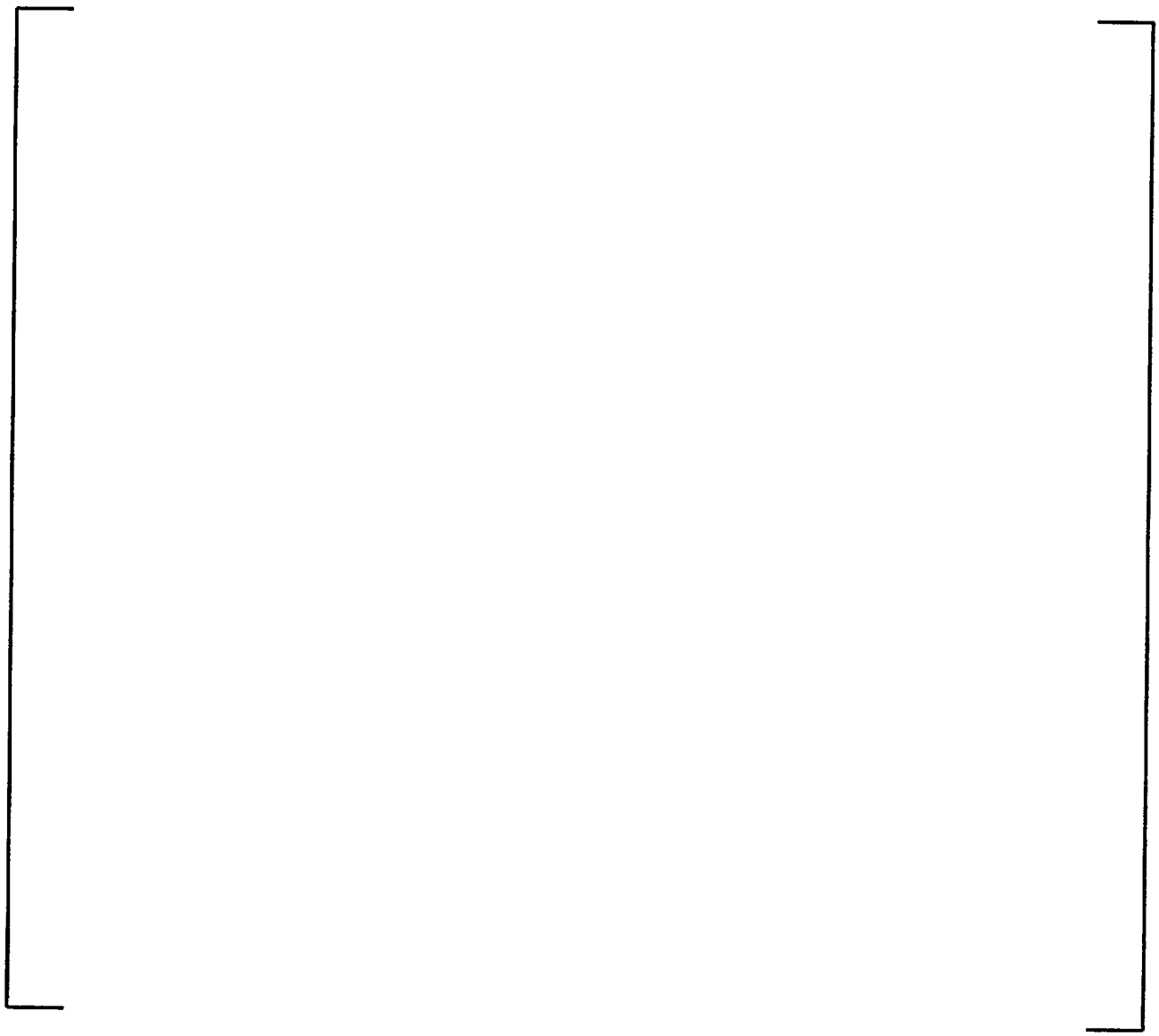

a, b, c

Figure 4-92: Core Average Axial Power Distribution (PARAGON versus PHOENIX-P) : Plant F, Cycle 11, MOC

a, b, c

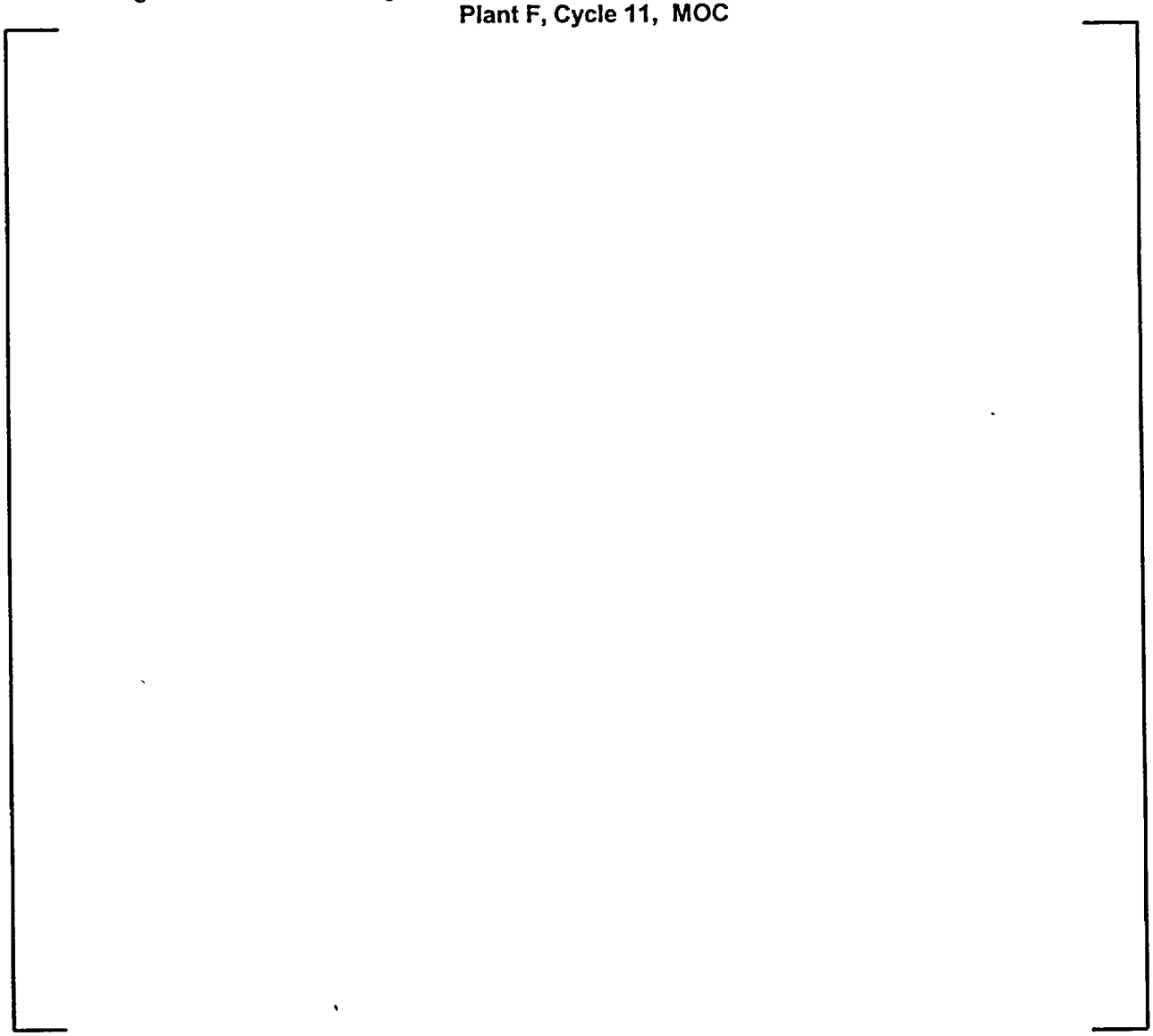

Figure 4-93: Core Average Axial Power Distribution (PARAGON versus PHOENIX-P) : Plant F, Cycle 11, EOC

a, b, c

Figure 4-94: Core Average Axial Power Distribution (PARAGON versus PHOENIX-P) : Plant F, Cycle 12, BOC

a, b, c

Figure 4-95: Core Average Axial Power Distribution (PARAGON versus PHOENIX-P) : Plant F, Cycle 12, MOC

[a, b, c

]

Figure 4-96: Core Average Axial Power Distribution (PARAGON versus PHOENIX-P) : Plant F, Cycle 12, EOC

a, b, c

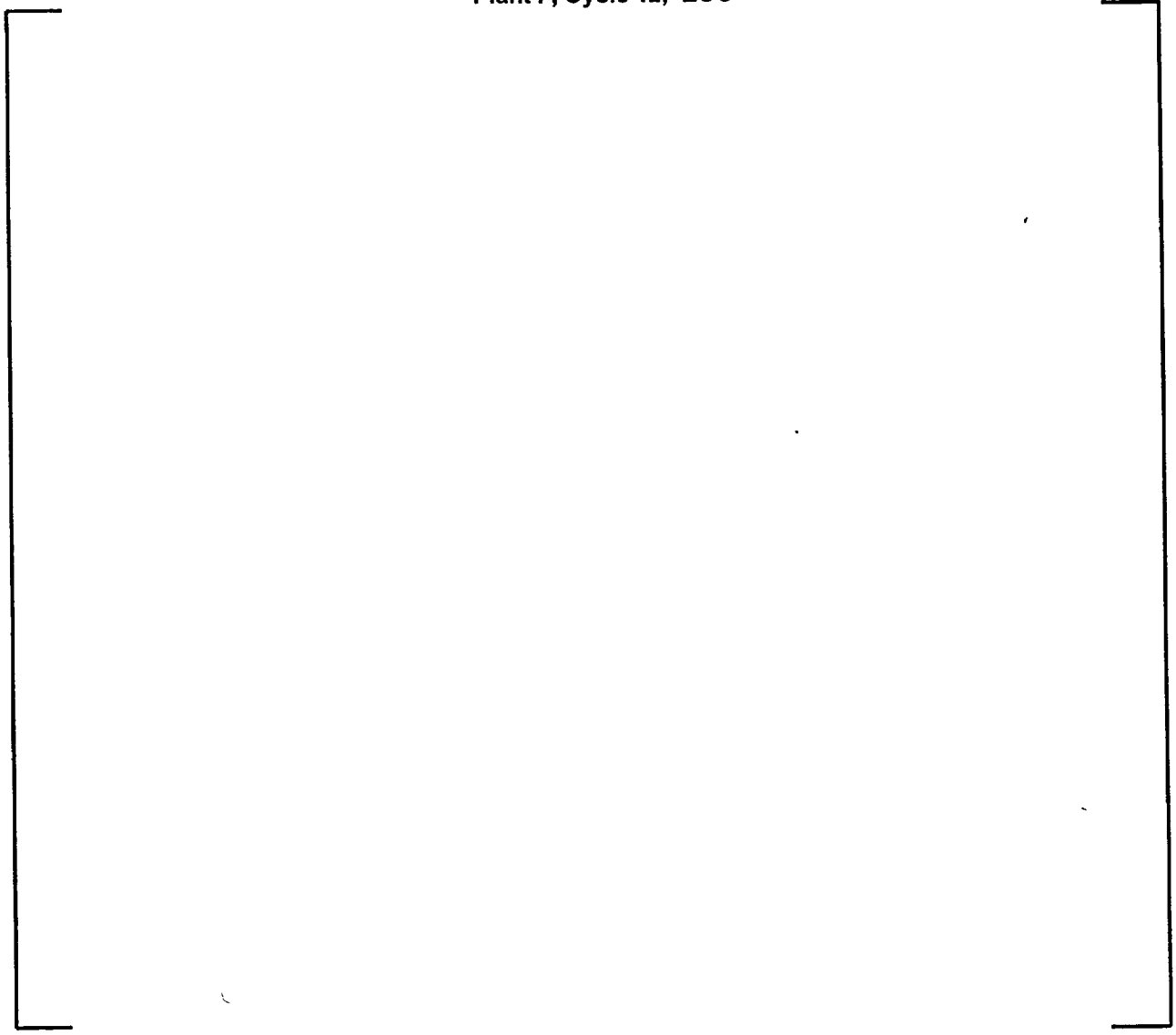

Figure 4-97: Core Average Axial Power Distribution (PARAGON versus PHOENIX-P) : Plant G, Cycle 13, BOC

a, b, c

Figure 4-98: Core Average Axial Power Distribution (PARAGON versus PHOENIX-P) : Plant G, Cycle 13, MOC

a, b, c

Figure 4-99: Core Average Axial Power Distribution (PARAGON versus PHOENIX-P) : Plant G, Cycle 13, EOC

a, b, c

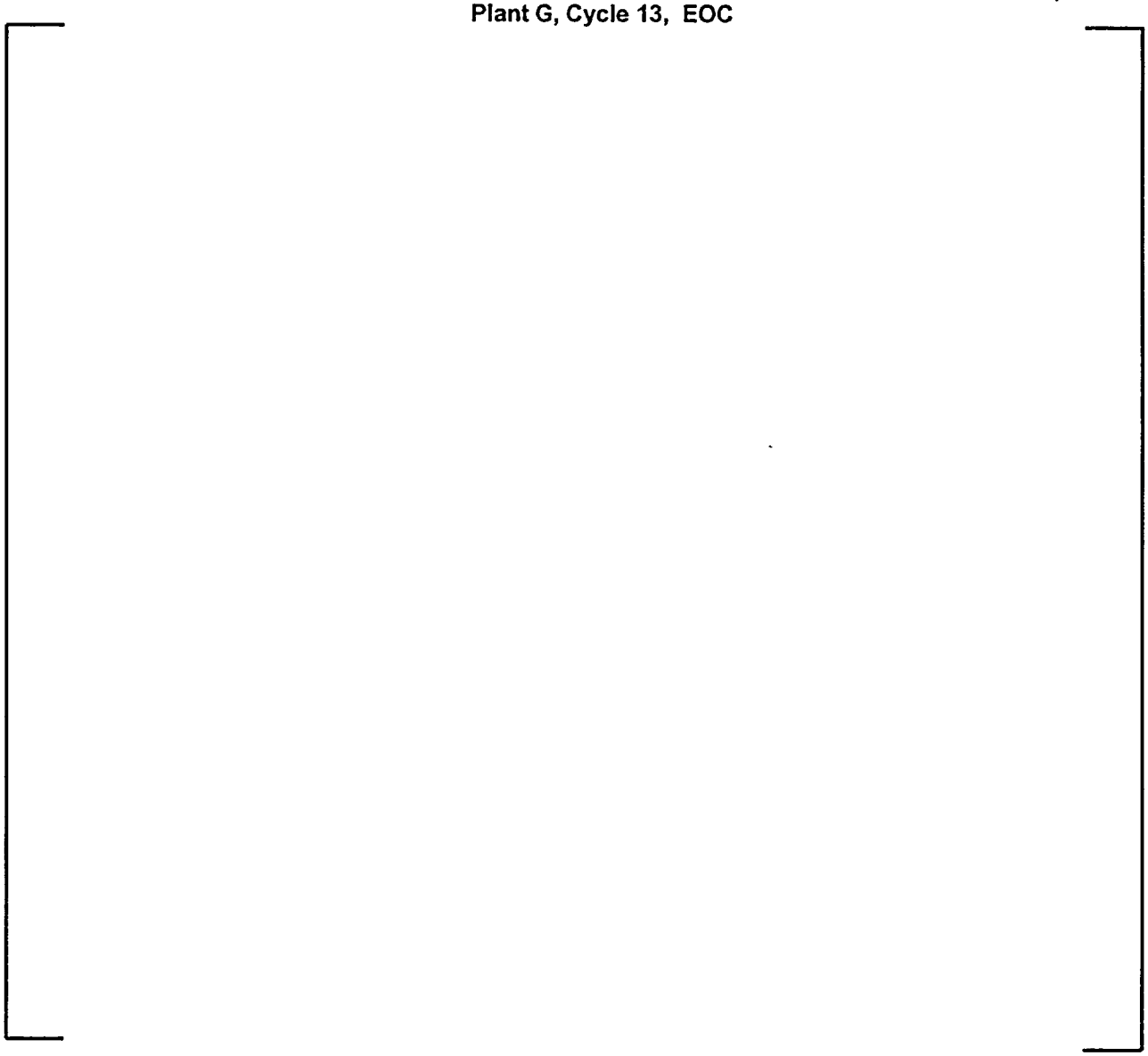

Figure 4-100: Core Average Axial Power Distribution (PARAGON versus PHOENIX-P) : Plant G, Cycle 14, BOC

a, b, c

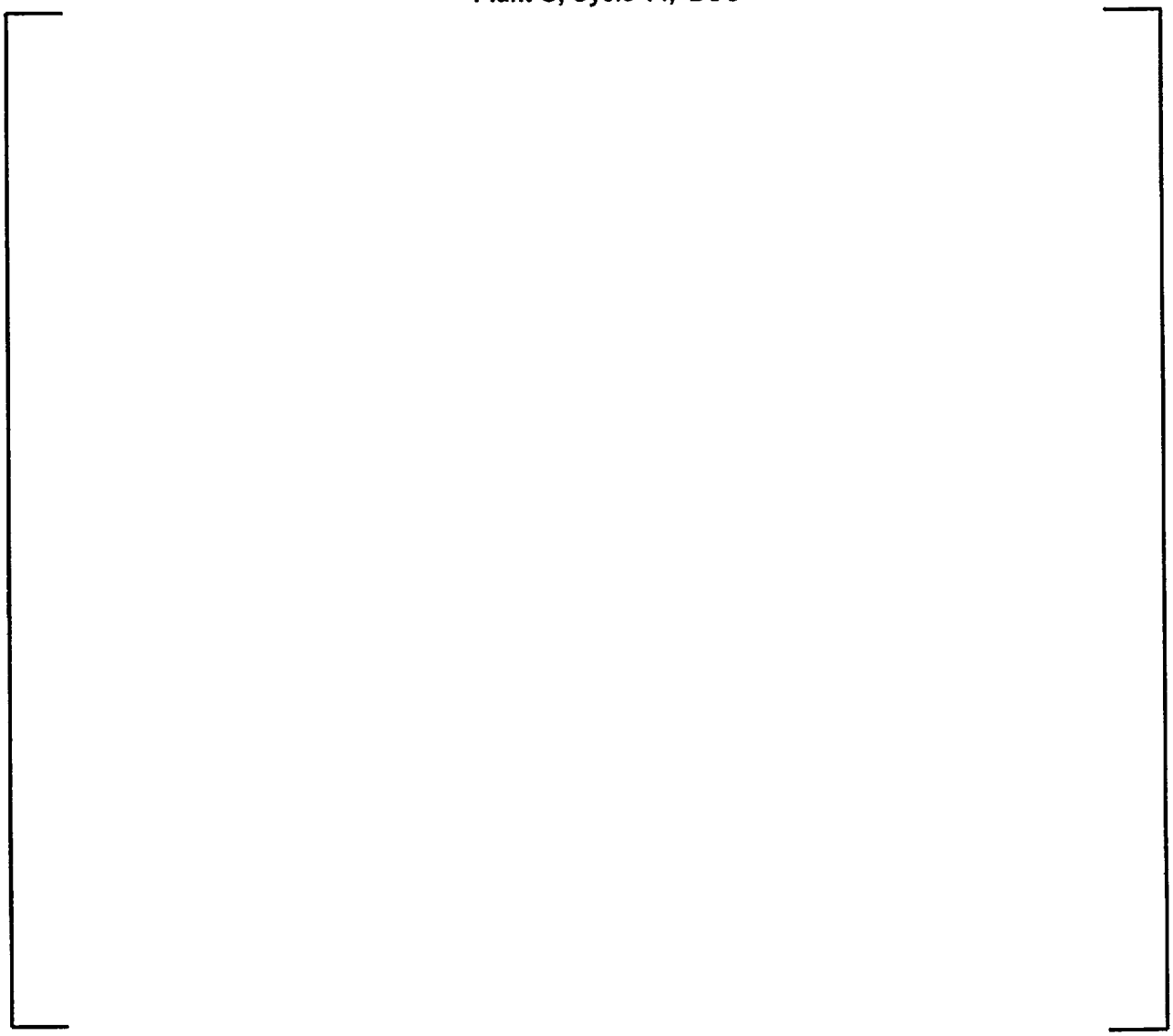

Figure 4-101: Core Average Axial Power Distribution (PARAGON versus PHOENIX-P) : Plant G, Cycle 14, MOC

a, b, c

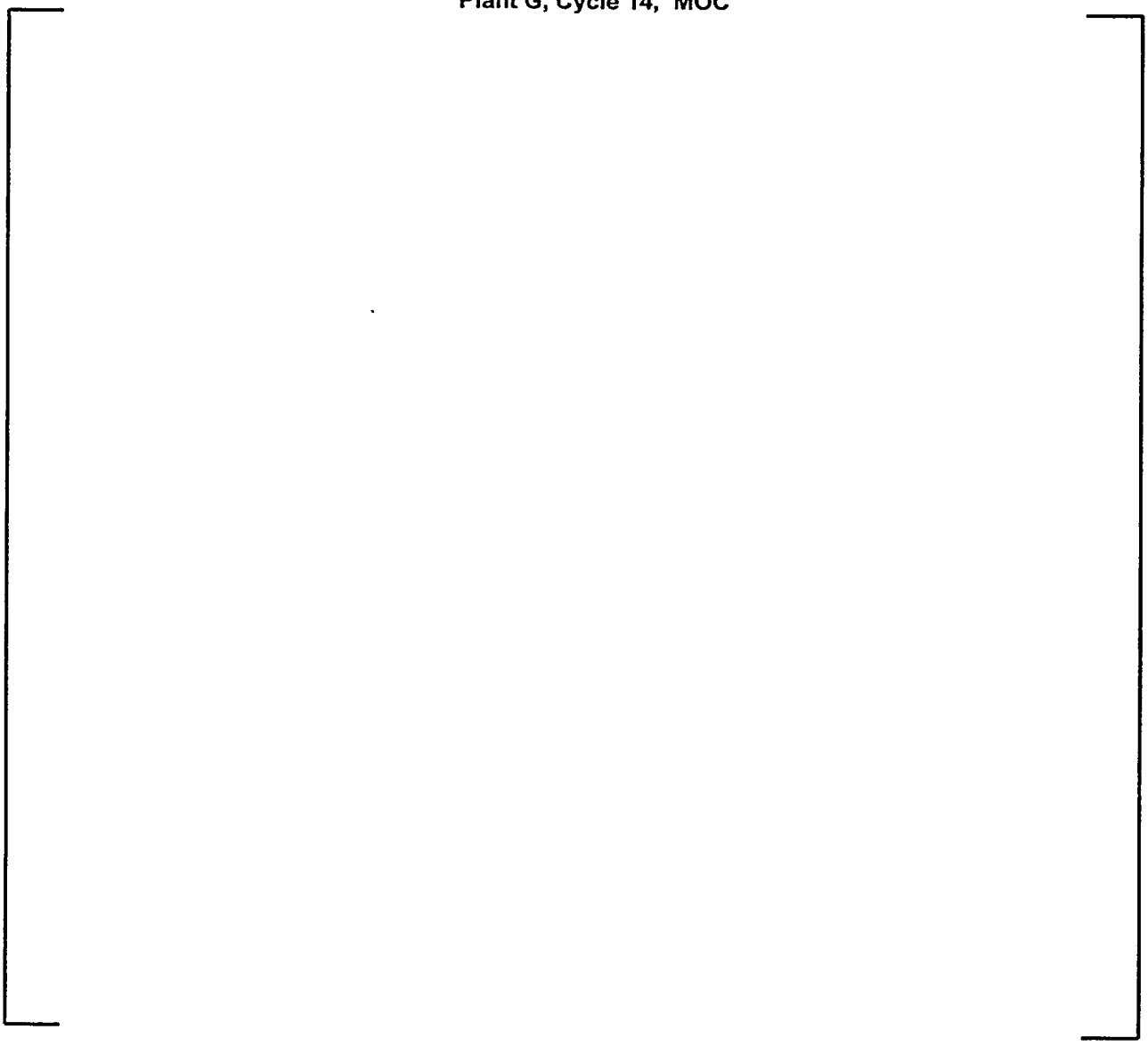

Figure 4-102: Core Average Axial Power Distribution (PARAGON versus PHOENIX-P) : Plant G, Cycle 14, EOC

a, b, c

Page Intentionally Left Blank

Section 5.0: Conclusion

The objective of this report was to provide the information and data necessary to license PARAGON both as a standalone transport code and as a nuclear data source for a core simulator in a complete nuclear design code system for core design, safety and operational calculations. PARAGON is a new transport code developed by Westinghouse. PARAGON is based on collision probability methods and is written entirely in FORTRAN 90/95. PARAGON can provide nuclear data, both cross sections and pin power information, to a core simulator code such as ANC.

Section 2 presented an overview of the PARAGON code and theory.

The qualification presented in this report followed a systematic qualification process which has been used previously by Westinghouse to qualify nuclear design codes. This process starts with the qualification of the basic methodology used in the code and proceeds in logical steps to qualification of the code as applied to a complete nuclear design code system.

5.1 PARAGON Benchmarking

Consistent with the qualification process described above, Section 3 presented the results of PARAGON run as a standalone code for a series of critical experiments, These experiments included the Strawbridge-Barry 101 criticals, the KRITZ high temperature criticals, and a large number of spatial criticals from the B&W physics verification program. The B&W criticals provided both reactivity and power distribution measurements.

5.1.1 Strawbridge-Barry Critical Experiments

The Strawbridge-Barry 101 criticals cover a wide range of lattice parameters and therefore provide a severe test for the lattice code. Since these experiments are uniform lattices, the criticals were run as single pin cells in PARAGON. There are 40 UO_2 experiments among the 101 criticals. The mean K_{eff} for these experiments calculated by PARAGON is [ ]^{a,c} with a standard deviation of [ ]^{a,c} The mean K_{eff} for all experiments was [ ]^{a,c} with a standard deviation of [ ]^{a,c} The results of these criticals were graphed as a function of water to uranium ratio, enrichment, experimental buckling, pellet diameter, and soluble boron. No biases or trends were seen as a function of any of these parameters.

5.1.2 KRITZ high temperature critical experiments

The KRITZ high-temperature criticals provide critical benchmark data for uranium-fueled, water-moderated lattices at high temperatures. The criticals were run at temperatures as high as 245 °C. Twelve KRITZ experiments were modeled in PARAGON. The mean K_{eff} for the twelve experiments was [ ]^{a,c} with a standard deviation of [ ]^{a,c} No significant trends across the large temperature range of these criticals were observed. The small standard deviation shows that PARAGON predicts very consistently across the large temperature range.

5.1.3 B&W spatial critical experiments

The B&W spatial criticals provided data on both reactivity and power distribution for a variety of uranium-oxide fueled lattices. A total of twenty nine configurations were analyzed: [

]^{a,c} K-infinity comparisons were made between PARAGON and the Monte Carlo code MCNP for all twenty-nine experiments. In addition, the measured axial bucklings were used with the PARAGON results to calculate K_{eff}.

The reactivity results for all configurations were very good with the overall K_{eff} for the twenty-nine experiments being [ ]^{a,c} with a standard deviation of [ ]^{a,c}

Rod power distribution comparisons of PARAGON results against measurements were provided for six of the experiments – two with no burnable absorbers, two with gadolinia burnable absorbers, and two with Pyrex burnable absorbers. The average difference between the measured and PARAGON power distribution for the six experiments was [ ]^{a,c} per cent with an average standard deviation of [ ]^{a,c} per cent.

5.1.4 Monte Carlo Assembly Benchmarks

Thirteen different assembly configurations were calculated in both PARAGON and the Monte Carlo code MCNP. These assembly configurations were chosen to cover a variety of lattice types and burnable absorbers over a large enrichment range. Eleven Westinghouse and two CE assemblies were included in these calculations. The PARAGON and MCNP calculations were compared for both reactivity and power distribution. The mean difference in reactivity between the MCNP and PARAGON calculations over the thirteen assemblies was [ ]^{a,c} with a standard deviation of [ ]^{a,c} The comparison between the MCNP and PARAGON power distributions showed very good agreement. The average difference in rod powers for each assembly ranged from [ ]^{a,c} Standard deviations of the rod power differences for each assembly range from [ ]^{a,c}

5.1.5 Saxton and Yankee Isotopics Data

The spectrograph-measured isotopics data for Saxton Cores 2 and 3 with mixed oxide fuel, Yankee cores 1, 2, and 4 with stainless steel clad fuel, and Yankee Core 5 with zircaloy clad fuel have been compared to isotopic concentrations from PARAGON calculations simulating the power history corresponding to these cores. These isotopic comparisons show no significant trend for any isotope with burnup. These excellent results demonstrate the capability of PARAGON for predicting the depletion characteristics of both UO_2 and PuO_2 LWR fuel over a wide range of burnup conditions.

5.2 Plant comparisons

The primary use of PARAGON will be to generate nuclear data for use in Westinghouse core simulator codes. Thus the most important qualification for PARAGON is comparisons of results of core calculations using PARAGON supplied nuclear data against plant measured data. This report presented ANC results for PWR core calculations with nuclear data supplied by PARAGON which were compared to corresponding plant measurements where available and to PHOENIX-P/ANC results for the same calculations. These calculations demonstrated the accuracy of the PARAGON nuclear data when applied to a complete nuclear design system. The calculations also demonstrated that PARAGON can replace all the previously licensed Westinghouse PWR lattice codes, such as PHOENIX-P, for use in all the previously licensed Westinghouse methodologies for PWR applications.

Cycles from eleven plants including both Westinghouse and Combustion Engineering type plants were used for measured to PARAGON/ANC predicted comparisons of startup data and at-power critical boron versus cycle burnup data. Measured radial power information was compared to PARAGON/ANC predicted values from 28 radial power maps from five different plants. BOC and EOC radial power and EOC burnup predictions from PHOENIX-P/ANC were compared to those calculated by PARAGON/ANC for nine cycles in five plants. PARAGON/ANC axial power predictions were compared to PHOENIX-P/ANC at BOC, MOC, and EOC for four plants. Finally, PARAGON/ANC results are compared to PHOENIX-P/ANC results for events for which measurements are generally not made or cannot be made. These are ARI-WSR (worst stuck rod)

rodworth (four plants), dropped rod events (four plants) and rod ejection events (BOC and EOC for four plants).

5.2.1 *Plants Cycles used for Comparison*

The PARAGON qualification included 24 cycles in 11 plants. These plants included both Westinghouse (15 cycles) and Combustion Engineering (9 cycles) type cores. The plants were chosen to cover a wide variety of lattices, burnable absorbers, blanket types, and core sizes. The availability of reliable measured data was also a consideration.

5.2.2 *Startup Test Results Comparisons*

Comparisons were made for PARAGON/ANC predictions against measurements for BOC HZP ARO critical boron, BOC HZP ARO isothermal temperature (ITC), and BOC HZP rodworths. Results from twenty-two cycles from 11 plants were compared for the BOC HZP critical boron. The mean difference between measured and predicted was [ ]^{a,c} for PARAGON/ANC and [ ]^{a,c} for PHOENIX-P/ANC. The standard deviations were excellent for both code systems: [ ]^{a,c} for PARAGON/ANC and [ ]^{a,c} for PHOENIX-P/ANC.

Results from the BOC HZP ARO ITC were compared for the same twenty-two cycles. The statistics from the ITC comparison were quite similar between the two code systems. The mean predicted to measured difference in ITC was [ ]^{a,c} pcm/°F for PARAGON/ANC and [ ]^{a,c} for PHOENIX-P/ANC. The standard deviations were the same for both code systems at 0.8 pcm/°F.

Predicted versus measured rodworths were compared for nine cycles in seven plants. The cycles used three different methods for rodworth measurement: DRWM, rod swap, and boron dilution. All rodworth predictions met the measurement review criteria. The average measured to predicted difference for all the rods over all nine cycles was [ ]^{a,c} for PARAGON/ANC with a standard deviation of [ ]^{a,c} The corresponding values for the PHOENIX-P/ANC code system were [ ]^{a,c}

5.2.3 *Critical boron comparisons*

At-power critical boron measurements were compared to results from PARAGON/ANC and PHOENIX-P/ANC core depletion calculations for twenty-two plant cycles. The results showed very good performance by PARAGON/ANC for EOC predictions. All plant cycles showed the effects of B^{10} depletion since the uncorrected measured and predicted critical boron values difference grew through the middle of the cycle. Accounting for B^{10} depletion reduces the difference between measured and predicted values through the middle of the cycle as was demonstrated in the report for one of the cycles.

5.2.4 *Radial Power Distributions*

Measured to PARAGON-predicted radial assembly power comparisons were made for five plants (28 total flux maps). These plants included both even (16x16 and 14x14) and odd (15x15 and 17x17) lattices. The range of cycle burnups for these maps was [ ]^{a,c} MWD/MTU. When processing the flux maps, the measured values were folded into the lower right quadrant to remove any core tilts. The average value of the measured to predicted differences over the twenty-eight maps was [ ]^{a,c} with an average standard deviation of [ ]^{a,c} These results show that the radial assembly powers are well predicted by PARAGON/ANC.

5.2.5 PARAGON/ANC to PHOENIX-P/ANC results

PARAGON/ANC and PHOENIX-P/ANC results were compared for radial assembly power distribution, axial power distribution, ARI-WSR rodworth, dropped rod, and rod ejection calculations. Radial assembly power (BOC and EOC) distributions were compared for nine cycles in five plants. EOC assembly burnup distributions were compared for the same cycles. Axial power distributions are shown at BOC, MOC, and EOC for eight cycles in four plants. The plant cycles for both radial and axial comparisons include Westinghouse and Combustion Engineering type cores. The results of both radial and axial power comparisons show very little difference between PARAGON/ANC and PHOENIX-P/ANC. Experience has shown that PHOENIX-P/ANC predicts radial and axial powers very well. The small difference between the PARAGON/ANC results and those from PHOENIX-P/ANC confirms that PARAGON/ANC also predicts these power distributions well.

ARI-WSR shutdown rodworths were calculated in PARAGON/ANC at BOC for four plants. The results were compared to PHOENIX-P/ANC for the same calculations. The largest difference for the worst stuck rodworth was [ ]^{a,c} The largest peaking factor difference was about [ ]^{a,c} Both differences are well within the uncertainties used with the ARI-WSR calculations.

Dropped rod calculations were also performed with PARAGON/ANC at BOC for four plants and the results were compared to corresponding PHOENIX-P/ANC results. The largest difference in the dropped rod worth was [ ]^{a,c} The largest difference in peaking factor was [ ]^{a,c} in Fq.

The last set of comparisons between PARAGON/ANC and PHOENIX-P/ANC were for BOC and EOC rod ejection calculations for four plants. The rod ejection calculations were performed for both HZP and HFP conditions. Rod ejection calculations are similar to stuck rod calculations except the feedback is frozen from pre-ejection conditions leading to much larger peaking factors and rodworths. The largest difference in rodworth was [ ]^{a,c} rod. The peaking factor differences were very small and well within the uncertainties used with this event.

5.3 Conclusion

The data presented in this report provide the basis for the qualification of PARAGON both as a standalone transport code and as the nuclear data source for core simulator codes. In chapter 3, standalone PARAGON was qualified against a wide variety of criticals and Monte Carlo calculations. In chapter 4, PARAGON was qualified as a supplier of core simulator code nuclear data through comparisons of the PARAGON results with ANC as the core simulator against measured data and against PHOENIX-P/ANC for a wide variety of plant designs and problems. The report demonstrates that PARAGON can replace all the previously licensed Westinghouse PWR lattice codes, such as PHOENIX-P, for use in all the previously licensed Westinghouse methodologies for PWR applications.

Section 6.0: References

Section 1.0

1-1 Liu, Y. S., et. al., "ANC: A Westinghouse Advanced Nodal Computer Code", WCAP-10965-P-A (Proprietary), and WCAP-10966-A (Nonproprietary), September, 1986

1-2 Nguyen, T. Q., et. al., "Qualification of the PHOENIX-P/ANC Nuclear Design System for Pressurized Water Reactor Cores", WCAP-11596-P-A (Proprietary), and WCAP-11597-A (Nonproprietary), June, 1988

Section 2.0

2-1 Nguyen, T. Q. et al., " Qualification of the PHOENIX-P/ANC Nuclear Design System for Pressurized Water Reactor Cores", WCAP-11596-P-A (Proprietary), and WCAP-11597-A (Nonproprietary), June, 1988.

2-2 Ouisloumen, M. et al., "The Two-Dimensional Collision Probability Calculation in Westinghouse Lattice Code: Methodology and Benchmarking", Proc. Int. Conf. On The Physics Of Reactors PHYSOR96, Vol. 1, A366, Mito, Japan, 1996.

2-3 MacFarlane R.E., "NJOY91.118: A code System For Producing Pointwise And Multigroup Neutron and Photon Cross Sections From ENDF/B Evaluated Nuclear Data", ORNL, RSIC, PSR-171(1994)

2-4 Stamm'ler R.J.J, Abbate M.J., "Methods Of Steady-State Reactor Physics in Nuclear Design", Academic Press, London (1983)

2-5 Villarino E.A., Nucl. Sci. Eng., 112, 16 (1992)

2-6 Thomsen K.L, Nucl. Sci. Eng., 119, 167 (1995)

2-7 Ouisloumen M. and Tahara Y., "PARAGON: The New Westinghouse Transport Code", Proc. Int. Conf. On The Physics of Nuclear Science and Technology, Vol. 1, 118, Long Island, New York, 1998.

2-8 Ouisloumen et al., "PARAGON: The New Westinghouse Lattice Code", Proc. ANS Int. Meeting on Mathematical Methods for Nuclear Applications, September 2001, Salt Lake City, Utah, USA

2-9 Hebert A, "Isotropic Streaming Effects in Thermal Lattices", Proc. ANS Int. Meeting on Mathematical Methods for Nuclear Applications, September 2001, Salt Lake City, Utah, USA

Section 3.0

3-1 Nguyen, T. Q., et. al., "Qualification of the PHOENIX-P/ANC Nuclear Design System for Pressurized Water Reactor Cores", WCAP-11596-P-A (Proprietary), and WCAP-11597-A (Nonproprietary), June, 1988.

3-2 Strawbridge, L. E., and Barry, R. F., "Criticality Calculations for Uniform Water-Moderated Lattices", Nucl. Sci. Eng. 23, pp 58-73 (1965).

3-3 Persson, R., Blomsjo, E., and Edenius, M., "High Temperature Critical Experiments with H2O Moderated Fuel Assemblies in KRITZ", Techical Meeting No. 2/11, NUCLEX 72, (1972).

3-4 Mosteller, R. D., "Critical Lattices of UO2 Fuel Rods and Perturbing Rods in Borated Water, LA-UR 95-1434, (1995)

3-5 Newman, L.W., "Urania-Gadolinia: Nuclear Model Development and Critical Experiment Benchmark, DOE/ET/34212-41 (April, 1984)

3-6 Nodvik, R. J., "Saxton Core II Fuel Performance Evaluation Part II: Evaluation of Mass Spectrometric and Radiochemical Analyses of Irradiated Saxton Plutonium Fuel," WCAP-3385-56 Part II (July, 1970).

3-7 Smalley, W. R., Saxton II – Fuel Performance Evaluation Part I: Materials", WCAP-3385-56 Part I (September, 1971).

3-8 Goodspeed, R. C., "Saxton Plutonium Project – Quarterly Progress Report for the Period Ending June 20, 1973", WCAP-3385-36 (July, 1973)
3-9 Crain, H. H., "Saxton Plutonium Project – Quarterly Progress Report for the Period Ending September 30, 1973", WCAP-3385-37 (December, 1973)
3-10 Melehan, J. B., "Yankee Core Evaluation Program Final Report", WCAP-3017-6094 (January, 1971).
3-11 Nodvik, R. J., "Supplementary Report on Evaluation of Mass Spectrometric and Radiochemical Analyses of Yankee Core I Spent Fuel, Including Isotopics of Elements Thorium through Curium", WCAP-6086 (August, 1969).
3-12 "MCNP4B - Monte Carlo N-Particle Transport Code System", CCC-660, RSICC Computer Code Collection, April, 1997.

Section 4.0

4-1 Liu, Y. S., et. al., "ANC: A Westinghouse Advanced Nodal Computer Code", WCAP-10965-P-A (Proprietary), and WCAP-10966-A (Nonproprietary), September, 1986
4-2 Nguyen, T. Q., et. al., "Qualification of the PHOENIX-P/ANC Nuclear Design System for Pressurized Water Reactor Cores", WCAP-11596-P-A (Proprietary), and WCAP-11597-A (Nonproprietary),, June, 1988.

Page Left Intentionally Blank